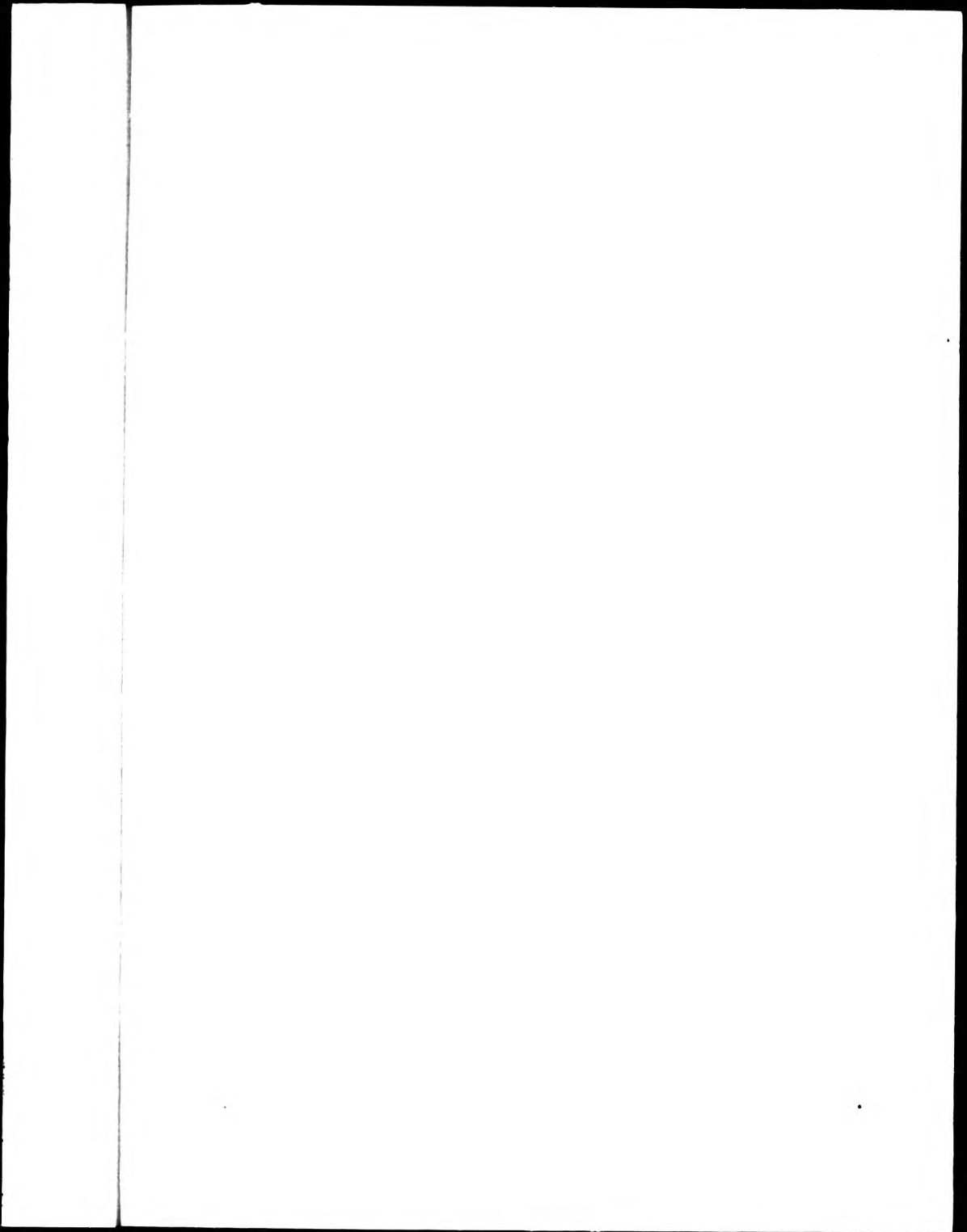
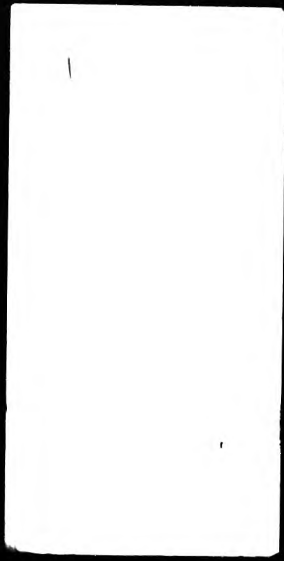


This PDF was created from the British Library's microfilm copy of the original thesis. As such the images are greyscale and no colour was captured.

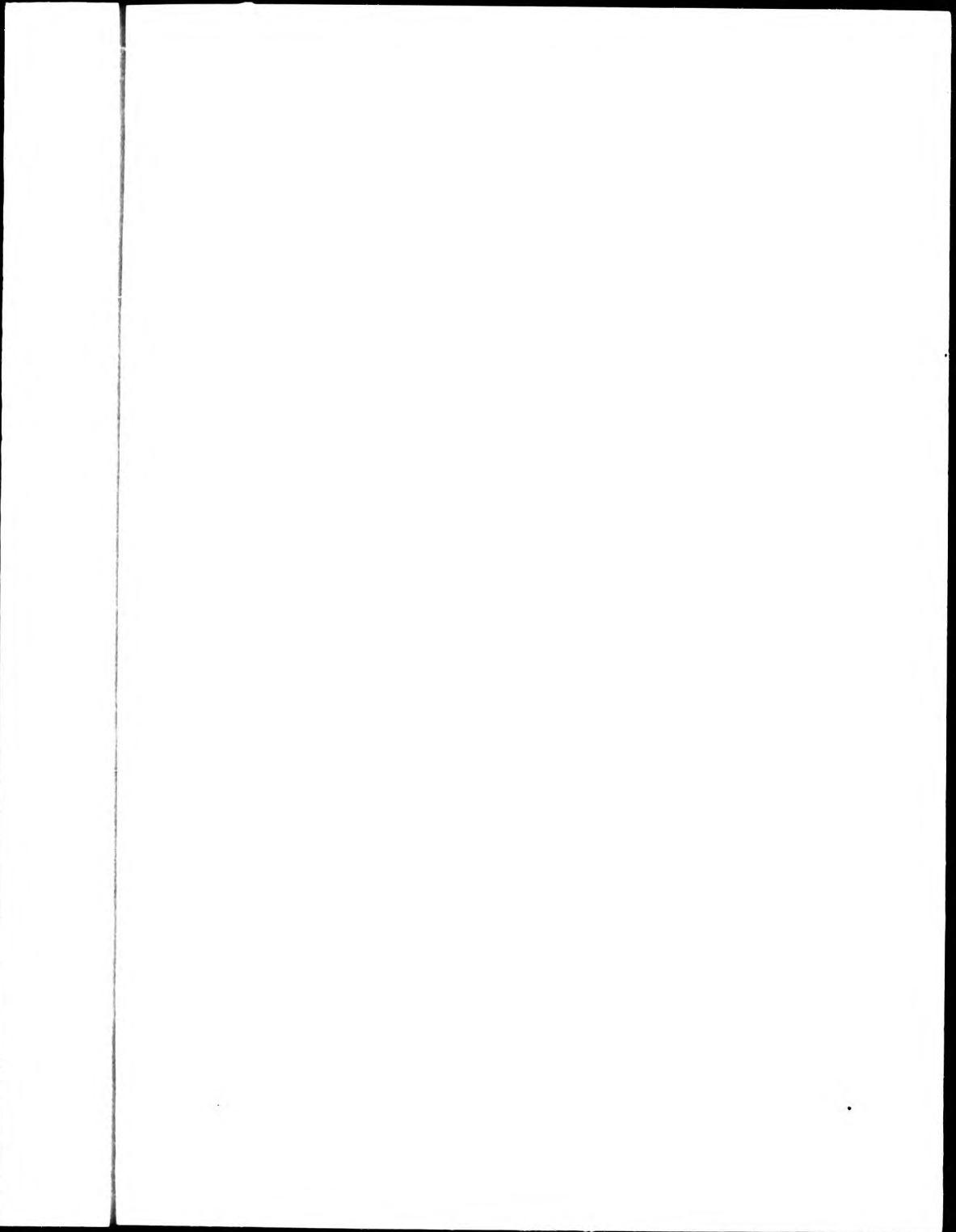
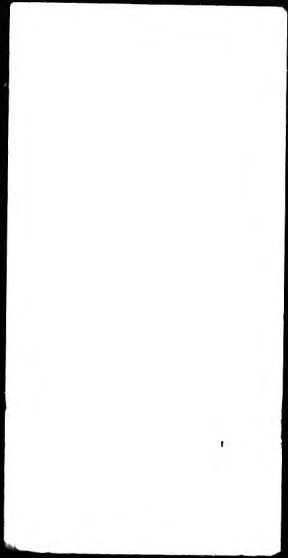
Due to the scanning process, an area greater than the page area is recorded and extraneous details can be captured.

This is the best available copy



DX

87724





THE BRITISH LIBRARY DOCUMENT SUPPLY CENTRE

TITLE AN INVESTIGATION OF DEFECT FORMATION AND GROWTH IN
EPOXY RESIN USING LIGHT SCATTERING METHODS

Elaine Ann Perkins

AUTHOR

INSTITUTION
and DATE

City of London
Polytechnic, 1989 (C.N.A.A.)

Attention is drawn to the fact that the copyright of this thesis rests with its author.

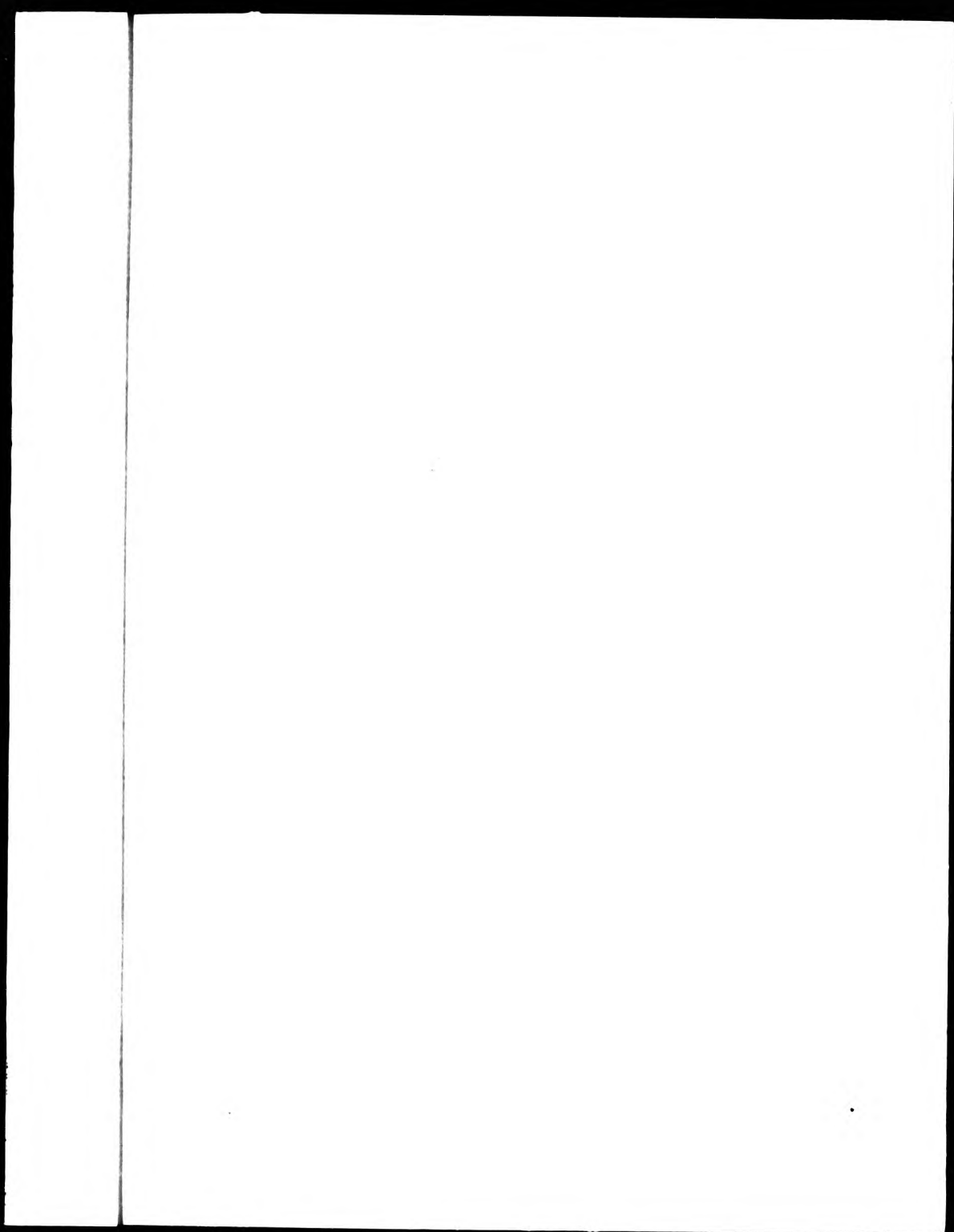
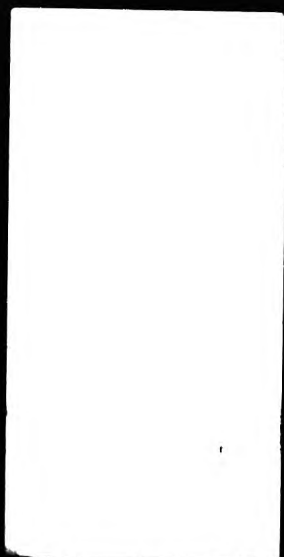
This copy of the thesis has been supplied on condition that anyone who consults it is understood to recognise that its copyright rests with its author and that no information derived from it may be published without the author's prior written consent.

THE BRITISH LIBRARY
DOCUMENT SUPPLY CENTRE
Boston Spa, Wetherby
West Yorkshire
United Kingdom

1	2	3	4	5	6	7	8
cms							

CAM. 9

REDUCTION X 21



AN INVESTIGATION OF DEFECT FORMATION AND GROWTH IN
EPOXY RESIN USING LIGHT SCATTERING METHODS

BY

Elaine Ann Perkins

A thesis submitted for the degree of Doctor of
Philosophy in partial fulfillment of the requirement of
the Council for National Academic Awards.

Physics Department,
City of London
Polytechnic,
31, Jewry Street,
London. EC3N 2EY

July 1989

CONTENTS

Acknowledgements	(iii)
Abstract	(iv)
Chapter 1. Introduction	
1.1 General Introduction	1
1.2 Chemistry of epoxies	2
1.3 Evidence of Microstructure	3
1.4 Epoxy Failure and Fracture	7
1.5 Electrical Breakdown and Treeing	13
1.6 Bulk Scattering Techniques	17
1.7 Summary	18
Chapter 2. Light Scattering Theory.	
2.1 Introduction	20
2.2 Rayleigh Scattering	24
2.3 Model Approach	26
2.3.1 R.G.D. Scattering	27
2.3.2 Mie Theory of Scattering	29
2.4 Data Fitting and Error Analysis	30
2.5 The Statistical Approach	42
2.6 Conclusions	45
Chapter 3. Experimental Apparatus and Technique	
3.1 Introduction	47
3.2 The Light Scattering System	50
3.2.1 Refractive Index Measurements	60
3.2.2 Electrical Stressing in Situ	61
3.3.1 Alignment of the System	62
3.3.2 Calibration of the System	63
3.4 Summary	71
3.5 Conclusions	72
Chapter 4. Preparation of Resin Samples for Light Scattering.	
4.1 Introduction	73
4.2 Epoxy Resin System	74
4.3 Possible Network Defects	78
4.4 Preparation of Samples	82
4.4.1 Ultra Clean Samples	82

4.4.2	Voided Samples	88
4.5	Conclusions.....	89

Chapter 5. Mechanical Stressing of Epoxy Resins.

5.1	Introduction	91
5.2	Stressing of Samples and Results	91
5.2.1	Scattering from Unstressed Samples	91
5.2.2	Stress Procedure	94
5.2.3	Results on Light Scattering of Stressed Samples	96
5.2.4	Scattering Behaviour of Inhomogeneities under Tensile Stress	96
5.2.5	Behaviour of Voids under Stress	105
5.2.6	Behaviour of Gas Filled Samples	110
5.2.7	Stress Strain Measurements	114
5.3	Discussion	118
5.3.1	Inhomogeneities	118
5.3.2	Pre-existing Voids in the Network	126
5.4	Conclusions	131

Chapter 6. Electrical Stressing of Epoxy Resins.

6.1	Introduction	133
6.2	Preparation of Pintips	133
6.3	Results of Stressing of Samples	139
6.3.1	D.C. Stressed Samples	139
6.3.2	A.C. Stressed Samples	152
6.4	Discussion	155
6.5	Conclusions	160

Chapter 7. Discussion. 162

References.....	173
-----------------	-----

ACKNOWLEDGEMENTS

I would like to thank my supervisors Dr J.V.Champion of the City of London Polytechnic, and Dr G.C. Stevens of the Central Electricity Research laboratories for all their help in guiding me through this work. I would also like to thank all the technical staff at The City of London Polytechnic with special mention for Messrs Pat Driscoll, Bill Hugglestone and Dave Wiffen and a very big thankyou for Mr Victor Manning for producing almost all the 'dogbones'. Thankyou too to Miss Dympna O'Shaughnessy for typing this work . Finally I would like to thank my parents for all their support and the City of London Polytechnic for a Research Assistantship whilst carrying out this work.

AN INVESTIGATION OF DEFECT FORMATION AND GROWTH IN EPOXY
RESINS USING LIGHT SCATTERING METHODS

by Elaine Ann Perkins

ABSTRACT

This work has used laser light scattering to investigate the possible existence of inhomogeneities and other defects in an epoxy resin system, and the role these defects play in the mechanical and electrical failure of the polymer.

Mie Theory was used in the analysis of the data throughout this thesis. Ultra clean fully degassed samples were prepared to ensure any scatterers observed were inherent to the sample.

It was discovered that inhomogeneities and microvoids do exist in the fully cured and degassed ultra clean samples before stressing. Reproducible trends in inhomogeneity behaviour were observed on stressing, and a three phase model of inhomogeneity has been proposed to explain this behaviour. This consists of a densely crosslinked core of mainly diester crosslinks, surrounded by a less densely crosslinked network containing more ether crosslinks. These regions are then interconnected by a weaker even less densely crosslinked matrix where it is proposed that initial yield occurs followed by eventual failure.

Voids present in the network were observed to grow in a similar manner under both mechanical and electrical stress. This suggests a possible link in the deformation processes under either stress. On release of both types of stress, relaxation occurred and the voids reduced in size although some hysteresis was observed. One distribution of voids reached a plateau in size with applied electrical and mechanical stress and this suggests that not all defects have the potential to cause failure.

No wholly reproducible trends were observed for the samples that underwent electrical stress. A common observation was a step type of behaviour that occurred on the release of stress, and also during stressing around a field value of $2.0 \times 10^6 \text{ kV m}^{-1}$. The latter has been attributed to failure occurring at the pin tip epoxy interface causing relaxation in the scattering volume. The overall behaviour with applied stress varied from sample to sample and has been attributed to complicated mechanical and electrical forces present and the remoteness of the scattering volume from the pin tip. The scattering volume, however is very much affected by what is occurring at the pin tip.

It is concluded that the defects present in the epoxy resin do play an important role in the deformation and failure of the polymer. The deformation process under both electrical and mechanical stress are thought to be the same and the deformation under electrical stress results from the mechanical force associated with the electric field.

CHAPTER 1.

INTRODUCTION.

1.1 General Introduction:

Epoxy resins and their composites represent an important group of highly crosslinked amorphous thermosetting polymers. They possess excellent mechanical strength and electrical insulation properties and have a high resistance to chemical attack. They are used extensively in the aerospace and power industries, often in harsh environments [1]. They also have commercial applications as adhesives [2], and have been considered for use in radioactive waste disposal [3]. Surprisingly, little is known of the detailed network structure of these resins, their intrinsic defects and the role these might play in the mechanisms of the mechanical and electrical failure of the system.

Previous work has attempted to determine the presence of microstructure in polymers [4-18]. However, in most cases, inappropriate or ill defined methods of preparation have been used. Under these circumstances it is impossible to know whether any intrinsic defects are present and if they are involved in the deformation

and failure processes of the network.

This work has set out to examine the network structure and determine if intrinsic defects exist in an epoxy resin system. Also how these defects influence the mechanical and electrical performance of the polymer.

1.2 Chemistry of Epoxy Resins

A number of different epoxy resins and curing reagents exist. The morphology of the final fully cured networks will depend on the crosslinking reactions applicable to the polymer.

The epoxy resin system used in this work is phthalic anhydride (PA) cured diglycidyl ether of bisphenol A (DGEBA). The chemical structures of these components are given in Fig 1.

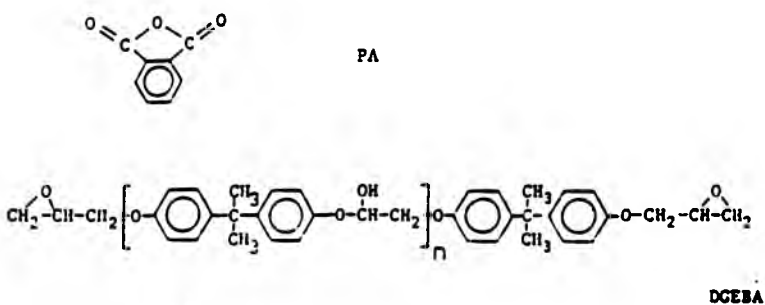



Fig. 1. Chemical formulae of resin and hardener used.

There are two common types of curing reagent available for use with DGEBA. These are anhydrides such as the



one used and also multifunctional amines. Studies on the crosslinking of both types of cured system have been made [10,19-22]. In general homogenous crosslinking reactions were observed to occur in amine cured systems whereas anhydride systems were inhomogeneous. Even if a homogeneous reaction is predicted for a system the resulting network may still contain inhomogeneities. The final network will depend on how the system is cured. Charlesworth [22] observed a cloudiness in his amine cured system when in solution with chloroform. This he suggested was due to the fragmentation in solution of a macrogel. However it could equally have resulted from the presence of microgels in the matrix [10]. Some neutron scattering results [28-29] have suggested that inhomogeneities are present in the amine cured systems as will be discussed later.

1.3. The Evidence for Microstructure.

If microstructure exists there are a number of techniques that are able to elucidate this. These are either direct, such as electron and optical microscopy, or indirect such as X-ray, neutron and light scattering.

Electron microscopy has been used to determine the possibility of microstructure and inhomogeneities have been observed to exist. These have been described as

nodules and have been observed by various authors [4-6,17]. 'Nodules' are considered to be areas of higher density and these give both topological and density contrast.

Fracture surfaces examined by scanning electron microscopy (SEM) have shown 'nodules' on the surface with evidence that the surrounding matrix has undergone localised 'flow' and deformation around the 'nodules' [6], the 'nodules' remaining undeformed. This indicates these nodular areas do not contain as many defects or are less able to deform than their surroundings. Some nodules have been seen to align in the direction of crack propagation [4].

The size of nodules seen depend on the type and amount of curing agent for the system and the average length and number of potential crosslinking sites in the epoxy prepolymer [5,7,18,19]. Most sizes of inhomogeneity were observed to lie in the range of 10-100nm and inhomogeneities in the PA-DGEBA epoxy resin system should be at the larger end of the range [7]. The microstructure observed by electron microscopy could however simply be an artifact of the technique [23,24]. One study uses a defocussing technique [7] for which nodules can appear to be present even in samples in which microstructure is known not to exist [24]. Electron microscopy is a technique that can only look

at surfaces or thin films thus it cannot unequivocally establish if the structures found are representative of the bulk of the material. Therefore other techniques are required to give further evidence of microstructure within the bulk of the material.

Electromagnetic scattering experiments should establish the existence of bulk microstructure, however only a small number have been reported [10-15,25,26]. Earlier light scattering work on DGEBA resins [11,12] has shown pre-existing order in the epoxy resin prepolymer. There is the possibility that inhomogeneity develops during cure from the molecular aggregates formed by intermolecular hydrogen bonding [9-12]. SAXS (small angle X-ray scattering) examination of an amine cured system has indicated that the excess low angle scattering could be due to inhomogeneities of colloidal dimensions (~100nm) [13]. Uhlman et al. [14,15] found a similar excess in low angular X-ray scattering which again could be due to the presence of inhomogeneities of the size found under electron microscopy in the range 30-800nm. This could also be as a result of scattering from microvoids or impurities in the resin. To date SAXS has failed to report unambiguously the presence of inhomogeneities.

Some d.s.c. (differential scanning calorimetry) results [16] have shown that there exists two

inflections in the heat flow temperature curves, that is there are two values for the glass transition temperature (T_g) for an epoxy resin. This suggests a network of two phases which could be due to a transition from glass to rubber occurring first in a less crosslinked region of the resin, followed by a transition in a more highly crosslinked region. However more knowledge of the polymer is required to state whether this is true or not as there are many other factors which influence glass transition behaviour [18] such as molecular weight and physical ageing.

Small angle neutron scattering has been carried out on deuterated epoxies to establish if non-random crosslinking exists in the cured system [27-29]. These studies have been on amine cured DGEBA, and the findings were not in complete agreement. Wu and Bauer [28,29] suggest that order within the range of 0.3-10 nm exist in the resin they studied. However Bai [27] failed to observe any inhomogeneity but this work only studied a monodisperse prepolymer system of one oligomer value which would lend itself to produce a more evenly crosslinked system due to the even spacings of the hydroxyl groups.

1.4 EPOXY FAILURE AND FRACTURE

If inhomogeneities exist in a network then it is expected that there will be evidence of this in the network failure and on the fracture surfaces. The behaviour observed macroscopically will relate to the microstructure of the sample. Detailed studies on the macroscopic properties of polymers such as yield stress and deformation processes have been made with little reference to the microstructure of the test samples.

For many materials failure of the sample occurs at a certain defined stress value inherent to that material. Fracture strength for polymers also depends on the testing conditions applied, especially the rate of loading [30]. The observed strength of a polymer is usually lower than that expected theoretically. This gives rise to the idea that there exist inherent flaws in polymer networks [31].

Griffith [31] proposed an equation for macroscopic observations relating the fracture stress σ_f to a flaw size a , that is:

$$\sigma_f^2 = 2E\gamma/\pi a \quad (1)$$

where

E = Young's Modulus

γ = Energy required to create a unit area of fracture surface

This assumes that

- (i) The solid is an isotropic linear elastic continuum.
- (ii) A flaw size 'a' exists within the solid
- (iii) An energy balance is maintained in the system.

This means the increase in potential energy due to the surface energy of the extended crack must be balanced by the decrease of the potential of the strain energy.

This theory therefore assumes total brittle fracture with no energy terms appropriate to viscoelastic or plastic deformation around the flaw. However work on the fracture of epoxy resins [32] shows that a small amount of plastic deformation occurs before failure, but the Griffith Theory still applies if a correction is made. The correction is to replace V with V_p which allows for a small amount of plastic deformation to occur [33]. One drawback of this theory is that it does not take into account the microscopic fracture processes occurring at the crack tip. Although these equations are used with the epoxy resins, the model is restricted by the fact that it assumes the plastic zone size does not disturb the stress field distribution of the whole sample. This may not be the case and further corrections should be made for this. This will be referred to later in this work.

It has been suggested that there is some plastic deformation involved in the failure of epoxy resins [32]. If plastic deformation is localized, two types of deformation process can occur. These are:

- (i) shear yielding
- (ii) crazing.

Shear yielding involves plastic deformation without a change in the volume of the sample. The two microprocesses of shear [33] are,

- (i) under stress, disc shaped sheared regions are thermally activated
- or (ii) there are thermally activated 'kinks' in the matrix.

In many cases shear bands lead to crack initiation by the nucleation of microvoids at their intersections. Groups of shear bands can stabilize to form a craze structure. Below T_g voids have been found to grow into more elliptical shapes [33] inducing a stress concentration in the surrounding material which initiates more voids and leads to crazing.

Unlike shear yielding, crazing involves an increase in sample volume. Crazing is initiated when an applied stress causes microvoids to nucleate at a point of high stress. Locally these could be areas of local inhomogeneity, defects, and as already mentioned shearbands. Crazing involves the cavitation of the

sample (see fig 2) and the formation of fibrils. These fibrils are stable, therefore the voids do not coalesce and form a crack until a critical stress is reached that breaks the fibrils. Crazing occurs readily in thermoplastics but becomes less likely in more densely crosslinked material, although some authors have suggested that epoxies fail this way [6,34-36]. The extension of the craze fibrils in a highly crosslinked network will be smaller than for thermoplastics [32].

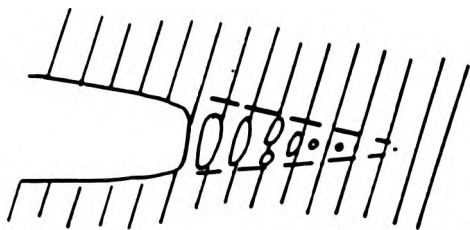


Fig 2 . Craze structure.

A typical stress-strain curve [32] of an epoxy undergoing uniaxial tensile stressing is given in Fig. 3. It exhibits a linear region before yield which is reversible. On release of the stress the material will return to its original condition. In contrast, nonlinear stress strain behaviour, may be observed when

the material exhibits visco elastic behaviour and if local yield occurs the deformation will not be completely reversible. i.e. the strain will not recover. Relatively shortly after yield the polymer fractures and this behaviour is consistent with all thermosetting polymers.

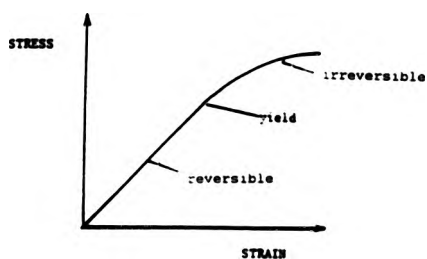
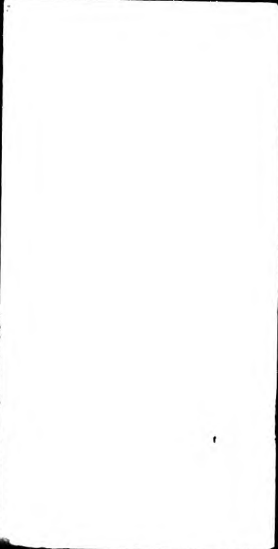


Fig 3 . Stress strain curve for an epoxy resin undergoing tensile stress

The fact that epoxy resins fail before they reach their theoretical strength implies that they contain flaws. The flaws that Griffith describes are voids, these may pre-exist in the network or be generated by yielding processes. Non-linear deformation and yield will be influenced by voids and also network inhomogeneity, and weak network sites may act to nucleate voids.

If defects such as microvoids and inhomogeneities are

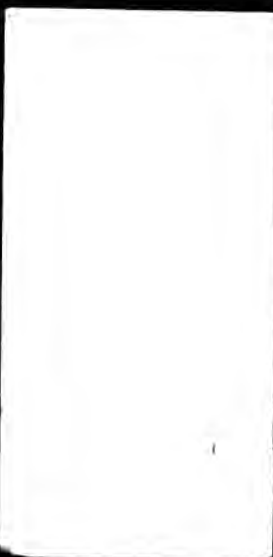


present in the epoxy resin then the fracture surface observed could show evidence of these defects and will have certain typical features indicating their existence.

The fracture surfaces of epoxy resins show three distinct regions [32,37,38] these are:-

- (i) initiation region, a coarse surface may exist at the actual source of the crack.
- (ii) Smooth mirror region, here the crack velocity is low and the resulting surface smooth.
- (iii) Fast crack growth region. This is a more rugged region and the direction of propagation can change suddenly.

The direction of crack growth can be seen from the river markings on the surface. Bands on the surface show where crack arrest has occurred [6,32,39] indicating that unstable crack growth can occur. Both stable and unstable (slip-stick) type crack growth have been reported [8,40-41], and is dependent on temperature and the conditions of crack propagation. If an inhomogeneous network exists then it might be expected that the sample will deform in an inhomogeneous manner as is suggested by the possibility of stable and unstable crack growth. A model of an inhomogeneous system, consisting of polystyrene latex spheres in a polystyrene matrix, has been made and the nature of the



fracture surface investigated [42,43]. It was shown that the surface morphology exhibited the structure expected from the bulk of the resin. Samples containing no microgel spheres showed no structure. Consequently, if in epoxy networks strong inhomogeneity exists we would expect to see evidence of this on fracture surfaces.

1.5 Electrical Breakdown and Treeing

Resins are widely used in high voltage equipment as insulators, therefore it is important to understand how epoxy resins deteriorate with time under electrical stress. Initially it may appear that failure processes under electrical stress would be different from those under mechanical stress. However recent work [44-45] has suggested that this may not be so and that fracture mechanics could be applied to the electrical stress situation [45] and that the breakdown of the polymers may be due purely to the mechanical stresses associated with the electrical stress conditions [45]. If these ideas are correct it would be expected that a link would exist between the mechanical and electrical failure processes and microstructure.

Previous work has shown that polymers placed under electrical stress fail by the growth of branched breakdown channels [44-53]. These are known as

trees and usually develop from localized areas of high electric stress eg.voids and conducting inclusions.

The rate of tree growth depends on the size of applied field. Growth is also expected to be faster for alternating fields [45] than static fields as the alternation between bombardment and extraction of electrons may cause earlier fatigue in the sample. This suggests that it is the bombardment of electrons on the polymer that weakens the matrix.

However the failure processes occurring in the polymers under breakdown are not well understood. It has been suggested [44] that treeing from voids begins through the action of partial discharge within the void. Void initiation and treeing could occur from damage caused by the injection of high energy electrons into the system on the negative cycle of the alternating voltage. Above a certain critical energy the electrons receive more energy from the electric field than they can dissipate within the bulk, therefore breakdown will occur at this critical field value [45]. Some of the electrons may be trapped, and some may cause ionization, producing molecular decomposition in the sample producing gas filled cracks and microvoids. Thermal breakdown could occur through Ohmic heating by the conduction current within the sample. Electro-mechanical breakdown may occur within

the sample when the electrostatic (Maxwell) force exceeds the elastic force resisting breakdown [45].

A recent suggestion has been that the treeing initiation may be purely mechanical, caused by the electrostatic-vibrational deformation of the pin tip in the resin system [44], and has shown that trees occur if a purely mechanical vibrational force is applied to the pin tip.

One or more of these processes could occur in the epoxy resin under electric stress resulting in the initiation of treeing processes, and possibly contributing to their propagation.

The process of electrical failure can be studied using a pin/plane configuration of electrodes. The pin is usually embedded within the sample. This configuration produces a highly divergent electric field at the pin tip. Very high field values can be obtained at the pin tip for relatively low applied voltages, so that breakdown should occur over a relatively short period of time at low voltages.

Previous work [46-49], monitoring void growth and treeing by optical microscopy and using the pin/plane configuration described, has shown that the void growth does occur with applied a.c. fields. The work also found that void growth is dependent on time and size of field applied. Under low stresses 'harmless' voids may be present that do not lead to failure by treeing.

Above a certain stress value of $3 \times 10^8 \text{ Vm}^{-1}$, void growth did lead to treeing and failure of the sample (see Fig.4). This suggests that some form of local yield may occur to produce voids which can support treeing. If this is so the value of $3.0 \times 10^8 \text{ Vm}^{-1}$ could be viewed as a material value and similar values must exist for other polymers.

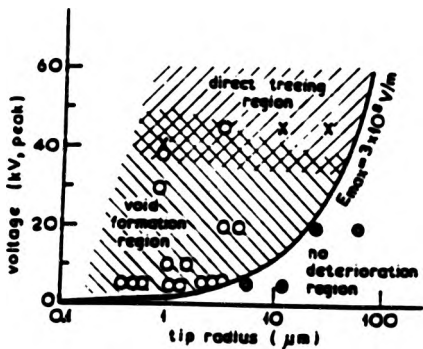


Fig 4 Shibuya's figure showing value of E_{max} above which harmful void growth can occur [49].

Even notionally void free samples were found to degrade under the applied stress. However, only optical microscopy was used, therefore it is impossible to judge if the sample was void free on a size below that discernible optically. Also void growth could not be monitored before the voids had reached optically resolvable dimensions. The relationship of time of void

growth and maximum applied field was found to be

$$E_{\max}^4 \times t = 8 \times 10^{37} \text{ v}^4 \text{ m}^{-4} \text{ h} \quad (2)$$

This work by Shibuya and Calderwood [46-49] has been used as the starting point for the electrical work carried out for this thesis in estimating the applied fields used to attempt to obtain void initiation and growth in a few hours. Work in this thesis has attempted to obtain information on sizes of voids smaller than those observed optically. Therefore a technique is required to do this. There now follows a discussion on the techniques available for this.

1.6 BULK SCATTERING TECHNIQUES.

It is possible that many levels of structure exist within the epoxy resin. These range from an ideal network through to large scale ordering. The limit of distinguishable order is that of thermal density fluctuations [10-12,54]. Molecular ordering will result in a density difference between the ordered molecules and surrounding medium. This density difference resulting from the ordering can be detected using scattering techniques.

As opposed to electron microscopy, scattering techniques give information from within the bulk of the material. Various scattering techniques are available, whilst the most common include Xray, neutron and light scattering. In this study light scattering has been

used to determine the presence of inhomogeneities in the epoxy resin, as the expected size of the inhomogeneity falls into the range applicable to light scattering. Small Angle X-ray Scattering (SAXS) was also attempted on the resin samples. However this was unsuccessful due to the absorption of the X-rays in the relatively thick films used. Also there was little difference in contrast between the inhomogeneity and surrounding medium for the scattering of X-rays to take place. It would have been possible to have attempted to produce thinner films to reduce the absorption of the X-rays. However this would mean that we could no longer assume that we were observing a bulk property of the sample, and the results would therefore be irrelevant to this thesis.

1.7 SUMMARY

It can be seen that evidence for microstructure existing in epoxy resins is mounting. However more conclusive data is still required in determining the existence of inhomogeneities and the role they play in the failure of the polymer. There also exists the possibility that voids exist in the network either through areas of trapped air, inherent voids in the matrix, or from volatile impurities. Bulk scattering offers a better technique to microscopy to determine

the presence of inhomogeneities and microvoids within the bulk of the polymer.

As epoxy resins are an important group of polymers it is necessary to understand their network structure and type of defect they possess. To date little is known of their network structure but there is mounting evidence that microstructure does exist in the resin. However there is a need to specify the sample preparation to ensure that the structure observed is not simply a result of sample preparation.

The aim therefore of this work is to establish, using light scattering, the presence of microstructure in the PA-DGEBA system; to determine if its presence is detrimental in terms of the polymers performance under mechanical and electrical stress. Also to link the structure to the macroscopic deformation processes such as yield and void growth, and to investigate the possibility that the processes initiating failure are the same for both mechanical and electrical stressing.

CHAPTER 2.

LIGHT SCATTERING THEORY

2.1 INTRODUCTION

All matter consists of discrete electrical charges. The electric charges within the scattering medium will be set into oscillatory motion by an incident electromagnetic field, such as visible radiation. These accelerating charges will cause a reradiation of light in all directions. This reradiation of the incident light will be seen as scattered light from the object containing the dipoles. An alternative explanation to the scattering of light was developed separately [55,56]. This states that the scattering by a system is related to the inhomogeneity of that system. Inhomogeneities cause density differences in the system which give rise to differences in refractive index. Any incident light will then be scattered by the differential refractive index.

If it is the inhomogeneity of the sample that causes the light to scatter, then the scattered light will contain information on the inhomogeneity. Much work has been done on interpreting light scattering from inhomogeneous systems. It has been found that the

angular scattering intensity gives information on the size and number of scatterers (ie inhomogeneities) present, provided they are above $0.02\mu\text{m}$ in size. This limit is set by the resolution of the system.

Scattering from low concentrations of scatterers only will be considered here as this is relevant for the likely concentrations of scatterers in the resin samples [11,12]. Higher concentrations cause multiple scattering between the particles so changing the scattering profile making it impossible to analyse for size and concentration [57].

In order to be able to obtain the size of the scatterer from the angular scattering profile, the theoretical scattering profiles have been calculated [55,56] from Maxwell's Electromagnetic equations [58], for different scatterer size and various differential refractive indices. Two theoretical approaches relevant to the scattering from the epoxy resin have been developed from Maxwell's equations, these are the Model Approach and the Statistical Approach. Both will be discussed in this chapter and their usefulness determined.

If we consider light as a scalar wave moving in a direction z (fig 5)

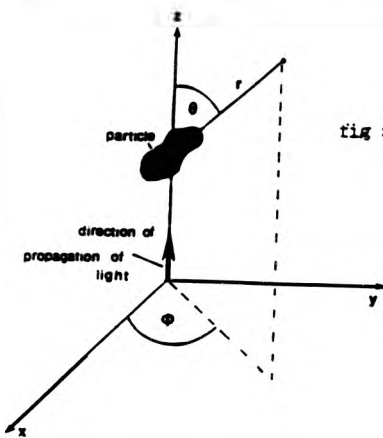


fig 5. Scattering by an arbitrary particle.

then the incident wave may be written as

$$U_0 = e^{-i(kz - \omega t)} \quad \dots(3)$$

the scattered wave may be written as

$$U_s = S(\theta, \phi) e^{-i(kr - \omega t)} \quad \dots(4)$$

$S(\theta, \phi)$ is the scattering amplitude,
 $\omega = 2\pi f$, f is the frequency of the incident wave
and $k = 2\pi/\lambda$

θ and ϕ are defined in fig 5

Combining the two equations gives

$$U_s = \frac{S(\theta, \phi)}{ikr} e^{-ik(r-z)} \cdot U_0 \quad \dots(5)$$

The intensity is related to the scattered wave by

$$I = |U|^2 \quad \dots(6)$$

therefore the scattered intensity is given by

$$I_{sca} = S^2(\theta, \phi) \frac{I_0}{k^2 r^2} \quad \dots(7)$$

Further more as light is a transverse wave it can be polarised or unpolarised. If light is unpolarised it can be resolved into two independent plane polarised

states. The relationship between the scattered and incident fields then becomes

$$\begin{pmatrix} E_{1s} \\ E_{rs} \end{pmatrix} = \frac{e^{ik(r-z)}}{-ikr} \begin{pmatrix} S_2(\theta, \Phi) & S_3(\theta, \Phi) \\ S_4(\theta, \Phi) & S_1(\theta, \Phi) \end{pmatrix} \begin{pmatrix} E_{1l} \\ E_{1r} \end{pmatrix} \dots (8)$$

E_{1l} is the incident field polarised parallel to the scattering plane and

E_{1r} is the incident field polarised perpendicular to the scattering plane.

$S(\theta, \Phi)$ has now been replaced by a scattering matrix where for a totally symmetrical particle $S_3(\theta, \Phi) = S_4(\theta, \Phi) = 0$.

It then follows that for a symmetrical particle

$$E_{1s} = S_2(\theta) \frac{e^{-ik(z-r)}}{ikr} E_{1l} \dots (9)$$

and

$$E_{rs} = S_1(\theta) \frac{e^{-ik(z-r)}}{ikr} E_{1r} \dots (10)$$

therefore the intensity for light polarized perpendicular to the scattering plane is

$$I = \frac{|S_1(\theta)|^2}{k^2 r^2} I_0 \dots (11)$$

and for light polarized parallel to the scattering plane

$$I = \frac{|S_2(\theta)|^2}{k^2 r^2} I_0 \dots (12)$$

These basic relationships may be used as the basis for

solving light scattering problems.

2.2 RAYLEIGH SCATTERING

The simplest theory developed was that by Rayleigh for very small particles. The diameter of these should be $< \lambda/20$ [39,40] for the theory to be valid, where λ is the wavelength of the incident beam in the scattering medium. It is appropriate to discuss this theory first as it provides a basis for the other scattering theories. It is important to this thesis as it is relevant for the scattering from liquids which have been used to calibrate the light scattering photometer.

For very small scatterers whose size is very much smaller than the wavelength of the incident light, the particles can be considered to act as point scatterers.

Hence they will scatter light equally at all angles in the scattering plane.

Many authors use the 'Rayleigh Ratio' in their analysis which is related to the scattered intensity by equation (13). The Rayleigh Ratio is a material constant and is independent of the scattering photometer used.

$$R(\theta) = \frac{I_s}{I_o} r^2 \sin(\theta) \quad \dots(13)$$

I = scattered intensity

I_o = incident intensity

r

r = distance between scatterer and point of detection.

θ = scattering angle.

$R(\theta)$ is a constant for each angular value and depends only on the scattering medium, this value will now be used in place of intensity.

Rayleigh calculated an expression for the scattered intensity for 'N' small independent isotropic scatterers [59] given by equation (14), for unpolarized light.

$$I = \frac{8\pi^2}{r^2} \frac{a^6}{\lambda^4} \left(\frac{n_1^2 - n_2^2}{n_1^2 + 2n_2^2} \right)^2 (1 + \cos^2 \theta) \quad (14)$$

a = scatterer radius

n_1 = refractive index of medium

n_2 = refractive index of scatterer

λ = wavelength of the incident light in the scattering medium.

For vertically polarised incident light and light scattered in the horizontal plane, with $\theta = 90^\circ$, the Rayleigh Ratio is:-

$$R(90^\circ) = \frac{16\pi^2 a^6}{\lambda^4} \left(\frac{n_1^2 - n_2^2}{n_1^2 + 2n_2^2} \right)^2 N \quad \dots (15)$$

The scattered unpolarised light consists of a horizontally and vertically polarized contribution (Fig. 6). For isotropic scatterers and vertically polarized incident light however the horizontal scattering component will be zero. However a correction needs to be applied to (15) if the scatterers are

anisotropic. This is known as the Cabannes factor and the form of which for vertically polarised incident light is given by (16) [73,74].

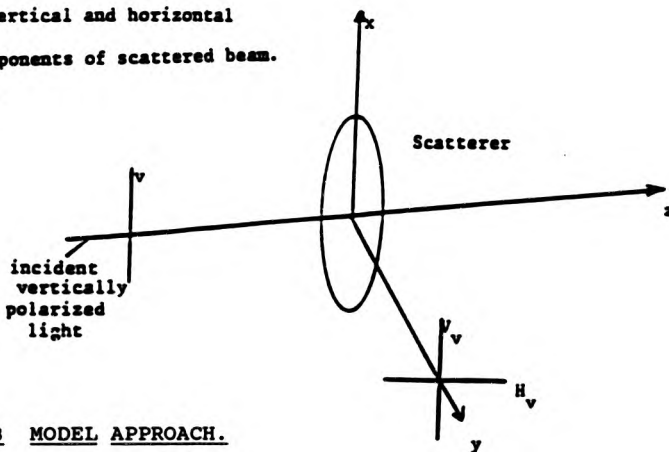
$$C_v = 6 / (6 - 7 \Delta_u) \quad \dots(16)$$

Δ_u = the ratio of the horizontal and vertical components of the scattered light intensity (H/V) for unpolarised incident light.

The Rayleigh Ratio is then given by

$$R(90^\circ) = \frac{16\pi^4 a^6}{\lambda^4} \left(\frac{n_i^2 - n_f^2}{n_i^2 + 2n_f^2} \right)^2 N C_v \quad \dots(17)$$

Fig. 6. Vertical and horizontal components of scattered beam.



2.3 MODEL APPROACH.

This approach involves the calculation of a theoretical scattering amplitude for the scatterer ($S(\theta)$) [55,56] at a certain angle for a proposed scatter type, e.g. sphere, coil, rod etc. This

method has been shown to work with systems whose shapes are known [60].

The scatterers in the epoxy resin have been assumed spherical and only theories for spherical particles will be considered and discussed. However the theory has been developed for other shaped scatterers such as ellipsoids and rods [76,77].

2.3.1. Rayleigh Gans Debye (RGD) Scattering.

For larger particles $> \lambda/20$ but with a low refractive index variance so that $|m-1| \ll 1$ and

$2ka |m - 1| \ll 1$ still hold (m is the ratio of the refractive index of scatterer and medium and k has its usual meaning of $2\pi/\lambda$, λ is the wavelength of light in vacuum). Then the RGD scattering calculations apply. The scatterers can no longer be considered to act as point scatterers, however, each volume element can (Fig 7.).

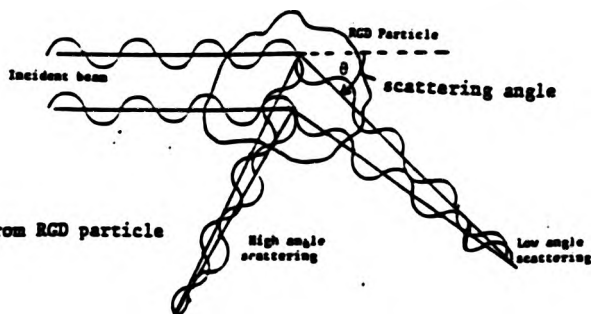


Fig. 7. Scattering from RGD particle

Because of the different spatial positioning of the scatterers, each scattered element has a different phase to the others and interference occurs between the scattered fields, so the intensity of the angular scattered radiation is reduced relative to that of the Rayleigh particle due to the interference. This effect is greater at higher angles as shown in Fig. 7.

The Rayleigh theory needed to be modified for these larger scatterers [55,61]. This was achieved by means of a form factor $P(\theta)$. This is an expression dependent upon the shape of the scatterer.

For a spherical particle the form factor is:-

$$P(\theta) = \left\{ \frac{3}{u} (\sin(u) - u \cos(u)) \right\}^2 \quad \dots (18)$$

where $u = 2k a \sin(\theta/2)$.

So the expression for the Rayleigh Ratio for N RGD scatterers is:

$$R(90^\circ) = \frac{16\pi^4 a^6}{\lambda^4} \left| \frac{n_1^2 - n_2^2}{n_1^2 + 2n_2^2} \right|^2 N c_v P(90^\circ) \quad \dots (19)$$

Previous work on the range of validity of the RGD theory [55,62] has shown that it will be valid for inhomogeneities in the resin provided they are no larger than $0.5 \mu\text{m}$ [62]

This theory is not valid for scattering from voids unless they are $\ll \lambda/20$, due to the large difference in refractive index between voids and surrounding network.

2.3.2. MIE THEORY OF SCATTERING

For even larger particles the RGD theory does not hold and a more rigorous method of analysis is required [63].

Mie [64] solved Maxwell's equations [65] for light scattered from a spherical particle. A solution for the scattering vectors $S_{1,2,3,4}$ exists for spheres of arbitrary size and given differential refractive index. A detailed derivation of the theory is given in Van de Hulst [40] and only the essential results will be quoted here.

The two scattering amplitude functions for horizontally S_2 and vertically S_1 polarized light are complex and given respectively by:

$$S_1(\theta) = \sum_{n=1}^{\infty} \frac{2n+1}{n(n+1)} \left[a_n \pi_n(\cos \theta) + b_n \tau_n(\cos \theta) \right] \quad (20)$$

$$S_2(\theta) = \sum_{n=1}^{\infty} \frac{2n+1}{n(n+1)} \left[b_n \pi_n(\cos \theta) + a_n \tau_n(\cos \theta) \right] \quad (21)$$

where

$$a_n = \frac{x \psi'_n(y) \psi_n(x) - y \psi'_n(x) \psi_n(y)}{x \psi_n(y) \zeta_n(x) - y \zeta_n(x) \psi_n(y)} \quad (22)$$

$$b_n = \frac{y \psi'_n(y) \psi_n(x) - x \psi'_n(x) \psi_n(y)}{y \psi_n(y) \zeta_n(x) - x \zeta_n(x) \psi_n(y)} \quad (23)$$

$$\pi_n(\cos \theta) = \cos \theta \cdot \frac{2n-1}{n-1} \cdot \pi_{n-1}(\cos \theta) - \frac{n}{n-1} \pi_{n-2}(\cos \theta) \quad (24a)$$

$$\tau_n(\cos \theta) = \cos \theta [\pi_n(\cos \theta) - \pi_{n-2}(\cos \theta)] - (2n-1) \sin^2 \theta \cdot \pi_{n-1}(\cos \theta) + \tau_{n-2}(\cos \theta) \quad (24b)$$

where ψ_n and ζ_n are given by

$$\psi_n(z) = (\pi z/2)^{1/2} J_{n+1/2}(z) \quad (25a)$$

$$\zeta_n(z) = (\pi z/2)^{1/2} H_{n+1/2}^{(1)}(z) \quad (25b)$$

these are the Ricatti-Bessel functions [61] (see next section for further details). τ_n and τ_n are Legendre polynomials. From the values of $S_1(\theta)$ and $S_2(\theta)$ the scattered intensity can be calculated as follows:-

$$I_s = \frac{|S_1(\theta)|^2 + |S_2(\theta)|^2}{4k^2 r^2} I_0 \quad (26)$$

The advantages of Mie theory are:

- (i) the process of fitting the data doesn't involve Fourier transforming the data as required by the Statistical Theory (see later in this chapter).
- (ii) it will fit to voids and inhomogeneities of any size provided that they are not smaller than 10nm.

The main disadvantage is that it will only fit data for spherical scatterers. The theory is for a single size of scatterers whereas a distribution will be present in the epoxy resin. It is however possible for the theory to be modified to fit to a bimodal distribution.

2.4 DATA FITTING AND ERROR ANALYSIS

A Fortran programme was written and run on a VAX mainframe computer in order to fit the data obtained from the light scattering system to the most

appropriate theoretical Mie scattering profile. A flow diagram of this programme is given in fig 8.. This was achieved by using a non-linear least squares fitting routine E04PDF available on the VAX nag library. This routine minimised the difference between the actual data and theoretical values using an iterative process and decreasing steps in the varying parameter, which was the size of scatterer.

The theoretical values were calculated from recursion relations as will now be discussed.

The main difficulty in using the Mie formulae is the requirement of summations to infinity to calculate a_n and b_n (equations (27) and (28)). It is possible to perform these calculations using recursion relations [66]. These are

$$a_n = \frac{\left(\frac{A_n(\gamma)}{m} + \frac{n}{x}\right) \operatorname{Re} \{\zeta_n(x)\} - \operatorname{Re} \{\zeta_{n-1}(x)\}}{\left(\frac{A_n(\gamma)}{m} + \frac{n}{x}\right) \zeta_n(x) - \zeta_{n-1}(x)} \quad (27)$$

$$b_n = \frac{\left(mA_n(\gamma) + \frac{n}{x}\right) \operatorname{Re} \{\zeta_n(x)\} - \operatorname{Re} \{\zeta_{n-1}(x)\}}{\left(mA_n(\gamma) + \frac{n}{x}\right) \zeta_n(x) - \zeta_{n-1}(x)} \quad (28)$$

These recursion relations breakdown for sizes of scatterer larger by more than ten times than that expected to be present in the epoxy resin $>10\mu\text{m}$. [11-12].

A_n and ζ_n can be generated using the following

recurrence relations:

$$A_n(y) = -\frac{n}{y} + \left(\frac{n}{y} - A_{n-1}(y) \right)^{-1} \quad (29)$$

$$A_0(y) = \cos y / \sin y \quad (30)$$

$$\zeta_n(x) = \frac{2n-1}{x} \zeta_{n-1}(x) - \zeta_{n-2}(x) \quad (31)$$

$$\zeta_{-1}(x) = \cos x - i \sin x \quad (32)$$

$$\zeta_0(x) = \sin x + i \cos x \quad (33)$$

where $x = 2\pi a/\lambda$ and $y = mx$

$\pi_n(\cos \theta)$ and $\tau_n(\cos \theta)$ were calculated from equations (24) and (25) using the following.

$$\pi_0(\cos \theta) = 0 \quad (34)$$

$$\tau_0(\cos \theta) = 0 \quad (35)$$

$$\pi_1(\cos \theta) = 1 \quad (36)$$

$$\tau_1(\cos \theta) = \cos \theta \quad (37)$$

$$\pi_2(\cos \theta) = 3 \cos \theta \quad (38)$$

$$\tau_2(\cos \theta) = 3 \cos 2\theta \quad (39)$$

$S_1(\theta)$ and $S_2(\theta)$ were calculated but $S_1(\theta)$ was used for the fitting of the data as vertically polarised light was used.

n is the number of terms needed for the summations to converge. These recursion relations have been used throughout to fit all the scattering profiles from the epoxy resins.

The data obtained from the light scattering system is that of the mean scattered count (I_{sca}) and its standard error (s_{sca}) for each angle. These are the values obtained from the photon counting system. Simultaneously as I_{sca} and s_{sca} were obtained from the scattering system, a mean reference beam count I_{ref} and its standard error s_{ref} were also obtained (see appendix on how the mean and standard errors were calculated). A reference was used so that any variation in incident intensity over the data collection period could be corrected. This was achieved by dividing the scattered beam count by the reference beam count. The angular intensity is then

$$I_i = \frac{I_{sca}}{I_{ref}} \quad \dots(40)$$

The error on the value I_i was then calculated from the standard error on each of the mean counts, by initially calculating each error as a percentage error on each of the mean counts so that

$$s_{sca\%} = \frac{s_{sca}}{I_{sca}} \times 100 \quad \dots(41)$$

and $s_{ref\%}$ was calculated in the same way.

The percentage error $s_{i\%}$ of I_i was then obtained from the sum of the percentage errors on the reference and scattered counts.

$$s_{i\%} = s_{refi\%} + s_{scati\%} \quad \dots(42)$$

Therefore the total error s_i of I_i is

$$s_i = s_{i\%} \cdot I_i / 100 \quad \dots(43)$$

I_i is related to the actual scattering intensity by an unknown factor. In order to fit the data to the theoretical profile the actual data (I_i) was normalised to unity by dividing all values by the lowest angular data point as this should be the largest value. s_i was also divided by this value. If the data at this point was spurious (eg too large due to dust in the system) then the data was normalised by dividing by the next lowest angular point. A fit using a spurious data point could be determined by a very large value for the sum of squares to the fit on the data, returned by the minimisation routine. Normalisation was made at low angles so that the data range was 0..1, the best range for the use of the minimisation routine E04FDF. Also, as the theoretical data is also normalised at this point to achieve a fit, the best fit of the profile will be at the low angle end. This is where the data for non spherical particles fits closest to Mie theory [67]. However as the largest particles in the system dominate the low angle scattering, it is likely that

the fit will be biased towards the larger scatterers in the system. The usual angular range of data was from 34° to 105° . The minimisation routine was used to minimise the sum of squares (χ^2) of the differences between the theoretical $I(x_i)$ and actual data I , where χ^2 is given by

$$\chi^2 = \sum_{i=1}^{npts} \frac{(I_i - I(x_i))^2}{s_i^2} \quad \dots(44)$$

The value of the sum of squares was weighted by s_i to give the best indication of the goodness of fit. This is a convenient way of rationalising data and being able to compare data from sample to sample. As s_i is the calculated standard error on I_i , then we would expect the difference between the actual and theoretical value to be close also to the value of the error s_i if the fitting error was controlled primarily by the standard error and not the overall scattering envelope. Therefore dividing the square of the difference between the theoretical and the actual value by s_i^2 should give a value of one for each of the values in the sum of squares. Hence for a good fit, the value of the sum of squares should be the value of the number of points used in the fit. For the real data from the epoxy resin, a value above the number of points is expected as the Mie theory only approximates to the actual scattering. Table 1 gives examples of

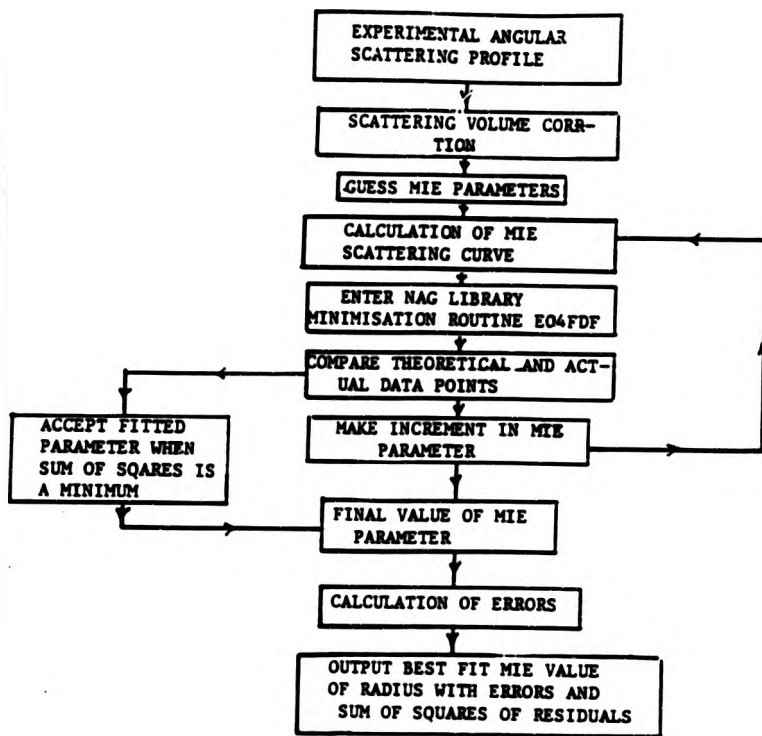


Fig 8. Flow Diagram of fitting routine for Mie Theory.

for various fits from theoretical data ,solutions of polystyrene spheres and actual resin samples. The number of data points for each case was 44. A flow diagram of the computer programme is given in fig. 8.

TABLE 1: Comparison of programme fit for theoretical and actual data

SAMPLE	VALUE OF DIAMETER/ μm	SUM OF SQUARES χ^2
Theoretical Mie file 0.3 μm	0.300	3.52×10^{-3}
Polystyrene 0.3 μm	0.304	0.378
Resin void	0.402+/-0.06	198
Resin void	0.301+/-0.02	106

For the theoretical profile and the scattering from the polystyrene spheres the sum of squares is smaller than the number of points. This is due to the fact that the error on the profiles was over estimated so the weighting on the sum of squares too large.

For the epoxy resin there may be more than one type of scatterer present . If we exclude the possibility of foreign bodies being present due to the rigorous sample preparation used (see chapter 4), then there are two types of possible defects present. These are voids and inhomogeneities. There will be a large difference in the differential refractive index between scatterer and

medium for voids and inhomogeneities. Samples were fitted assuming that either a distribution of inhomogeneities or voids were present and the sum of squares compared for both to determine which type of scatterers were present. This was the one for which the value of the sum of squares was the smallest. Table 2 gives some examples of the differences in the sum of squares for the two types of scatterers. The number of points used in the all the fits was 44. Samples 1,2 and 3 contained voids and samples 4 and 5 were considered to contain inhomogeneities.

TABLE 2 Comparison of sum of squares for voids and inhomogeneities (incho.).

sample	size (void) / μm	void χ^2	size (incho.) / μm	incho. χ^2
1	0.469+/-0.16	1730	0.33+/-0.02	3892
2	0.402+/-0.12	1980	0.322+/-0.07	2930
3	0.320+/-0.014	738	0.282+/-0.13	857
4	0.17+/-0.04	259	0.16+/-0.03	173
5	0.16+/-0.042	433	0.144+/-0.033	90

It can be seen that in most cases there is a large difference in the sum of squares on the fits for the two different types of scatterer, and that the type of scatterer present can best be established by the smallest value of the sum of squares. For samples such as No. 3, it is not possible to be unambiguous and other information such as scattering intensity needs to

be considered in order to make a judgement.

The value of χ^2 varies greatly from sample to sample. However for the same sample there is little difference in the value of χ^2 for consecutive data files from the same sample (Table 3).

The consistency of the value of χ^2 for the same sample adds further validity to the use of this value in determining type of scatterer present as it will not change with different data files of the same sample.

Table 3 Value of sum of squares of fit for consecutive files (data fitted to void)

File	size of scatterer / μm	sum of squares
1	0.417+/-0.036	199
2	0.402+/-0.023	198
3	0.412+/-0.033	189
4	0.411+/-0.034	200

The error on the size of scatterer was determined in the programme by the two methods described in the Appendix.

The concentration of scatterers was determined by calculating the 90° Rayleigh Ratio using the calibration obtained for the system from the 90° scattering of well defined liquids (see chapter 3). This value then relates to the number N of scatterers present and the refractive indices of scatterer and

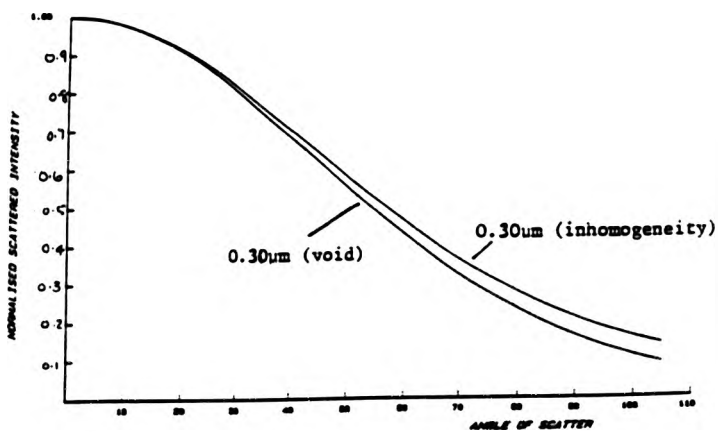


Fig 9. Comparison of angular intensity profiles of voids and inhomogeneities of the same size.

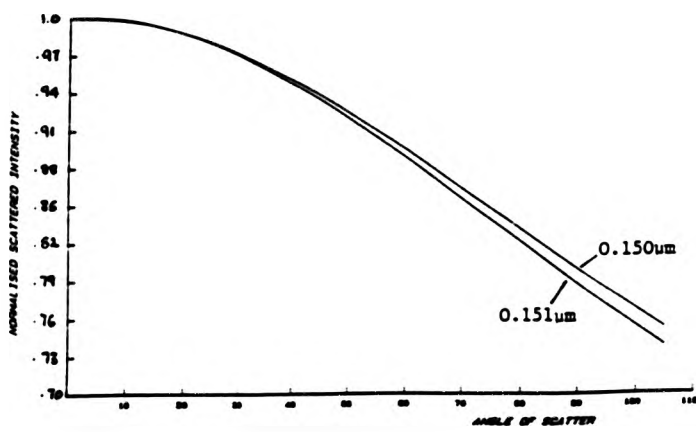


Fig 10. Comparison of angular intensity profiles of inhomogeneities differing in size by 0.001 μm.

medium, provided a correction $K(90)$ is made to allow for the fact that the scatterers are too large to be Rayleigh scatterers. $K(90)$ is calculated from Mie theory and is dependent on the size and relative refractive index of the scatterers. The percentage volume fraction is then calculated using equation 45.

$$R(90^\circ) = \frac{16\pi^4 a^6}{\lambda^4} \left(\frac{n^2 - n_1^2}{n^2 + 2n_1^2} \right)^2 N C_v K(90^\circ) \quad (45)$$

Mechanical stress influences the optical properties [68] of a material such as the bulk refractive index and the birefringence of the system. This has only been considered to affect the depolarization ratio which was monitored throughout the stress cycle with no discernible change in the value of Δ_U . Therefore the scattering amplitude was thought not to change during stress due to these effects.

Figs 9 and 10 show the difference in the normalised theoretical scattering profiles for voids and inhomogeneities of the same size and the same type of scatterers differing in size by 0.001 μm . Showing the differences between the two that the programme can discern. It is important to note that due to the greater differential refractive index for voids in the matrix, these will scatter more light and there will be a very large difference in scattering intensity at 90° between voids and inhomogeneities. This fact was

also used in determining if voids or inhomogeneities were present in the matrix.

2.5 THE STATISTICAL APPROACH

Although the Model Approach works very well for monodisperse systems of known shape, scatterers in a real system are not so well defined. A statistical theory was developed by Ross [69] that would describe the scattering from random density fluctuations such as might exist in a solid polymer, in order to obtain the size and concentration of these scatterers.

This method holds two main advantages,

- (i) a distribution of particle size can be fitted ,and
- (ii) a number of correlation functions can be used to fit to the scatterers to obtain a best fit value of a correlation length.

The work was originally described by Debye [70,71] and further developed by Ross [69]. He derived an expression for the Rayleigh Ratio from Maxwells equations for the scattered light. The flux per solid angle [72] is given by.

$$R(\theta) = \frac{\langle k^3 \langle \delta \epsilon^2 \rangle}{4 \langle \epsilon \rangle^2} \frac{\sin^2(\theta)}{8} \int \rho F(\rho) \sin(\langle k \rangle \rho s) d\rho \quad (46)$$

where

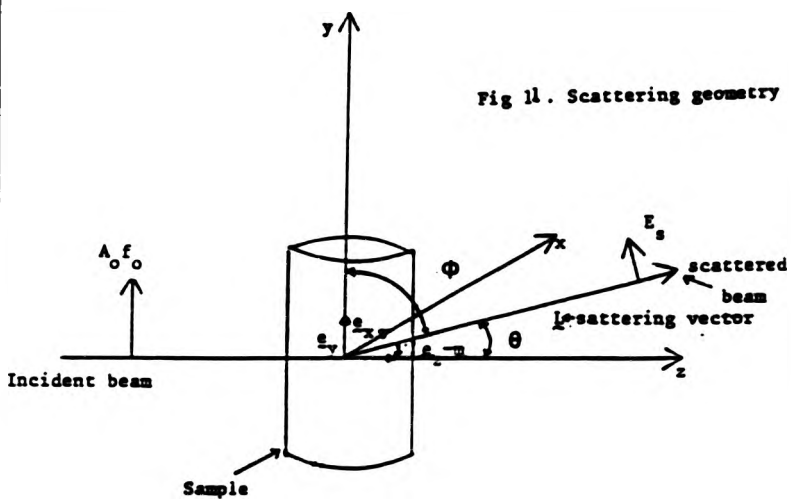
ϵ = permittivity

$s = 2 \sin(\theta/2)$;

$F(\rho)$ = correlation function. Of which Ross quotes
7, an example is F_1

$$F_1 = \exp(\rho/a) \quad (47)$$

ϕ and θ are defined as in fig. 11



This method is valid for determining scatterer size providing the following are true [69,72].

(i) there is no phase change due to the scattering by the particles

i.e. $[\langle \delta\epsilon \rangle / \langle \epsilon \rangle^2] \ll 1 \quad (48)$

(ii) the Fraunhofer approximation holds:

that is, for parallel incident light

$$L \gg \frac{1}{2} \langle k \rangle \eta_{s,coh} \quad (49)$$

$\eta_{s,coh}$ is the coherence distance

L is the distance from the sample to where the intensity is measured

This approach is therefore valid for determining the size of inhomogeneities in the resin matrix, however, it will not hold for determining the size of voids present as the differential refractive index between void and surrounding matrix is too great for (i) to hold.

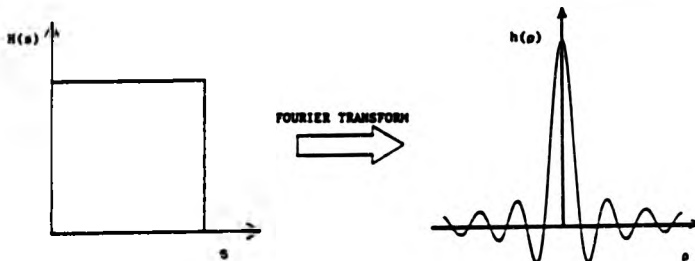


Fig 12. Fourier Transform of the window on the data.

A further problem of this theory is the window (the angular range) of the data. The correlation function needs to be convoluted with the transform of the window function (fig 12). This increases the noise on the data and reduces the resolution of the system. Table 4 gives some of the values of fitted theoretical values for

different windows the largest angular value was always
105°.

TABLE 4: Effect on resolution of system with
changing window on data

Correlation Length (F ₁)	Starting Angle	Fitted Value /μm
0.3	0.0	0.308
0.3	10.0	0.330
0.3	14.0	0.338
0.3	23.0	0.400

As it can be seen, for perfect data the error on the fitted value returned by the fitting programme increases as the window decreases, to give an error of over 30% if the range 23° - 105° is used. Due to the restricted resolution of the data using this method and its inability to fit to data that contains voids this method of analysis has been considered inappropriate.

It was decided to use the theory of Mie to determine the sizes and concentrations of the scatterers present in the epoxy resin system before and whilst it underwent mechanical and electrical stressing.

2.6 CONCLUSIONS

(i) The difference in density between inhomogeneity and medium expected to exist in the epoxy system, will cause the light to scatter and give information on the scatterer size and concentration of

defects present.

(ii) Two theories (the statistical and model approaches) giving this information have been investigated. The restriction on the angular range of the data severely limits the resolution of scatterer size obtained from the transformed data if the statistical theory is applied. Also the theory is inappropriate for the analysis of the scattering from voids present in the epoxy system. Therefore this theory has been rejected for use in the analysis of the results of the light scattering from the epoxy resin.

(iii) The theory of Mie is valid for the analysis of the scattering profiles from both voids and inhomogeneities provided the scatterers can be considered as spheres.

(iv) It has been shown how small differences in size can be determined using the light scattering technique. Therefore it will be able to pick up any small changes occurring to the scatterers as the resin undergoes mechanical and electrical stress.

(v) Mie Theory will be used throughout this thesis in determining the defect and microstructural content of the epoxy resin.

CHAPTER 3.

EXPERIMENTAL APPARATUS AND TECHNIQUE

3.1 INTRODUCTION

Having decided that light scattering was the best technique available to determine scatterer size and concentration, a light scattering system was designed and constructed considering the theories outlined in chapter 2 [69,72]. The light scattering system needed to be able to accurately acquire the scattering intensity at each scattering angle over as large an angular range as possible, whilst at the same time allowing the sample under investigation to be stressed mechanically or electrically to failure. Incorporating a stress apparatus in the system restricted the angular range over which the scattered light from the sample could be measured.

The photometer was designed to optimise the angular range for the scattering cell. A photomultiplier tube was chosen to detect the scattered light as the response of these tubes is linear over a large range of intensities. This is important in this work because of the large change in intensity between the lowest and highest angle measured, and the change

in the observed scattering volume between these angles due to the pinhole geometry. The scattering intensity in the horizontal plane was detected by the system.

The apparatus used needed to be tested and calibrated before it could be employed as a scattering photometer capable of providing data that would give both scatterer size and concentration on analysis. The angular scattering profiles from pure liquids were used to calibrate the system and ensure that the values for the Rayleigh Ratio calculated from the measured intensity using the calibration constant, agreed with those found by others [62,73-76]. Monodisperse polystyrene latex spheres, of known diameter, were used in very dilute aqueous solutions to test that accurate sizing of scatterer diameter can be obtained from the system, to within an acceptable degree of accuracy, using the fitting routine developed from the Mie formulae.

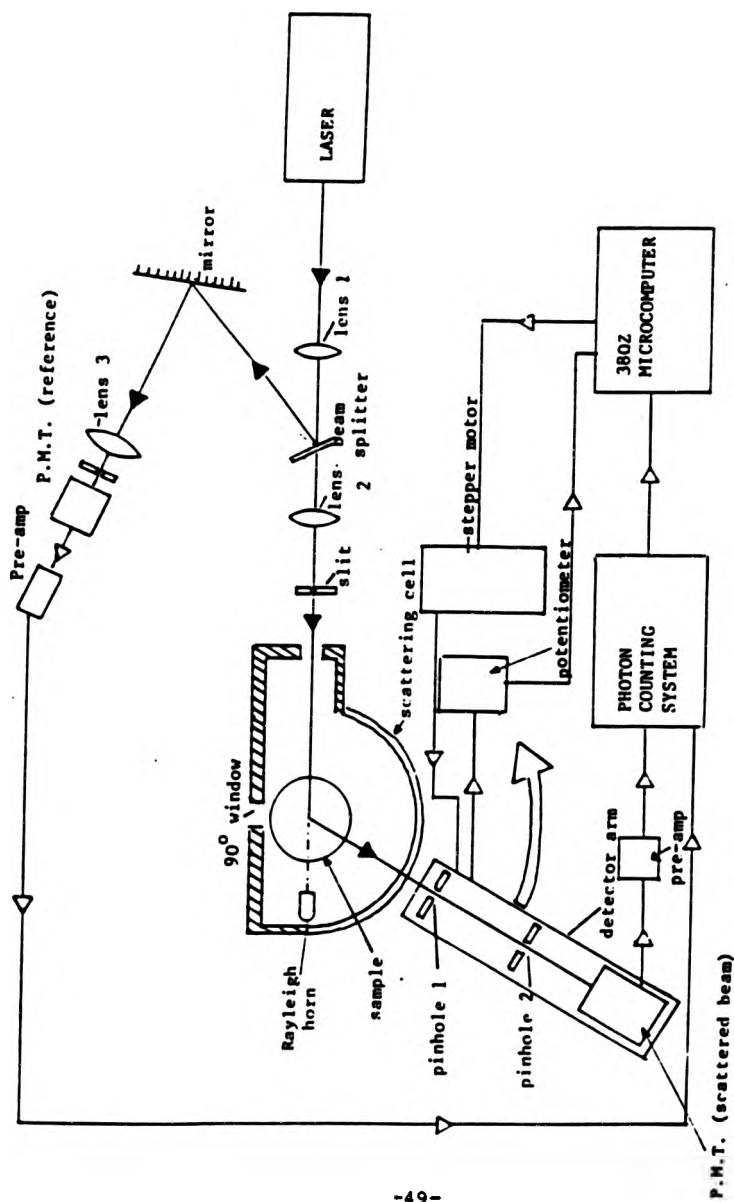


Fig 13 Schematic of scattering system.

3.2 THE LIGHT SCATTERING SYSTEM

A schematic diagram of the system can be seen in Fig.13 The light source was a 10mW helium-neon (HeNe) laser supplied by Scientifica and Cook. The laser produces highly coherent vertically polarised light with a wavelength in air of 632.8 nm. A red laser was chosen as the epoxy resin absorbs in the green-blue region causing fluorescence within the sample which would affect the scattered intensity. Fluorescence at the red wavelength was investigated using a narrow band blocking filter in front of the detection system which absorbed the exciting wavelength. Therefore any fluorescence in the system could be detected. The count was sufficiently low (i.e. at noise level) for the fluorescence intensity to be negligible.

The laser produces a beam of light with a Gaussian profile as described later. The beam was focused down by a system of two lenses, Fig.14, in order to sample as small a scattering volume as possible and to ensure that the beam is as parallel as is possible across the total scattering volume (see Fig 14).

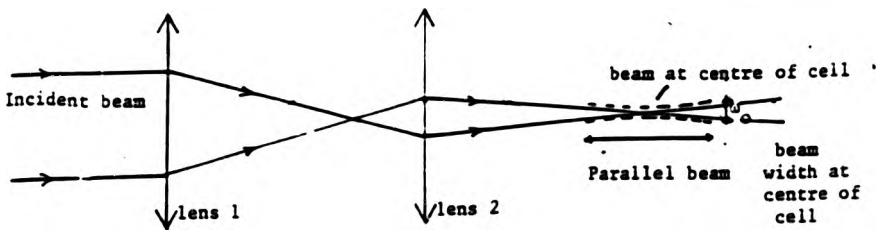


Fig 4. Focussing down of beam.

The value of the diameter of the beam at the centre of the cell was measured using a photodiode (with a spacial resolution less than 10% of the beam diameter) to map out the beam profile after the two lens system. This was fitted to a Gaussian distribution and the half width of the Gaussian profile obtained to give the beam width (Fig.15) of 0.16mm. However when the sample was placed in the beam the diameter was increased to 0.5mm, due to the scattered light and differential refractive index causing a defocussing of the beam.

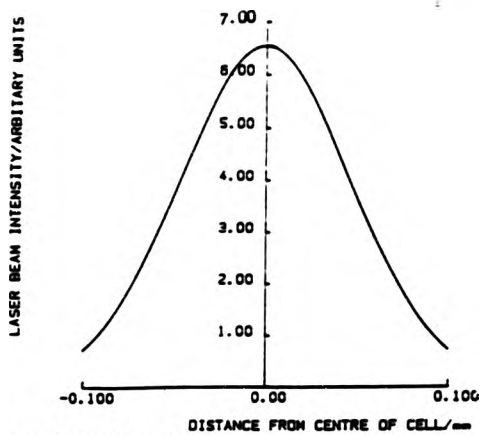


Fig. 15. Profile of laser beam at the centre of the cell.

As shown in Fig.13 a beam splitter was placed in the incident beam before the light enters the sample. This reflects a small amount of the light onto a third lens which is focused onto the entry pinhole of a second photomultiplier tube. This acts as a reference monitoring the incident beam intensity simultaneously with the scattered intensity, so any variation in input intensity can be corrected by simply dividing each count by the reference beam count.

The detection system was designed so that only the

light scattered from a well defined scattering volume enters the detector. The light received at each angular position is collected from as small a solid angle as possible, whilst allowing light of sufficient intensity to be detected for minimum error on calculating the intensity.

The detection system consists of the two pinholes (shown in Fig 16.); a mirror, an iris aperture and a photomultiplier tube.

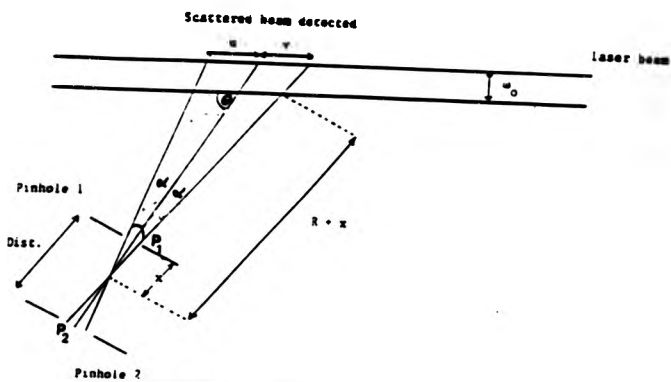


Fig 16. Detection system geometry.

The two pinholes are a fixed distance apart but the pinhole diameters are changeable. The size of the pinholes determines the scattering volume observed as the following equations describe. w is the beam width in the resin sample.

θ is the angle at which data is being collected; u and v and w will determine the scattering volume detected by the system. u and v can be calculated from R once x is known. x can be calculated (see Fig 16.) where x is

$$x = \frac{P_1 \cdot x \text{ Dist}}{P_1 + P_2} \quad (50)$$

The sine rule can be used to find u and v as given below;

$$u = \frac{R \sin(\alpha)}{\sin(180-\theta-\alpha)} \quad \text{and} \quad v = \frac{R \sin(\alpha)}{\sin(\theta-\alpha)} \quad (51)$$

As the scattering angle increases, the scattering volume decreases by a factor of $1/\sin\theta$. This is the correction for angular scattering volume used on the data.

Table 5 gives the angular spread of the data for the pinhole sizes used with the epoxy resins (see Chapter 3).

TABLE 5 : Angular spread (2α) of data for different pinholes

Pinhole 1 /mm	Pinhole 2 /mm	2α
0.6	0.6	0.11 ^o
0.6	1.0	0.15 ^o
0.6	1.5	0.20 ^o
0.6	3.0	0.34 ^o

Table 6 shows how the scattering volume changes with angle for pinholes of sizes both 0.6 mm in diameter. These were the sizes mainly used in the experimental work.

TABLE 6: Variation of scattering volume with angle

ANGLE	SCATTERING VOLUME /mm ³
10	1.490
19	0.795
28	0.552
37	0.431
46	0.360
55	0.316
64	0.288
73	0.277
82	0.261
91	0.259
100	0.263

The signals from the photomultiplier tubes were both amplified 100x each by a pre-amp and then fed into a

5C1 photon-counting system which controls the time taken for each count. At each angle, twenty one-second counts were recorded and the mean taken. A count was taken every 1.5°. The photon counter was interfaced with a Research Machines 380Z microcomputer via a parallel interface board which enables data to be transferred from the photon counter to the microcomputer at the fastest possible rate. The data was stored on floppy disc, so that it can later be transferred to a VAX 750 mainframe computer for fast analysis.

The 380Z computer was also linked to a driver which controlled the stepper motor that turned the detector arm to the next angle at which the data is to be acquired, so the entire system for data collection was fully automated.

The scattering cell into which the samples were placed was made of stainless steel with a semi-circular polished pyrex window through which the scattered light is detected, Fig 17. It was made of stainless steel to ensure that none of the index matching fluids attacked the cell as these contain reactive bromide ions. The full theoretical data range would be 180° before the scattering profile repeated itself. The range of the scattering system is smaller due to the position of the pillars for the stress apparatus. These were placed to optimise the

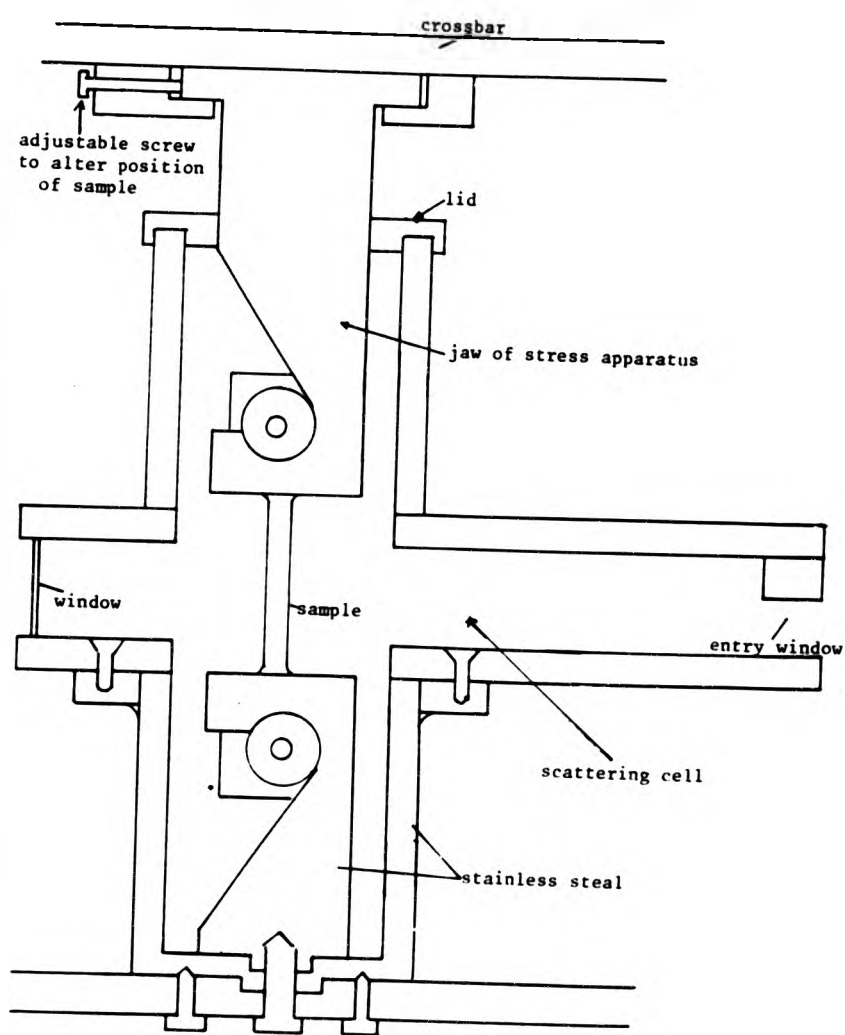


Fig 16. Cross section of scattering cell.

range from 10° to 105° . Below 10° spurious scattering from dust and the incident beam will mask the scattering from the sample. The cell also contained a 90° window at the back of the cell to enable the monitoring of the scattering volume for light emission such as when an electrical discharge occurs. This is important when the sample is electrically stressed as light emission within the sample could occur, artificially increasing the scattered intensity.

The cell was constructed with a removable upper jaw and a permanent lower jaw Fig. 17. This was designed in such a way that modifications could be made for work other than mechanical stressing. These were to

- (i) enable samples to be electrically stressed,
- (ii) enable a cylindrical scattering cell to be included so that scattering from liquids could be analysed.

The stress apparatus, Fig.18, was designed so the sample could easily be attached to the jaw, with no slippage or points where a high build-up of stress could occur and would give a constant and stable stress. For this reason a double beam cantilever system was used. The jaws were made of stainless steel for the same reasons as the scattering cell.

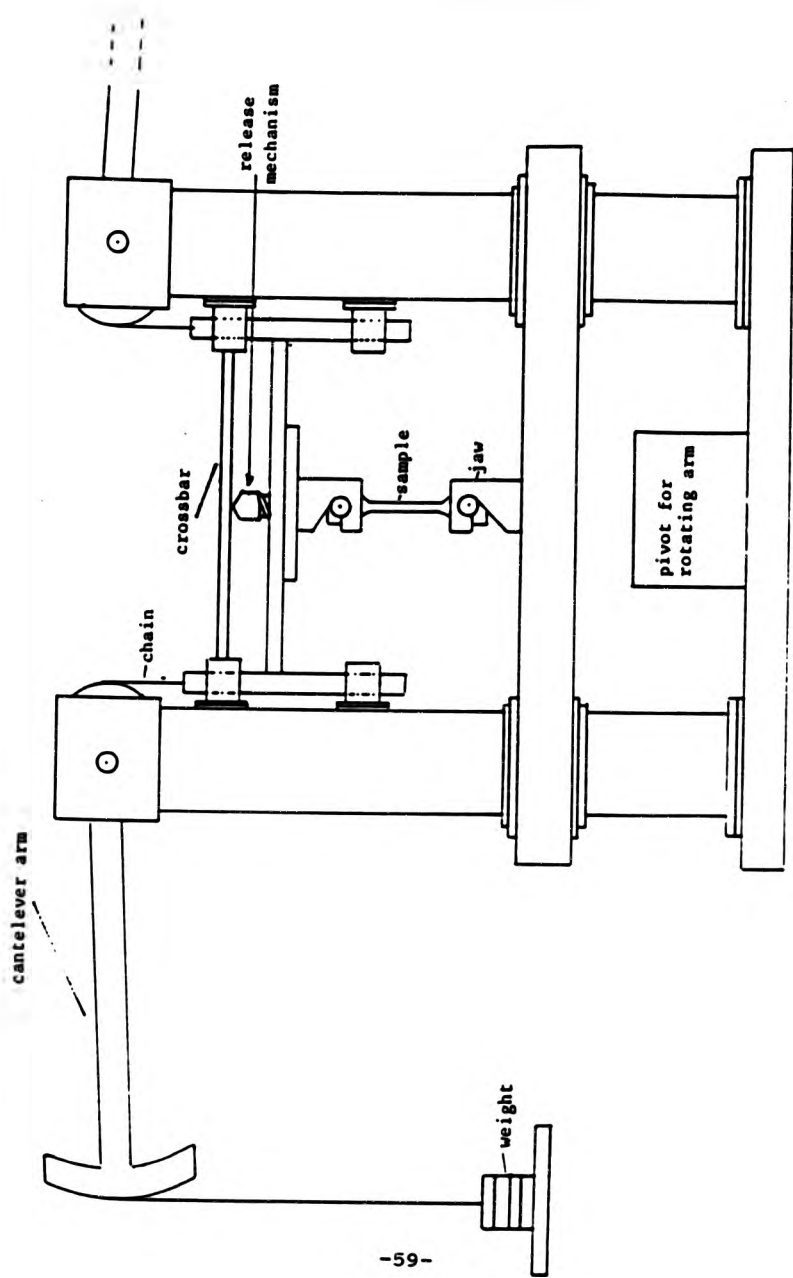


Fig 18. Stress Apparatus

The mechanical lever system had a ratio of 10:1 either side of the pivot in the cantilever arms ensuring sufficient force for failure of the sample in the cell.

3.2.1 Refractive index measurements

The surfaces of the resins had to be highly polished to prevent spurious scattering from any surface features. However, it is practically impossible to achieve a perfectly polished surface so the samples were also immersed in an index matched fluid. A mixture of *o*-bromonaphthalene and decane was used for the matching fluid. Known proportions of each would produce a liquid of the same refractive index as the sample. This was usually matched by eye using the laser beam and determining that the entry and exit surfaces could not be observed. An Abbe refractometer was also used to find the refractive index of the mixture in red light to allow a large enough amount of the mixture to be made to fill the entire scattering cell.

The index matched fluid was filtered using two 0.4 μm Millipore filters in a syringe which allows the liquid to be filtered into the scattering cell. 0.4 μm filters were used as most dust will be much larger than this value and it enables rapid filtering of the matching

fluid. Any particles smaller than this in the matching fluid will have little effect on the scattered intensity. Previous work showed that these liquids had no detrimental affect on the resin.

A Rayleigh horn was placed in the exit beam and acted as a light stop to the beam so that the straight through beam did not effect the low angle scattering intensities or cause serious damage to the photomultiplier tube.

A semicircle of blackened metal was made and placed between the PTFE ring and the stainless steel cell at the back of the sample to prevent any reflections from the back of the cell from entering the detection system. This also allowed the 90° window to be used to monitor any discharge.

3.2.2 Electrical stressing in-situ

The modifications to the system for electrically stressing the sample are as follows; the top jaw was removed and an earth plate placed over the lower jaw (Fig.19), the stress apparatus was used to clamp the sample in position using the cross bar (Fig.18). The sample was aligned by eye using the 90° window, ensuring that the pintip was in the centre of the cell and ~ 0.5 mm above the beam. Details of the a.c. and d.c. circuits used are given in chapter 6.

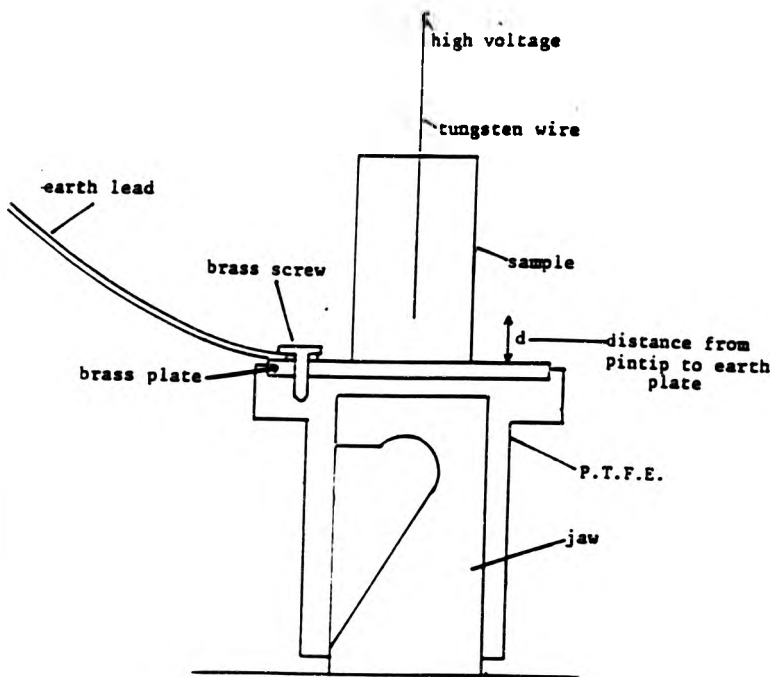
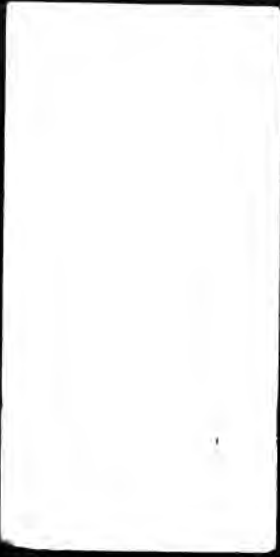


Fig 19. Setup for electrical stressing.

3.3.1 Alignment of the System

To ensure that the scattering detected by the system is from the centre of the sample the whole system needed to be aligned. This was done by first removing the lenses, beam splitter, horn and back mirror of the detecting system. A brass piece was made which could be clamped between the jaws. This had a pinhole drilled through the centre at the same height as the



back pinhole of the detection system enabling the beam to be aligned with the centre of the cell at the correct height for the scattering system. The laser was fitted onto an optical bench and had horizontal and vertical translations to enable the beam to be aligned. For the alignment the detecting system was clamped at 0° .

The beam was considered aligned when the maximum light could be detected. The lenses, beam splitter and front pinhole were then replaced and adjusted to still allow the maximum light through the back pinhole, the beam still passing through the centre of the brass piece.

The reference beam was reflected by a mirror onto a lens (Fig. 13) which was adjusted to focus the beam onto a pinhole in front of a second photomultiplier, the counts for both P.M.T.s were taken simultaneously.

3.3.2. CALIBRATION OF THE SYSTEM.

Once the system was ready for data acquisition it needed to be tested to ensure that reliable data could be obtained and calibrated so that the scattered intensity could be used to determine scatterer concentration. Use of well documented liquids was the obvious choice for two reasons.

(1) They are Rayleigh scatterers which should produce a horizontal angular profile when corrected for

scattering volume, so any spurious scattering at any angle could be detected immediately from simple intensity plots.

(ii) Many authors have determined the Rayleigh Ratio of some common liquids [73-74,76] making them ideal for the calibration of the system.

The three liquids used were carbon tetrachloride, toluene and n-hexadecane. These were filtered into high optical quality scattering cells through 0.025 μm pore size Millipore filters ensuring that very little dust enters the cells to cause spurious scattering.

The scattering cell was adapted to fit the liquid sample scattering cell by using a P.T.F.E. collar which fitted over the lower jaw and had a hole drilled in the centre into which the scattering cell fitted (Fig.20). P.T.F.E. was used as this will not react with the immersion fluid or introduce dust in the scattering cell.

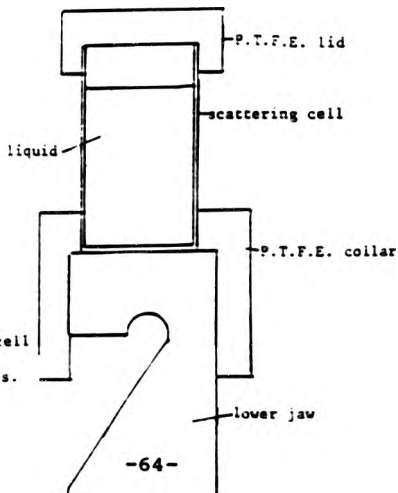


Fig 20. Adaptation of cell to use scattering cells.

Five scattering profiles were averaged and used to obtain the calibration constant. The calibration constant of the cell was obtained using the literature value of the 90° Rayleigh Ratio [43-46] and the 90° scattering intensity from the sample using equation (52).

$$R_{90} = K_{\text{cell}} \times (A_{90}/B_{90}) \quad (52)$$

where

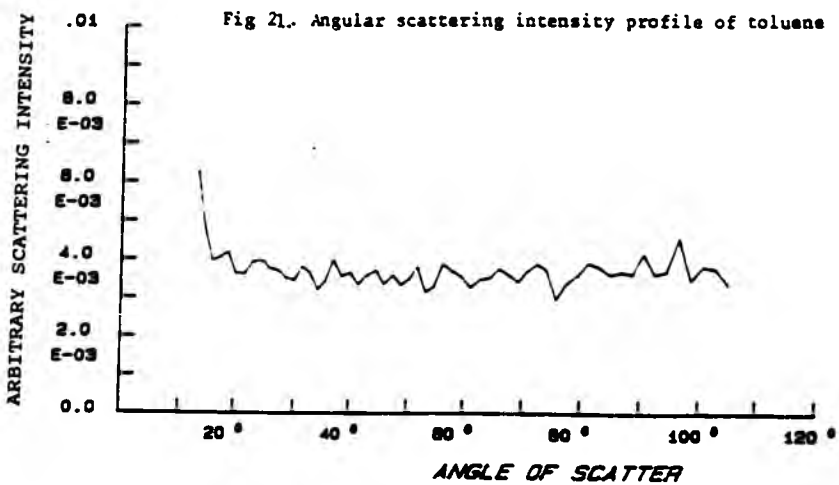
- R_{90} = literature value of R_{90}
- K_{cell} = cell constant
- A_{90} = scattered intensity at 90°
- B_{90} = reference beam count at time A_{90} was measured.

The value of K_{cell} was found using carbon tetrachloride and was then used to calculate the 90° Rayleigh Ratio for toluene and n-hexadecane. These were then compared with the literature values (Table 7).

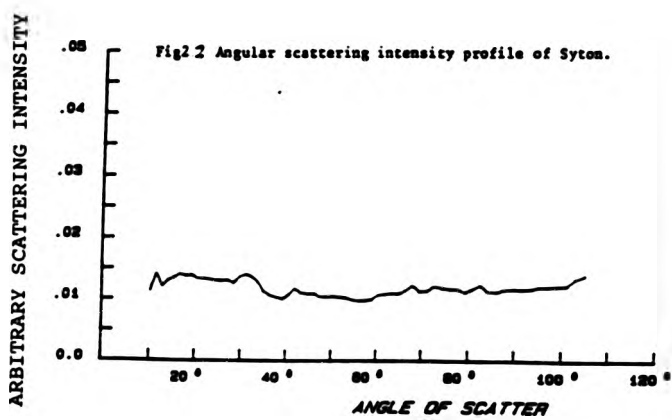
Table 7 Rayleigh Ratios determined from calibration of cell


Liquid	Calc. $R_{90} \cdot 10^6 \text{ cm}^{-1}$	literature $R_{90}/10^6 \text{ cm}^{-1}$	% difference	estimated % error
CCl_4	-	5.221	-	-
$\text{C}_6\text{H}_5\text{OH}$	8.446	8.281	2.0	3.3
n-hexa- decane	4.675	4.166	12.0	10.0

The values obtained were within reasonable agreement of those given by others to within the expected accuracy. There is a higher percentage error for n-hexadecane as the scattering intensity is lower, and any spurious scattering would be more significant. Also, for the other samples, the value of the 90° intensity was an average of five data files whereas only one data file was used for the n-hexadecane 90° scattering value. This was to give an idea of how accurate the data could be from one data file as no average of data could be taken for the epoxy resin under stress.



From the full angular scattering profile (Fig. 21) it can be seen that for scatterers of small intensity, angular values below 25° give spurious scattering probably due to dust in the system which dominates the scattering from the liquids. A stronger Rayleigh scatterer was used to see if the data range could be improved for good scatterers such as the epoxy resin samples. For this Syton X30 was used, supplied by Monsanto, this is a 15% aqueous dispersion of colloidal silica -25 nm in diameter. A very weak aqueous solution was prepared using filtered de-mineralised water. The angular profile (Fig. 22) shows that for larger scattered intensities useful data can be obtained over the full 10°-105° range.

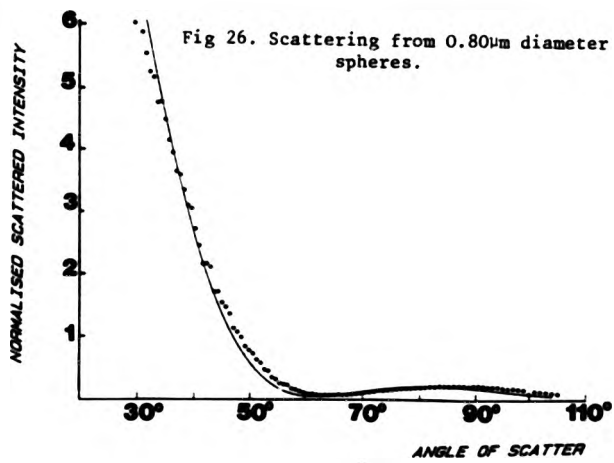
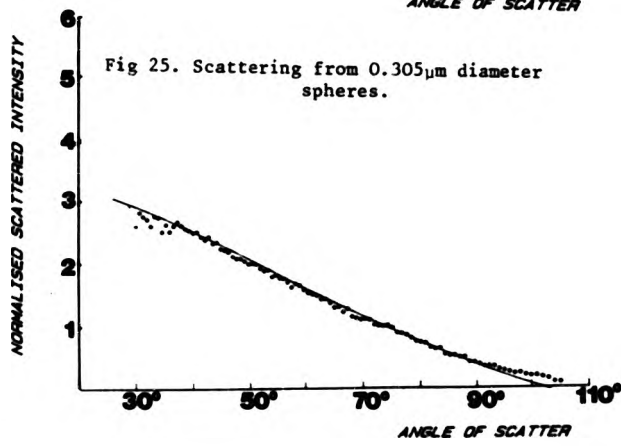
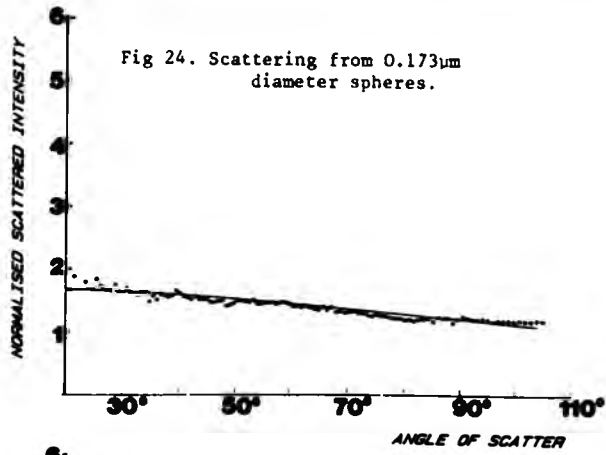


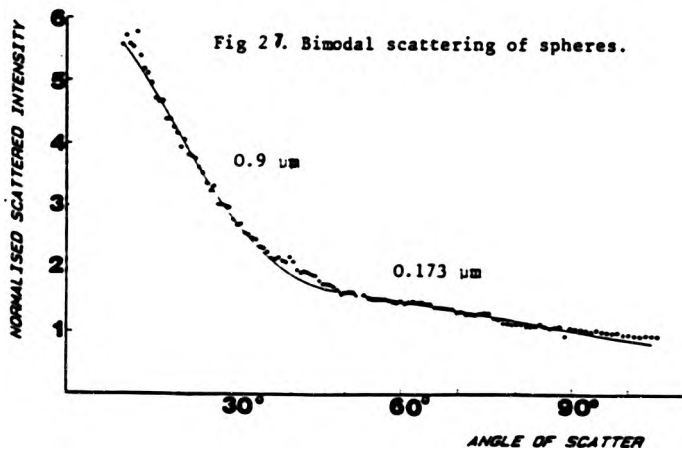
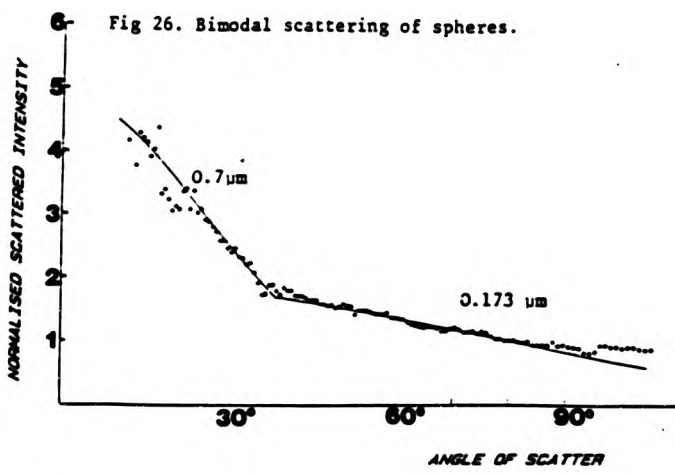


Dilute aqueous solutions of polystyrene latex spheres of known diameter were used to further test the system for accurate determination of particle size. De-ionised water was used with a buffer of pH6 added to prevent coagulation of the spheres. The buffer solution was filtered repeatedly through two Millipore filters of pore sizes $0.05\mu\text{m}$ and $0.025\mu\text{m}$ to ensure the water was completely dust free. The spheres were supplied by Sigma Chemicals at a concentration of 10% in solution. Accurately known volumes were added to 250 cm^3 of the filtered buffer solution using a transferpettor. These were of very low concentration to ensure no multiple scattering occurs. All values of diameter were quoted as accurate to within 0.5% by the manufacturers.

Figs. 23-25 show the fits of the data to Mie Theory for the known sizes.

Although the correct ionicity and pH of the water was maintained, the spheres did coagulate when left in solution over a period of time. These samples show a bimodal type distribution from the nominally $0.173\mu\text{m}$ diameter spheres. When the sample was left overnight (fig 26) it shows scatterers of $0.7\mu\text{m}$ diameter dominating the lower angle scattering, this is 4x the original diameter. The scatterers became larger, reaching $0.9\mu\text{m}$ in size (5x the original diameter) after the sample had been left for three days Fig. 27.





The data was fitted using the Mie formulae [55,56,64,68] fitting routine described in Chapter 2. The results are given in Table 8.

TABLE 8 : Sum of squares on the fit to Mie theory of the data

nominal diam./ μm	fitted Mie diam./ μm	sum of squares for Mie
0.173	0.192	0.0429
0.305	0.304	0.0086
0.800	0.819	0.0190

It can be seen that the scattering system gives valid angular scattering intensities and Mie theory will be able to fit accurately to data obtained from the light scattering system, over a wide range of scatterer size. Sizes used to test the system were in the range $0.17\mu\text{m}$ to $0.8\mu\text{m}$, and it is expected that the size of scatterers within the epoxy resin will fall in this range.

3.4 SUMMARY

This chapter has described the light scattering system used throughout the work. It includes a mechanical stress apparatus with a removable upper jaw enabling scattering measurements to be taken on

- (i) liquids
- (ii) unstressed resin
- (iii) mechanically stressed resin
- (iv) electrically stressed resin.

3.5 CONCLUSIONS

Work on the calibration of the system has shown.

- (i) Accurate data over the angular range 25° to 105° can be obtained for low intensity scatterers. This can be improved to 10° to 105° for good scatterers
- (ii) Accurate size parameters can be obtained.
- (iii) From the data for coagulated spheres it has been seen that information on bimodal systems can be found and both scatterer sizes calculated.

CHAPTER 4

PREPARATION OF RESIN SAMPLES FOR LIGHT SCATTERING

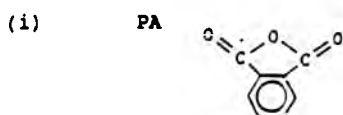
4.1 Introduction

In general use the epoxy resin prepolymer and curing reagent will not be mixed in perfect conditions; air and impurities will be incorporated in the fully cured network which may produce extrinsic defects such as voids and inclusions in the matrix. This work attempts to establish if intrinsic network defects play a part in the failure of the sample, so any extrinsic defects are undesirable. Also from the light scattering point of view, extrinsic defects will scatter the light more and therefore mask any network inhomogeneity so it is important to eliminate air and impurities from the resin and hardener. Therefore a technique of filtration and de-gassing has been developed and used for the preparation of samples for mechanical and electrical stressing.

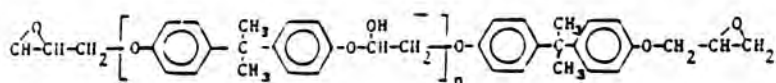
This Chapter describes the epoxy resin system used in this work, the chemical formulae of the two reagents and the crosslinking reactions, how inhomogeneities might occur in the matrix and the sample preparation for light scattering.

4.2 The Epoxy Resin System

The resin and hardener system used is the phthalic anhydride (PA) cured diglycidyl ether of bisphenol A (DGEBA) Ciba Geigy CT200-HT901 commercial system. The chemical structure and crosslinking reactions will now be described.



(ii) DGEBA



The DGEBA oligomers have a low degree of side branching [78] and are hindered and rod like [79-80]. 'n' is a repeat unit and can have a value of up to 12 [20] or more [81] the system under investigation had an average value of $\langle n \rangle$ of 1.7 [19-20] with comparable $n = 0$ to 4 fractions [18]. Two gel permeation chromatographs were taken of the DGEBA prepolymer, the results of which are given in Table 9.

TABLE 9: Fraction of oligomers present in CT200 system used

n-oligomer	g.p.c. fract. area	mass frac. P(%)	epox equiv.	hydrox equiv.
0	0.186	19.68	1.152	0
0, glycol.	0.014	1.55	0.087	0.087
0, chloro-hydrodrin	0.014	1.63	0.087	0.043
1	0.230	22.24	0.847	0.036
1, glycol.	0.019	1.89	0.059	0.088
1, chloro-hydrodrin	0.019	1.94	0.059	0.059
2	0.208	19.51	0.430	0.429
3	0.148	13.66	0.229	0.343
4	0.115	10.51	0.142	0.168
5+	0.082	7.46	0.105	0.119
Other oligomers				

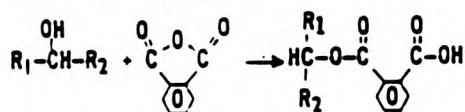
The different end groups originate from the chemical preparation of the DGEBA.

For $n > 0$ oligomers there are at least two types of reaction sites; those of the hydroxyl group and the epoxide group. The hydroxyl groups form the crosslinks and the epoxide groups endlinks. Therefore an $n=0$ oligomer will not form crosslinks. So it can be seen how the polydispersity of the system plays an important part in the network formed, lower molecular weight fractions will give a less densely crosslinked matrix as these oligomers will only be able to produce endlinks.

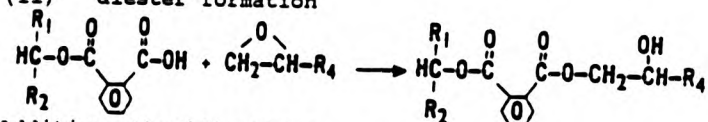
The following crosslinking reactions have been shown to occur when the anhydride and resin are mixed [10,82-88].

Addition esterification:-

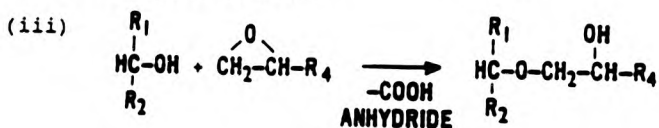
(i) monoester formation



(ii) diester formation



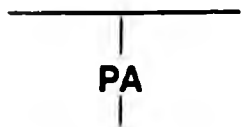
Addition etherification:-



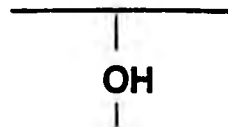
Under normal conditions condensation esterification is minimal [10].

Reaction (i) acts as the initiating step for reaction (ii). It is important to note that in both (ii) and (iii) the free hydroxyl group concentration is conserved to allow for further crosslinking reactions to take place. Reactions (ii) and (iii) are responsible for the connectiveness of the resin [10]. Fig 28a and b give examples of the full network structures of the diester and ether crosslinks. The ether crosslink sequential lengths are shorter than the aromatic ester links. However there will a sequential length distribution as a result of the epoxide oligomer

distribution and incomplete reaction.



(a) ester crosslink.



(b) ether crosslink.

In an ideal case all reactions will go to completion and an infinite network will result extending to the macroscopic dimensions of the sample [89].

All the outlined reactions are in direct competition with each other. A kinetic study of the system [19-20] has shown that the reaction is inhomogeneous and initially addition esterification dominates the crosslinking reactions during the early stages of reaction then addition etherification becomes more effective during the later stages of reaction. This means the initially formed matrix will be chemically different to the one formed later. Chemical differences however, may bring about only very small physical density differences between areas of different chemical crosslinking as only the chemical nature of the bonding is different [10]. The density differences will in this case depend on the chemical positioning of the oxygen atoms and phenyl groups.

4.3 Possible Network Defects

As already discussed, an ideal network will be infinite and extend to the macroscopic dimensions of the sample and as such will meet its ultimate tensile strength. Epoxy resins fail long before the theoretical strength of the breaking of the carbon-carbon bonds [90]. Therefore, epoxy resins do not represent ideal systems. The main causes of network defects as listed by Dusek and Prins [91] are listed below.

(i) 'Network inhomogeneity from pre-existing order'.

In the system under investigation it is possible for hydrogen bonded aggregates to exist in the prepolymer prior to mixing. This has been suggested for other polymers [92]. Evidence of this has been observed using light scattering [11-12] although differential scanning calorimetry (d.s.c.) measurements have not shown two phases, so a separate and discrete hydrogen bond phase is thought not to exist [18]. These aggregates will have a high concentration of hydroxyl groups and will act as preferential reaction sites for the anhydride (fig 29). This will depend on the history and reaction conditions of the sample [11-12]. The reaction would appear inhomogeneous and colloid like. A study of these reactions [19,20] has found that these reactions are consistent with inhomogeneous colloid

type behaviour that is, $X+Y \rightarrow Y$ where Y is self similar. However due to the complex chemical kinetics of the system the model outlined here may require some modification.

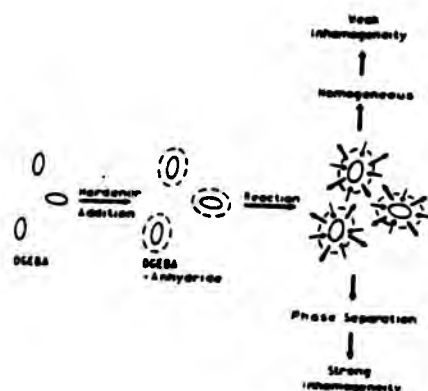


Fig 29. Possible reaction procedures at aggregate interface.

(ii) 'Network Defects'

These arise from:-

(a) unreacted functional groups that become sterically hindered as the system reaches gel point and will remain unreacted in the fully cured system Fig 30a.

(b) intra-molecular reactions, where functional groups within the same molecule react together preventing them from forming crosslinks Fig 30b.

One study [22] has shown that 1 in 16 bonds are loop producers in a stoichiometric system, this

number increases as the system is diluted, indicating the importance of the initial ratio of resin to hardener to the type of defected network formed.

(c) intermolecular entanglements are also likely again disrupting the network at these points
Fig 30c

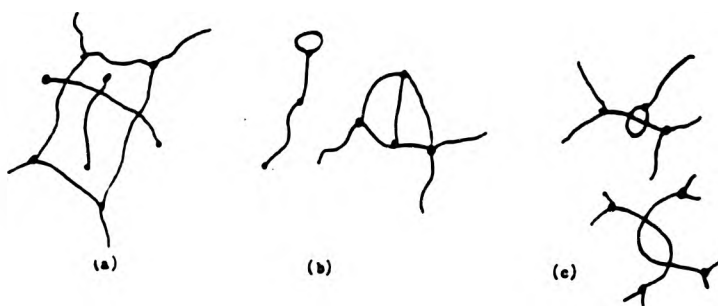


Fig 30. Network Defects

(iii) 'Inhomogeneous Network Formation'

Polydispersity of the prepolymer gives a different spatial arrangement of crosslinks due to the differences in lengths between -OH groups for different oligomers. A broad distribution could produce a homogeneous network but a spatial distribution as a result of the presence of $n=0$ oligomers may occur resulting in an inhomogeneous network. In the system under consideration the crosslinking reactions are exothermic which means localised heating can occur at the reaction points causing the reaction to proceed at a faster rate at those points leading to the formation

of microgels [10]. Uneven curing will also result from incomplete mixing of hardener and resin [79,80]. Therefore, it is important to thoroughly mix the two reactants to ensure any structure observed is not just an artifact of the mixing technique.

(iv) 'Phase Separation'

If the crosslinking reaction proceeds in solution then this has to occur at localised points. This should then proceed until all the individual regions connect. If however some critical value of crosslink density of the local regions is achieved then phase separation can occur with low molecular weight material being ejected as a solvent phase. The resulting network could then be highly inhomogeneous fig 31.

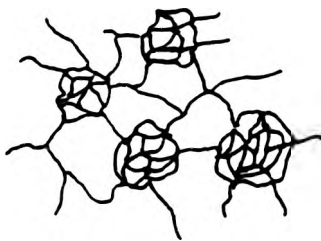


Fig 31. Network Resulting From Phase Separation.

In conclusion to this section it can be seen that a large number of factors can be involved in producing a defected matrix. Some can be avoided, such as incomplete distribution of the reactants by improving the mixing technique. The next section describes the technique used in preparing the epoxy resin samples,

this has been perfected to ensure that any defect present in the matrix is inherent to the epoxy system and not a result of the sample preparation. This also provides us with a well defined sample free of extrinsic defects.

4.4 PREPARATION OF SAMPLES

4.4.1 Ultra Clean Samples

Stoichiometric mixtures 100:30 parts by weight resin to hardener were used. This was determined from the reaction chemistry ensuring that all the functional groups have the chance of reacting. This includes an efficiency factor 0.8. In an ideal case the sample will be fully crosslinked.

A known amount of the crystalline anhydride was weighed and filtered at 140 °C, where the anhydride is a free flowing liquid, into the top compartment of a mixing vessel (Fig.32) using a two phase Millipore filtration system (Fig.33) under dry nitrogen. Millipore 0.2 µm type FG fluoropore filters were used. These were soaked in xylene for 4 hours for the easy removal of the polypropylene mesh support for the P.T.F.E. filters, as the anhydride attacks the polypropylene causing the mesh to break up and

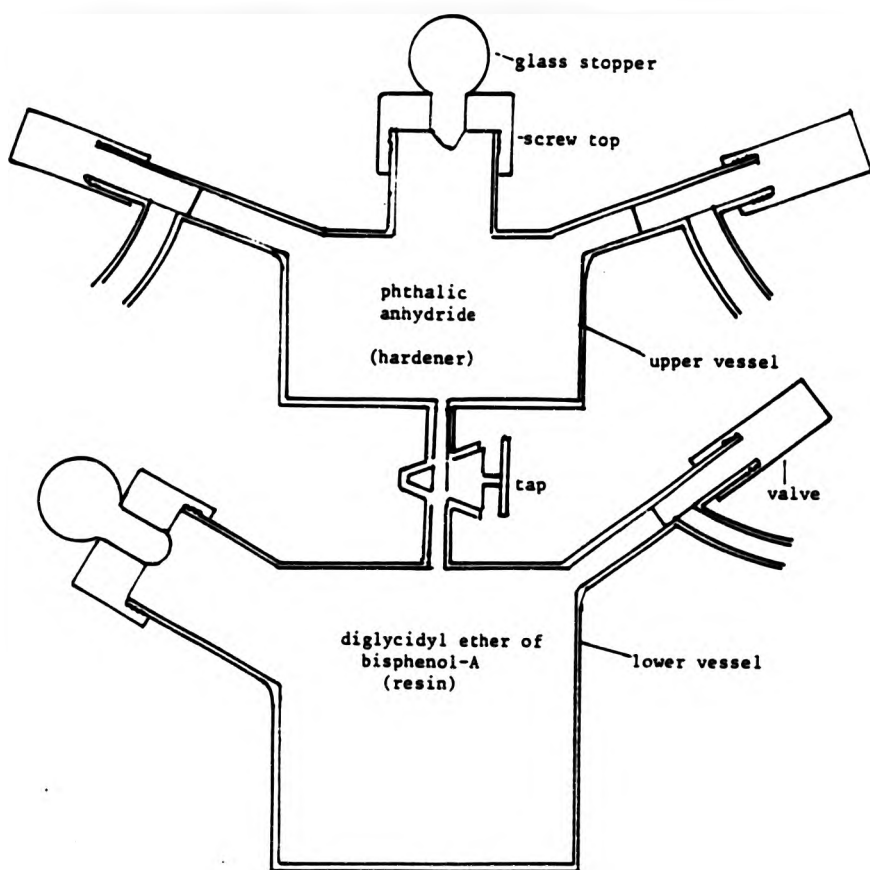
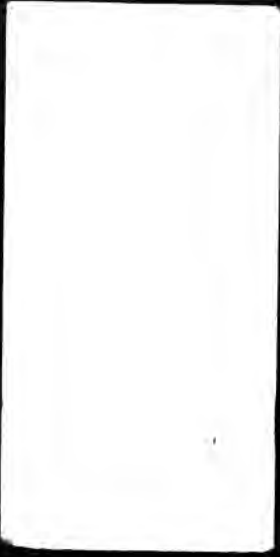


Fig 32. Mixing Vessel for the epoxy resin



contaminate the filtered anhydride. As the anhydride is highly volatile, the reaction vessel was weighed before and after the filtration to determine the actual mass of anhydride filtered. As the anhydride is extremely hygroscopic it was filtered onto a bed of dry nitrogen.

The stoichiometric amount of resin for the mass of anhydride was weighed and dissolved in butanone, this was then filtered at room temperature into the bottom of the mixing vessel using a three phase filtration system (Fig.34.). The same 0.2 μm type filters were used with the supporting mesh removed as the butanone would dissolve the polypropylene again contaminating the resin. Once the solution was filtered it was placed in a laser beam to ensure that no dust was present. Dust would show up as bright speckles in the beam. The temperature of the DGEBA-butanone solution was then raised to 80^o C using a magnetic hot plate and stirrer, the butanone was then evaporated off using a rotary pump and a liquid nitrogen cold trap to condense the solvent and ensure that no oil from the pump entered the mixing vessel. The resin was then fully degassed at the same temperature still using the rotary pump.

Care was taken not to raise the temperature of the resin above 100^o C as microgelation can occur at temperatures above this value. The anhydride was then

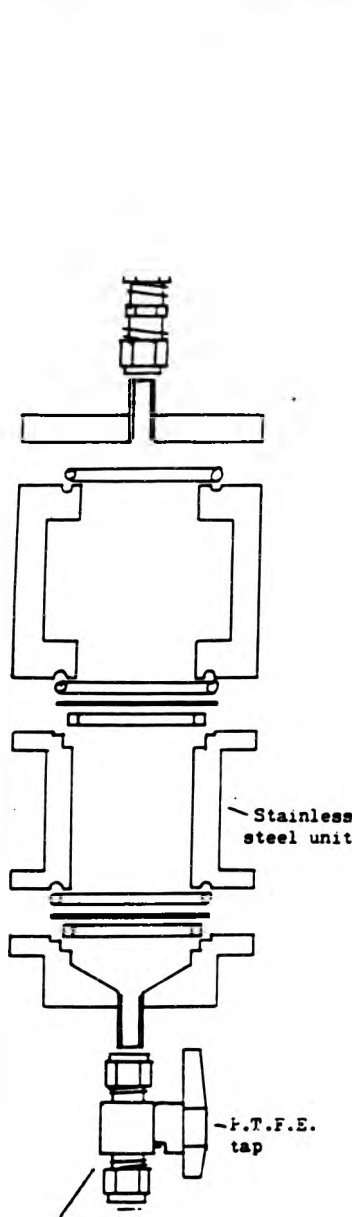


Fig 33 Anhydride filtration unit

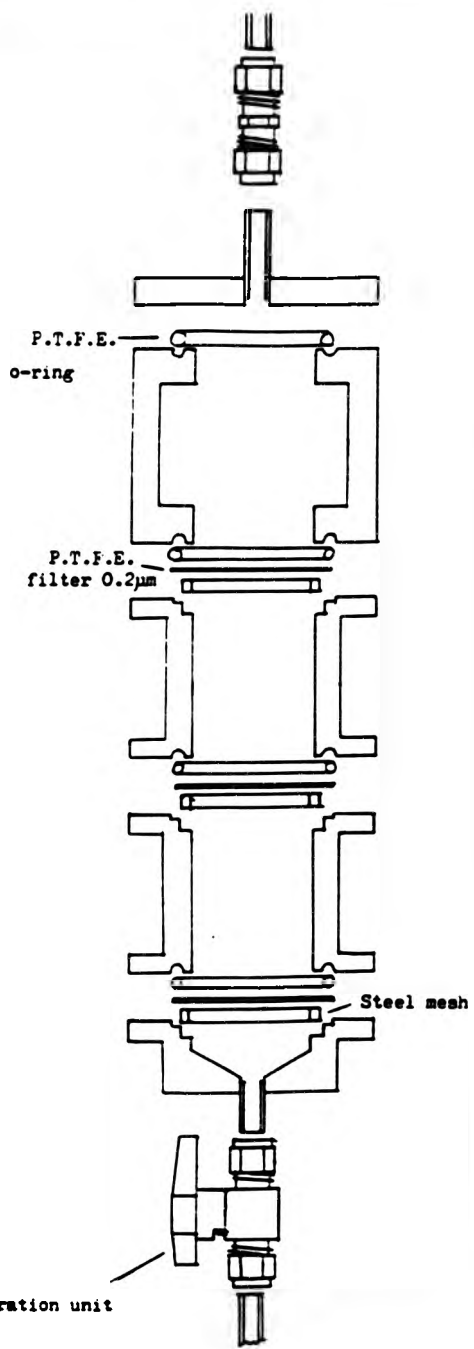


Fig 34 Resin filtration unit

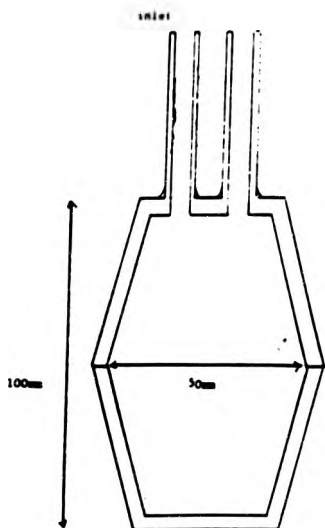


Fig 3 5. Large cylindrical mould cross-section

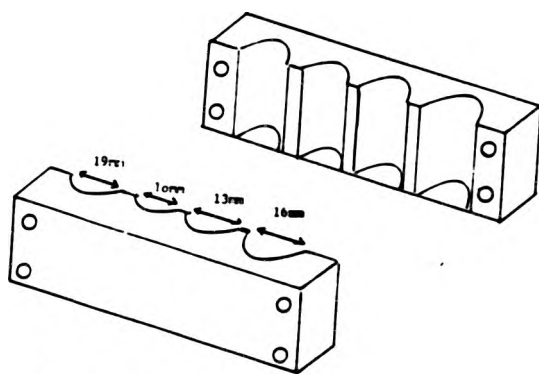


Fig 3 6. Mould for small cylindrical samples

degassed at room temperature; this was to ensure that none of the anhydride was lost as it is extremely volatile when liquid. The reaction vessel was then reweighed and placed in the oven at 140 °C until the anhydride had completely melted. The vessel was then removed from the oven and placed on the magnetic hotplate where the anhydride was added to the DGEBA and thoroughly mixed using a magnetic stirrer.

The anhydride was added to the resin as a liquid to ensure a more even mixture, this is not in accordance with the manufacturer's recommendations [95], but is consistent with other workers [9-12]. Ciba Geigy recommended addition of the anhydride as a solid but there is a possibility of unreacted anhydride remaining in the cured network. The mixture was then fully degassed for 20 minutes then poured into moulds preheated to 125 °C (see Figs.35-36). The samples were then cured for 2 days at 125 °C, allowed to cool to -80 °C taken out of the moulds then replaced in the moulds and further postcured in a vacuum oven at 150 °C for 8 hours to ensure all the curing reactions have gone to completion. A vacuum oven was used to ensure that no oxidation of the resin occurred at the high temperatures. The vacuum oven was then switched off and the resin allowed to cool slowly through the glass transition temperature T_g (100 °C-110 °C). The samples were then taken out of the oven and released from the



moulds.

Samples were prepared for mechanical stress from the large cylindrical mould (Fig. 35). Samples for electrical stressing were prepared in cylindrical flat sided glass bottles 20 mm in diameter with the tungsten tips inserted in the centre of the bottle using a P.T.F.E. bung, (fig. 37). The preparation of the pin tips is described in Chapter 6.

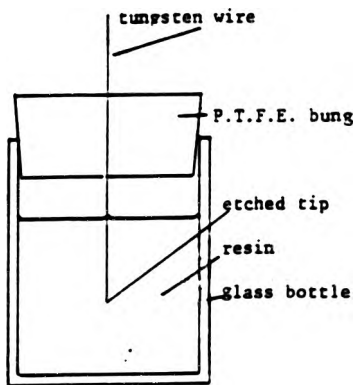


Fig 37. Setup for producing samples for electrical stress

4.4.2 VOIDED SAMPLES

Some samples were prepared with a known volume of gas added to them in an attempt to produce a controlled number of defects in the matrix, and to see if these affected the mechanical properties of the resin. The same procedure of sample preparation was followed

except that after degassing the resin prepolymer, a known volume of carbon dioxide or nitrogen was added, to create a certain percentage volume concentration of gas to resin. The resin-hardener mixture was no longer degassed. Table 10 shows the amount of gas added to the samples and the range of particle sizes found in them. This shows that carbon dioxide is possibly more soluble in the resin than the nitrogen, due to the smaller voids present in the CO sample. The nitrogen behaves in a similar way to air as might be expected.

TABLE 10 : Range of void sizes found in epoxy resins with different added volumes of gas.

Sample	Range particle size/ μm
clean	0.83-0.095
100% N ₂	0.77-0.11
200% N ₂	1.3-0.065
300% N ₂	0.4-0.12
sat. CO ₂	0.57-0.14

The samples were cured and postcured in the same way as before.

4.5 CONCLUSION

A vast range of possible network defects could exist in the epoxy resin system. From the chemistry of the system two types of crosslinking reactions occur, addition esterification and etherification. An analysis of the kinetics of the system [19,20] has shown that initially esterification dominates the crosslinking

reactions then etherification becomes the most dominant reaction.

The reaction is inhomogeneous and colloid like. If this type of reaction behaviour is considered along with the possibility of the presence of hydrogen bonded aggregates in the epoxy resin prepolymer [11-12], then the resulting crosslinked network is likely to be inhomogeneous the inhomogeneity resulting from the hydrogen bonded aggregate.

CHAPTER 5.

MECHANICAL STRESSING OF THE EPOXY RESINS.

5.1 Introduction

Laser light scattering was used to investigate the possibility of microstructure in the PA-DGEBA samples and to see how an inhomogeneous network deformed under uniaxial tensile stress and if it acted to nucleate voids or other flaws. Should voids exist in the matrix light scattering could also be used to monitor their behaviour during deformation. In the case of both types of scatterer, a link between microstructure and macroscopic yield or fracture was sought.

5.2 Stressing of Samples and Results.

5.2.1 Scattering From Unstressed Samples

Scattering envelopes from unstressed epoxy resin samples were obtained using the light scattering system, and analysed to ascertain the type of defects present, their sizes and concentrations.

The light scattering envelopes were analysed using the Mie fitting routine described in Chapter 2. A refractive index variance of 1% was chosen for inhomogeneities. This corresponds to a density variance of 0.5%. Previous work used a density range of 1%-4.3% [9,11] to determine the presence of inhomogeneities and their size. A smaller density

difference was chosen in this case as it was considered that the changes in physical density difference between highly crosslinked areas and less crosslinked areas will be smaller in the fully cured system than the prepolymer. If we consider equation 53 from which the mean square variance $(\overline{\Delta\rho_0})^2$ of thermal density fluctuations can be calculated [11].

$$(\overline{\Delta\rho_0})^2 = k_B T \kappa_T \rho_0^2 / v \quad (53)$$

where k is the Boltzmann's constant,
 κ is the thermal compressibility,
 ρ_0 is the average sample density,
 T is the temperature and
 v is the scatterer volume.

Then if we use the values for a liquid of ρ_0 and κ (see ref 11) then for an inhomogeneity value of diameter 40nm which is the smallest value of diameter obtained in this work. The thermal density fluctuation will be -0.02% far smaller than 0.5%. Therefore the use of the value of 0.5% is valid for inhomogeneities in the system.

As the sample is stressed if one area of crosslink density deforms greater than another, such as a more weakly crosslinked area, the refractive index variance between the two regions will increase. However it is

not expected that the size of scatterer calculated from the Mie analysis will be sensitive to the relatively small change in refractive index with stress. Therefore the same refractive index variance was used throughout the whole analysis of the stressed data.

In principle Mie theory can differentiate the presence of a void or an inhomogeneity by the value of the sum of squares of the residuals (see Chapter 2).

Both types of scatterers were observed to exist within the epoxy resin. Table 11 gives examples of some of the sizes and concentrations typical of these scatterers. It can be seen that there is a very wide range of size and concentration for both types of scatterer showing how inhomogeneous the network is.

TABLE 11 Initial size and vol fraction of inhomogeneities in unstressed samples.

SAMPLE	SIZE OF SCATTERER / μm	$\%$ VOL. FRACTION
INHOMOGENEITY		
7	0.045 \pm 0.005	7.6 \pm 0.011 $\times 10^{-2}$
3	0.079 \pm 0.003	2.3 \pm 0.060 $\times 10^{-2}$
11	0.086 \pm 0.002	9.0 \pm 0.05 $\times 10^{-5}$
8	0.167 \pm 0.06	1.90 \pm 0.07 $\times 10^{-4}$
VOID		
6	0.234 \pm 0.084	0.69 \pm 0.06 $\times 10^{-3}$
9	0.270 \pm 0.051	0.19 \pm 0.02 $\times 10^{-2}$
10	0.495 \pm 0.044	0.73 \pm 0.04 $\times 10^{-3}$



5.2.2 Stress Procedure

The same procedure was followed for the stressing of all samples. Cylindrical dogbone samples with 0.4 cm long gauge length (fig 40) were hand crafted from the initially cylindrical block of resin from the large mould fig 35. the average diameter of the dogbone samples was 3mm; this size was chosen to ensure that failure of the samples could occur within the load capacity of the system as calculated from the Youngs Modulus and fracture stress of the epoxy resin which are $3.3 \times 10^9 \text{ Nm}^{-2}$ [82] and 70 MNm^{-2} reselectively.

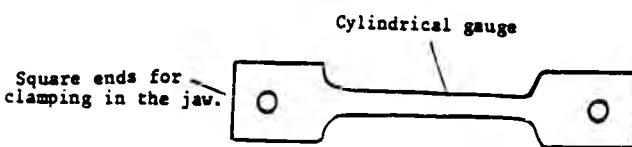


Fig 40. Actual size of dogbone

The gauge length of the samples was highly polished using various grades of emery paper 0 ---> 0000 and No. 2 grade perspex polish supplied by I.C.I.. They were polished to ensure that there were no surface defects which would cause spurious scattering. This also

reduced the number of sites for premature failure such as scratches which would act as stress concentration sites.

The samples were then placed in the jaws of the stress apparatus surrounded by a filtered refractive index matched fluid. The scattering profile was obtained of the samples before undergoing any stress and analysed. The sample was re-positioned in the cell using the adjustments on the top jaw (Fig. 17), until a scattering profile from the specimen was obtained, which contained no spurious scattering at any angle.

For many samples, as the scattering volume observed was relatively small ($\sim 0.2 \text{ mm}^3$ at 90°), it was possible to find scattering volumes that contained only inhomogeneities, as well as others where the scattering was dominated by a small population of microvoids. The deformation of both types of scatterer was investigated. Once the scattering volume for a sample was chosen, the samples were then loaded. One kilogramme weights were hung on both sides of the double cantilever beam (Fig. 18). The samples were loaded 0.6kg at a time up to 1.8kg then left over night at that value and unloaded 0.6kg at a time the next day, down to zero stress and again left over night. The samples were then loaded 0.6kg at a time up to at least 6kg, whilst sample 7 was loaded further and failed on

a reload. The results of this are given in fig 45. The samples underwent a system of loading and reloading to determine if the epoxy deformation behaviour was reversible and if so after which point did it become irreversible, ie where does yield occur?

Three angular scattering envelopes were collected for each different load value. If the samples were left overnight at a certain value, data was taken again at that value the following morning to ascertain if any change had occurred at the same stress over night. Each file contained 64 angular data points. Each intensity value was an average of ten 1s counts over the range of 10^0 - 10^5 , on average it took 30 minutes to collect the data for one file.

5.2.3 Results on Light Scattering of Stressed Samples

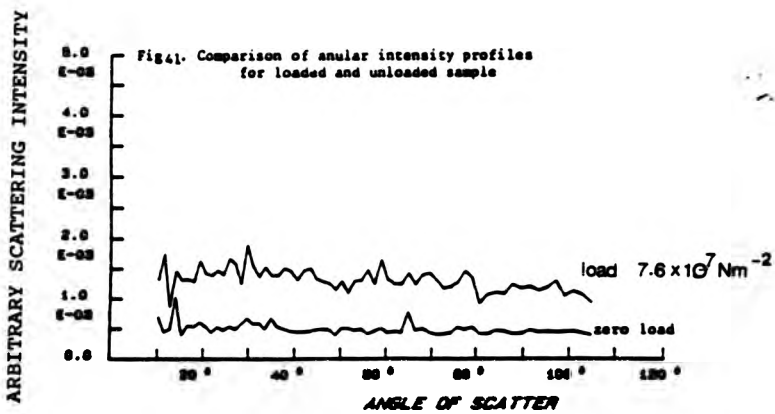
Two definite trends were observed in scatterer behaviour as the sample underwent uniaxial tensile stress. The trend depended on the type of scatterer present.

5.2.4 Scattering Behaviour of Inhomogeneities under Tensile Stress

Fig. 41 shows the sensitivity of the system by the change in angular intensity between load and unload data, indicating that the scatterers at the load value have changed dramatically to the zero value scatterers. This is born out by the analysed results from the data,



Figs 42-44 where scatterer size has increased along with the Rayleigh Ratio whilst the concentration has decreased. It may also be that the nature of the scatterers has changed as will be discussed later.



Figs. 42-51 show the behaviour of scatterer size, concentration and the Rayleigh Ratio typical for a scattering volume containing only inhomogeneities.

Initially scatterer size and concentration increased to a stress value, σ_1 then the size and Rayleigh Ratio decreased gradually towards a point where they reach their initial values at a stress value σ^* . However the concentration continuously increased up to σ^* and beyond this point decreased. The load, unload and reload behaviour shows reversibility up to σ^* . Beyond σ^* the material was irreversible (Fig 45). The character of the scatterers changes around the stress value σ^* . The sum of squares on the fit becomes greater indicating that it is no longer appropriate to fit entirely to inhomogeneities. Also the new trend in the behaviour of concentration and scatterer size follows closely that found for distributions of voids, with scatterer size increasing with stress and concentration decreasing with stress. It is therefore likely that voids have been created at σ^* .

Fig. 42 gives a zero stress value of $0.275\mu\text{m}$ on unload, smaller than the original zero stress value. This suggests that some modifications or relaxation may have occurred during stressing of the network. It is possible that the first set of data was erroneous due to unsettled bubbles and dust in the index matching fluid which settled out of the beam with time. These

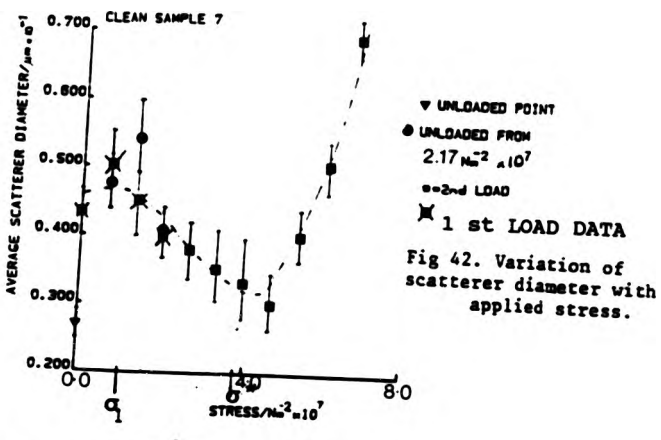


Fig. 42. Variation of scatterer diameter with applied stress.

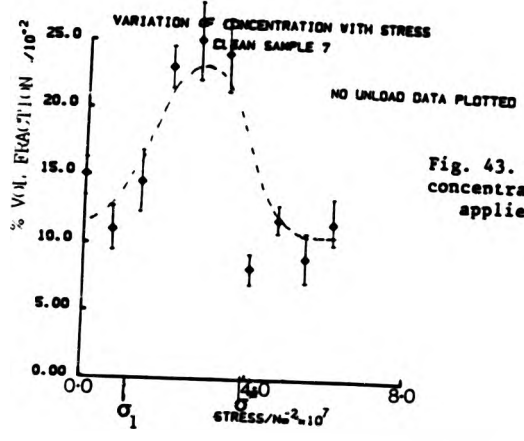


Fig. 43. Variation of concentration with applied stress.

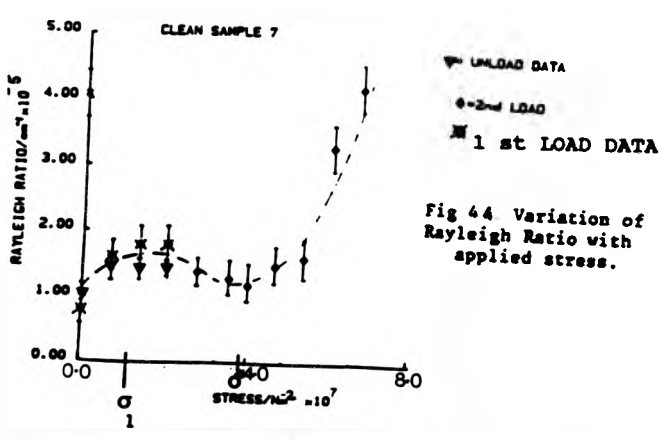
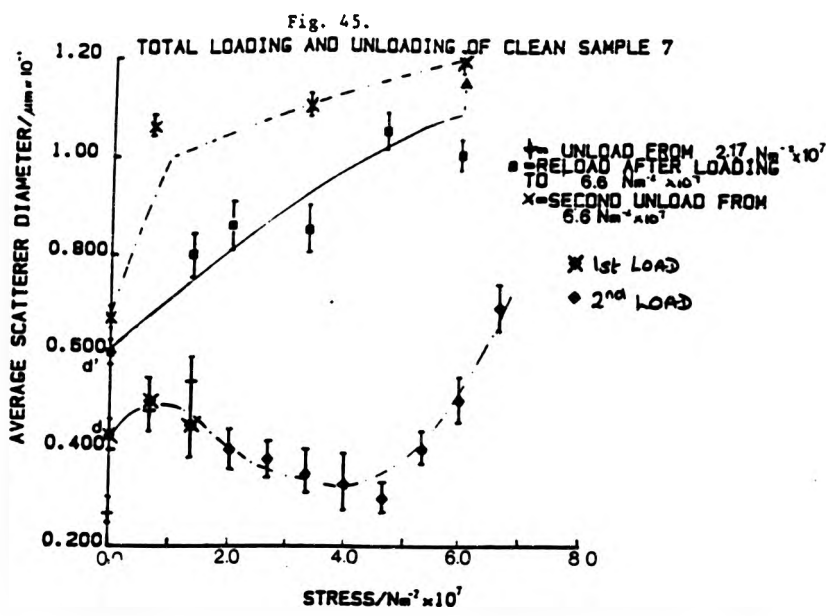


Fig. 44. Variation of Rayleigh Ratio with applied stress.



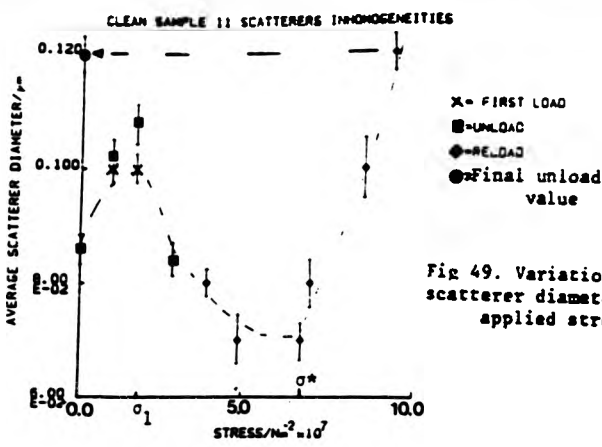


Fig 49. Variation of scatterer diameter with applied stress.

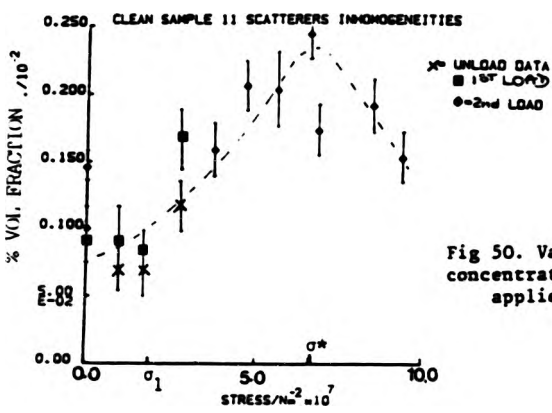


Fig 50. Variation of concentration with applied stress.

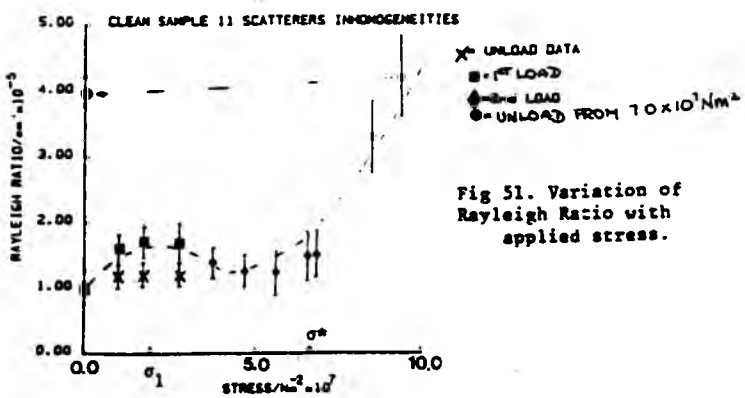


Fig 51. Variation of Rayleigh Ratio with applied stress.

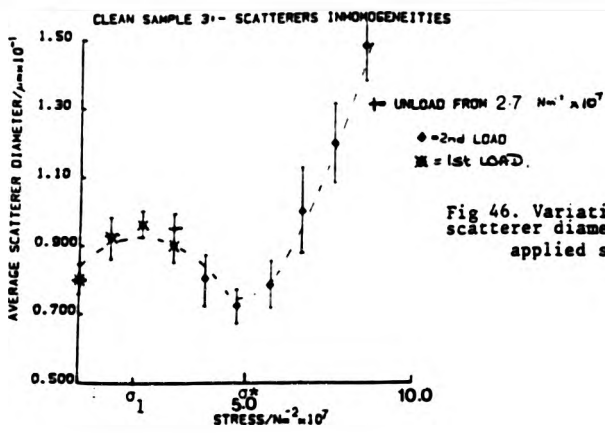


Fig 46. Variation of scatterer diameter with applied stress.

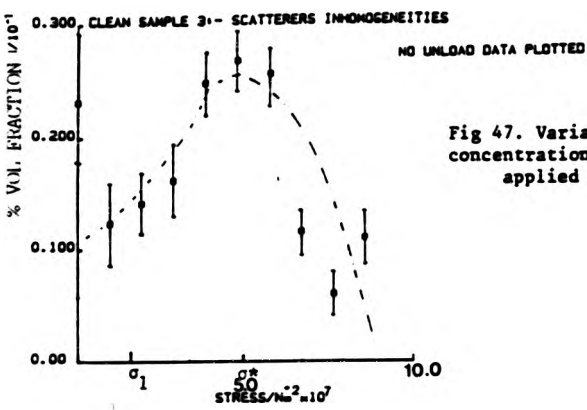


Fig 47. Variation of concentration with applied stress.

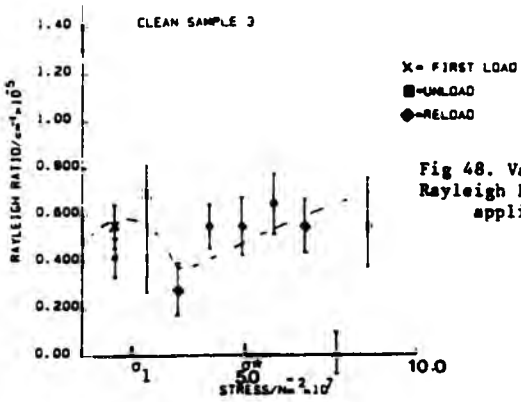


Fig 48. Variation of Rayleigh Ratio with applied stress.

will more greatly influence the low scattering angles and therefore may not be observed by the value of the 90° Rayleigh Ratio being relatively too high. Other samples have not shown this. Fig. 46 shows the zero stress value of scatterer diameter before loading and, on unloading from $2.7 \times 10^7 \text{ Nm}^{-2}$ returned to the same diameter to within the experimental error.

Fig. 45 shows the change of scatterer size on further loading and unloading of the sample. The new zero stress value of scatterer diameter d' is larger than the original zero stress value d indicating that the sample has not returned to its original state, and that the scatterer size increases with increasing load. The loading showed hysteresis with a small decrease in scatterer size as the sample is unloaded until it has returned to zero stress where the size approaches the value of d' . This suggests that with time the sample could return to d' . This sample failed on reloading.

Figs. 46-51 show the same trends for other samples. This substantiates that this is a true material behaviour. All samples gave similar values for σ_1^* and σ^* and are likely to be characteristic material quantities, typically $\sigma_1^* = 2.0 \times 10^7 \text{ Nm}^{-2}$, and $\sigma^* = 5.0 \times 10^7 \text{ Nm}^{-2}$. All samples that have failed, failed beyond the value of stress σ^* or on reload having once gone beyond σ^* .

It was noted that beyond values of stress σ^* the sum of squares on the fitted data increased (see Table 12).

TABLE 12 : Change in sum of squares with stress on data beyond stress $5.0 \times 10^7 \text{ N m}^{-2}$ (σ^*)

Stress /Nm ⁻² x10 ⁷	scatter size /μm	sum of squares on fit
3.96	0.269+/-0.023	287
4.62	0.274+/-0.022	295
5.28	0.312+/-0.017	501
5.61	0.337+/-0.02	831

The sum of squares for fitting to inhomogeneities is usually 40-100. Therefore as the sum of squares on the fit to the data increases with applied stress especially for values beyond σ^* , the scatterers being inhomogeneities becomes less likely. This can only be explained by considering that yield occurs at σ^* and voids are created and grow with applied stress. The value of the sum of squares is reduced to 300 beyond σ^* if the scatterers are treated as microvoids.

Table 13 gives for each different sample the initial value of size, concentration and Rayleigh Ratio and the yield stress observed for some of the clean samples.

Table 13: Initial values of inhomogeneity diameter and yield stress for the clean samples placed under uniaxial tensile stress.

Sample Number	Rayleigh Ratio $\times 10^{-5} \text{cm}^{-1}$	Yield Stress (σ^*) 10^7Nm^{-2}	Initial diam. / μm	Initial % vol fraction
3	0.8+/-0.08	4.62+/-0.3	0.08+/-0.003	.026+/-0.008
7	1.2+/-0.12	3.93+/-0.8	0.043+/-0.005	.0074+/-0.0001
8	0.69+/-0.07	5.11+/-0.7	0.168+/-0.004	.000195+/-0.0000
11	1.0+/-0.12	5.28+/-0.8	0.086+/-0.002	.000095+/-0.0000

5.2.5 Behaviour of Voids under Stress.

For those regions in which a population of microvoids were already present in the scattering volume before the application of stress the following results were obtained.

Figures 52-58 show the variation of size and concentration of microvoids with stress. In Fig. 58, the variation of Rayleigh Ratio is also shown to compare with the data (fig 44) obtained for the scattering from inhomogeneities. These all exhibit an increase in size with stress and the extent of the increase depends on the initial concentration of voids.

Fig 52 and 53 show an increase of size with an initial increase in concentration, followed by a decrease in concentration, indicating preferential void growth towards the end of the stress period. The shape of the curves resembles that of the variation of scatterer

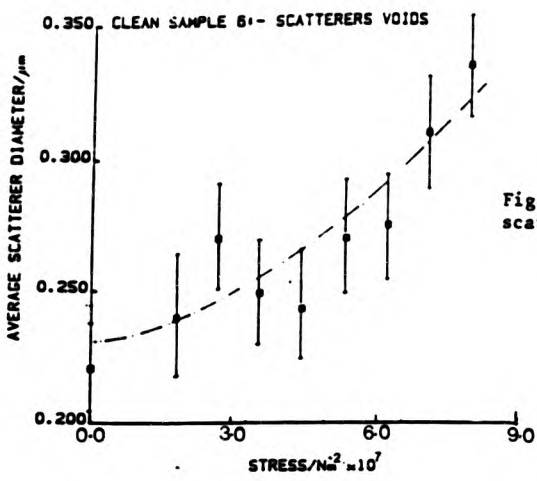


Fig 52. Variation of scatterer diameter with applied stress.

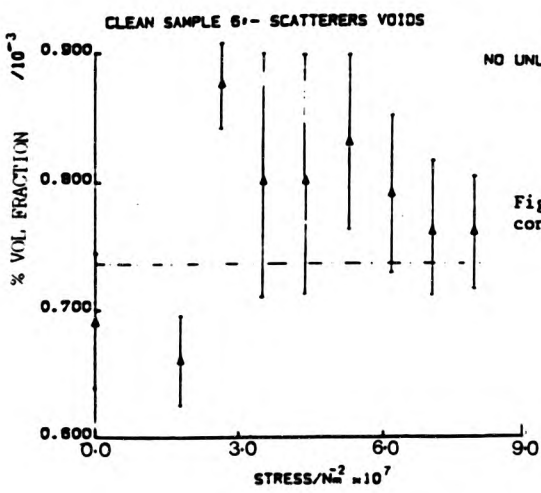


Fig 53. Variation of concentration with applied stress.

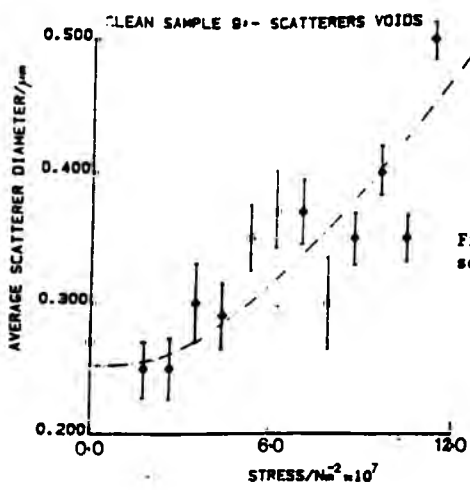


Fig 54. Variation of scatterer diameter with applied stress.

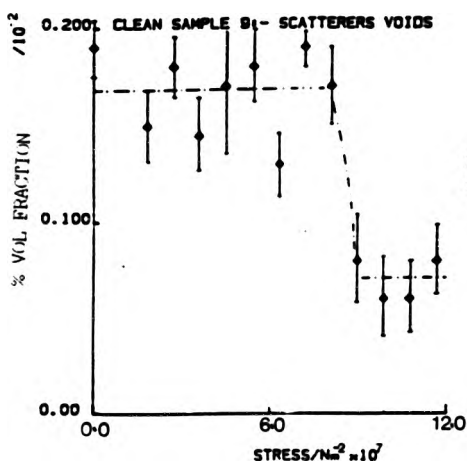


Fig 55. Variation of concentration with applied stress.

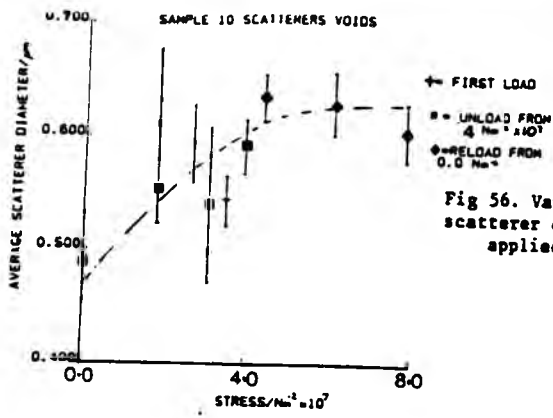


Fig 56. Variation of scatterer diameter with applied stress.

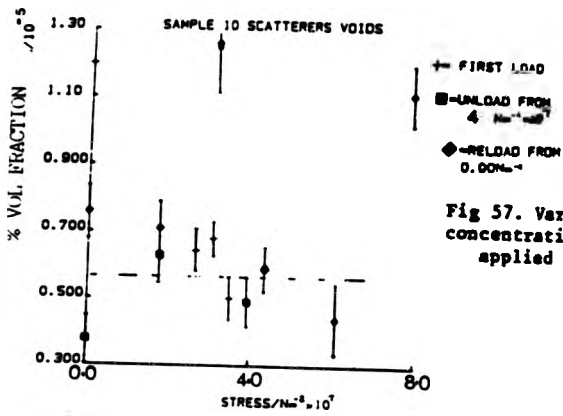


Fig 57. Variation of concentration with applied stress.

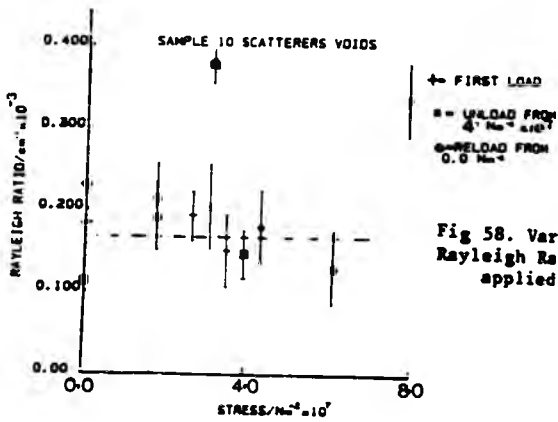


Fig 58. Variation of Rayleigh Ratio with applied stress.

size with stress for the inhomogeneity data for applied stresses above σ^* . Fig 54 also shows an increase in scatterer size with stress. The size remains constant until a stress value of $4 \times 10^7 \text{ Nm}^{-2}$ where an increase in size occurs progressively with increasing stress. At around $6 \times 10^7 \text{ Nm}^{-2}$ the concentration decreases rapidly to a new stable value. This could be regarded as a step type behaviour. A reverse step behaviour was observed as the epoxy underwent electrical stress. This has been linked to yield occurring away from the scattering volume causing a relaxation to occur within the scattering volume. Yield in the electrical case is thought to result from the action of the compressive mechanical force associated with the electric field (see chapters 6 and 7). These two behaviours may be linked and the reverse in the step may be due to the opposite nature of the stresses involved.

The behaviour in figs 54 and 55 is similar to that of Figs 52 and 53, but it is more amplified and suggests that dominant void growth exists within the scattering volume.

Figs 56 and 57 exhibit a similar behaviour of void size and concentration as Figs 52 and 53 until a stress value of $4 \times 10^7 \text{ Nm}^{-2}$ where the value of size of scatterer with stress appears to reach a plateau. This

value of size is $0.6 \mu\text{m}$ and is the largest size of scatterer observed. This could occur as a result of a critical size of void above which the matrix will not deform to allow the void to grow. The variation of concentration suggests that the concentration of scatterers may begin to increase once the size has reached this plateau, suggesting that possibly a number of voids will grow to a point where coalescence may occur leading to failure. Alternatively it is possible that not all voids have the potential to cause failure. This is most likely as the concentrations involved are so low that that coalescence is unlikely to occur. Voids in a region outside the scattering volume may be growing preferentially to those in the scattering volume and this growth may lead to the eventual failure of the sample.

5.2.6 Behaviour of gas filled samples.

The size of void observed for the gas filled samples was over all larger than those observed in the clean samples. The behaviour of gas filled samples containing both CO_2 and N_2 under stress was investigated. Trends were difficult to establish as no two samples behaved in exactly the same way under stress. Some of the response of these samples to stress will now be outlined. Figures 59-64 give the results of stressing the carbon dioxide filled samples. The nitrogen filled samples behaved similarly to the clean samples

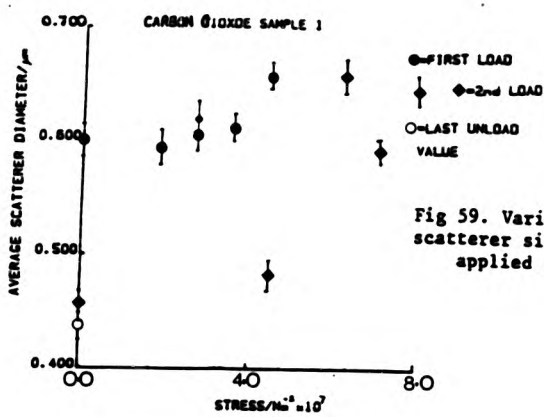


Fig 59. Variation of scatterer size with applied stress.

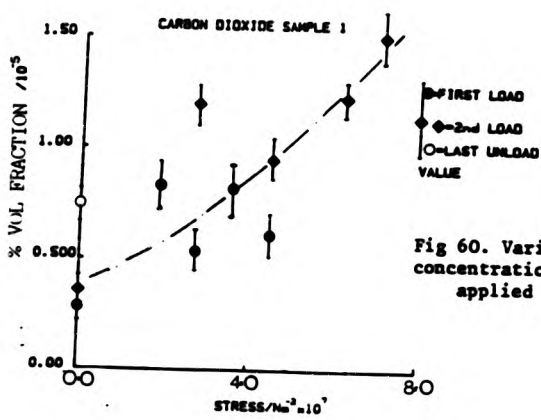


Fig 60. Variation of concentration with applied stress.

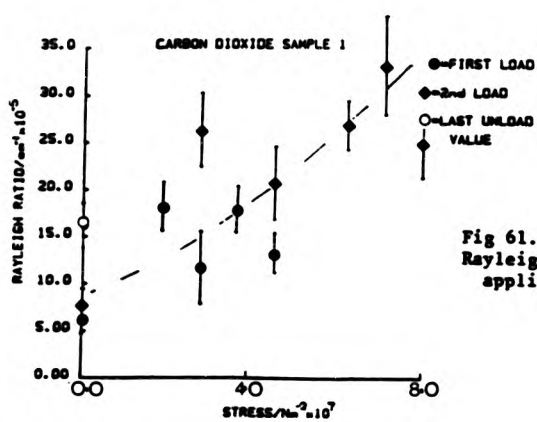


Fig 61. Variation of Rayleigh Ratio with applied stress.

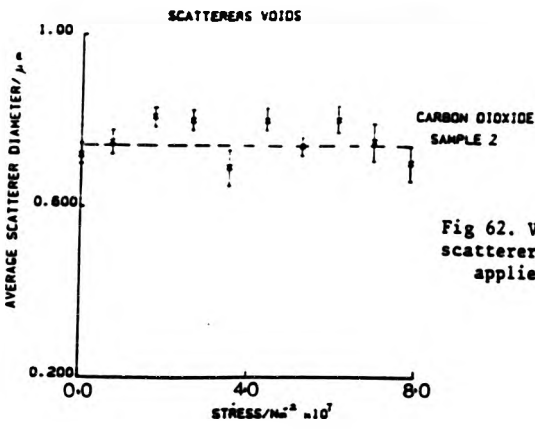


Fig 62. Variation of scatterer size with applied stress.

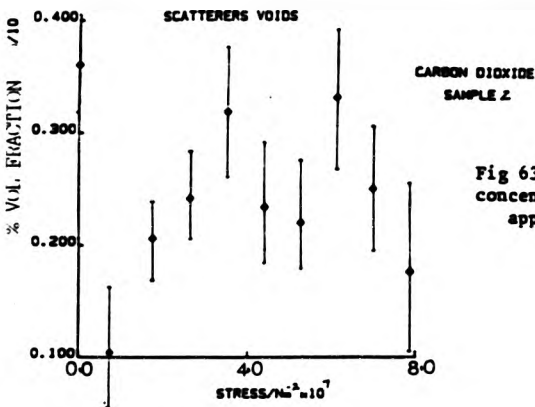


Fig 63. Variation of concentration with applied stress.

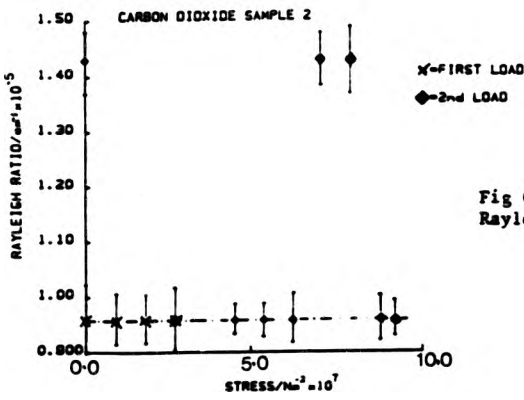


Fig 64. Variation of Rayleigh Ratio with applied stress.

that contained a larger concentration of voids with an increase in void size with stress and a decrease in concentration.

There appears to be very little effect of stress on the scatterers in the CO₂ filled samples, although scatterer growth occurs with increasing stress in some cases (fig 59 and 60). There is too much scatter on the values of concentration for any definite trend to be observed. The initial stress free scattering characteristics from CO₂ and N₂ containing samples are compared with degassed samples in table 14.

Table 14. Summary of void sizes and concentrations observed

Sample	Initial void size/ μm	Initial % vol concn.	Rayleigh Ratio/cm ⁻¹	General Comments
6	.234±0.084	0.69±0.06x10 ⁻³	5.0±.5x10 ⁻⁴	all voids grow slowly with stress
9	.270±0.051	.19±.02x10 ⁻²	6.±.5x10 ⁻⁵	faster preferential void growth with stress
10	.495±.044	.73±.04x10 ⁻⁵	.1±.06x10 ⁻³	all voids grow with stress
CO ₂ (I) saturated	.426±.008	.35±.06x10 ⁻⁵	.7±.12x10 ⁻⁴	small increase in size and concn.
CO ₂ (II) saturated	.72±.03	.36±.04x10 ⁻⁶	.95±105x10 ⁻⁵	no change
N ₂ 300% by volume	.9±.1	.81±.05x10 ⁻⁵	.1±.05x10 ⁻³	few voids grow with stress

NB Sample numbers represent voided but fully degassed clean samples.

5.2.7 Stress strain measurements.

Stress-strain measurements of clean samples were also made to establish the macroscopic yield behaviour of these materials and to seek correlations with the light scattering data. This was achieved using constantan strain gauges; type CEA-06-125UN-350 - (supplied by Wellwyn) of dimensions 3.5x2.0mm. These were attached to the gauge length of the dogbone samples, two for each dogbone, and connected to a strain bridge again supplied by Wellwyn Strain Instruments, along with a switch and balance unit so values from the two gauges could be recorded. Strain gauge one was placed above strain gauge two on the gauge length.

The samples were loaded in the same way as the light scattering samples and the strain recorded, Figs. 65 and 66 give examples of the results. Macroscopic yield was considered to be the point on the stress strain curve that departed from linearity. Table 15 gives the values of macroscopic yield found for these samples.

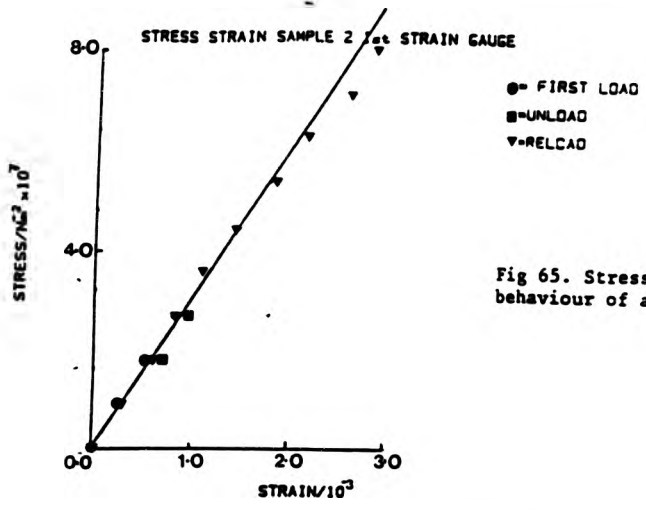


Fig 65. Stress strain behaviour of a dogbone sample.

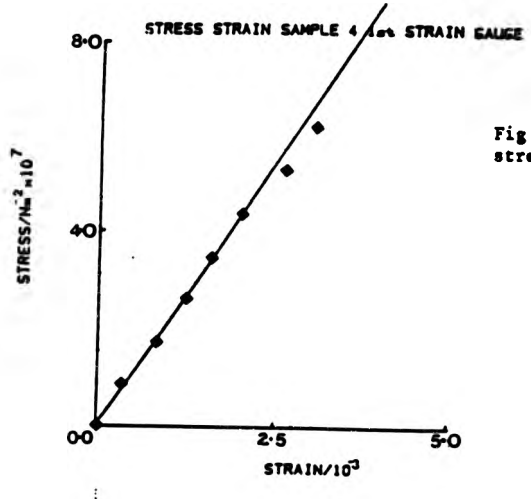


Fig 66. Another example of stress-strain behaviour.

TABLE 15 : Yield stresses observed.

sample	strain gauge	Yield stress /Nm ⁻² x10 ⁷
2	1	4.02+/-0.43
2	2	4.45+/-0.16
3	1	4.95+/-0.33
4	1	4.65+/-0.16
4	2	4.03+/-0.23

If we define the value of yield as the stress at which the stress-strain curve departs from linearity the values of yield stress agreed with those obtained from the light scattering data. Therefore it is likely that yield does occur at that point.

The average value of yield given by the light scattering data was $4.73 \pm 0.61 \times 10^7 \text{ Nm}^{-2}$ this is the same within experimental error as the value given by the strain gauge measurements of $4.41 \pm 0.40 \times 10^7 \text{ Nm}^{-2}$. Therefore we can assume that microscopic yield does occur at this point.

The percentage strain on the sample is -0.3% at the highest stress values. If we consider the scattering volume 0.5mm in diameter and a gauge length of the samples being typically 40mm then a strain of 0.3% on the gauge length is 0.12mm. This means that the sample will move in the scattering volume by 0.12mm, so throughout the stress period we will be sampling

slightly different scattering volumes. However the majority of the scatterers under observation will remain in the scattering volume throughout the experiment, also the movement is small so that we are likely to be sampling the same types of scattering volume throughout. This is substantiated by the trends observed. If we were sampling very different scattering volumes as the sample was stressed then no reproducible trends would be observed. As we do observe reproducible behaviour of scatterers then we can assume that the movement of the scattering volume under stress does not have a significant effect on the scattering behaviour.

5.3 DISCUSSION

Having established the trends in the light scattering data it is now necessary to discuss the behaviour in terms of the physical structure of the network and the type of defect present within that network.

5.3.1 Inhomogeneities

Figs. 67 and 68 show the typical scattering behaviour of inhomogeneities under uniaxial tensile stress.

The important points of the response of these scatterers to stress are:

- (i) Before σ^* the system is fully reversible. This suggests that yield occurs at σ^* .
- (ii) The value of scatterer size at σ^* is the same as the initial scatterer size.
- (iii) Beyond σ^* the size of scatterer increases and the concentration decreases, the value of χ^2 on the data increases.
- (iv) Scatterer size exhibits a peaking behaviour between zero stress and σ^* , whilst the concentration steadily increases.

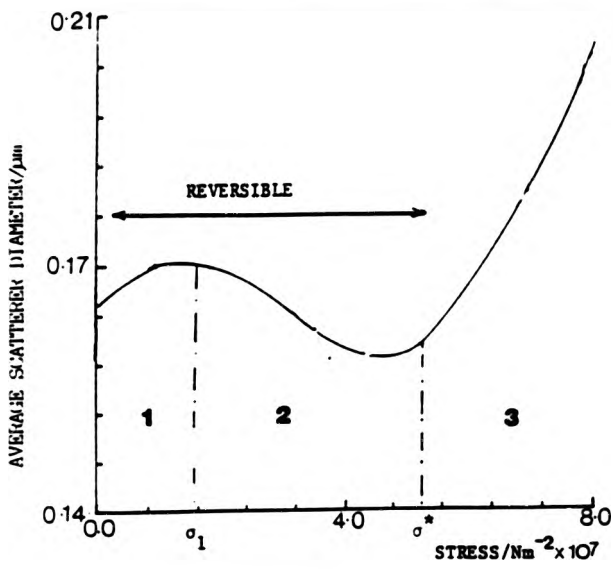


Fig 67. Reproducible trend in scatterer size that inhomogeneities exhibit under tensile mechanical stress.

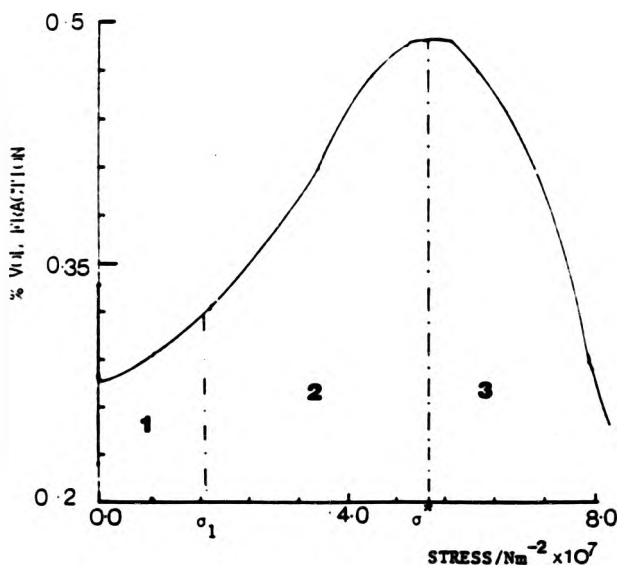


Fig 68. Reproducible trend in the concentration of inhomogeneities with tensile mechanical stress.

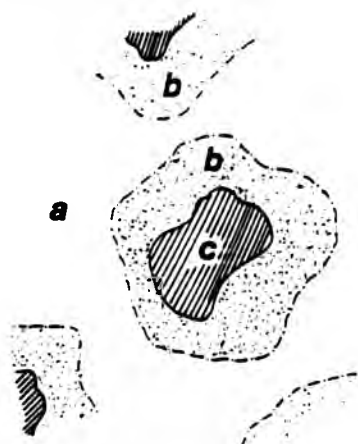


Fig 69. Model of inhomogeneities in the epoxy network.

The proposed structure of the matrix is given in Fig. 69 three regions are considered to exist within the network and are dependent on the volume crosslink density and the chemistry of the crosslinks. A three phase nature of this network has been suggested before [9].

The suggested structure of these regions are as follows:

'c' = highly crosslinked matrix consisting of mainly ester crosslinks.

'b' = a less densely crosslinked matrix per unit volume. In relation to 'c' a higher proportion of the crosslinks are chemically different from 'c' in that they are ether crosslinks.

'a' = a weak defected matrix interconnecting the 'b' regions.

The percentage volume fraction of these inhomogeneities is very small and the chemistry producing them is very diffuse. Therefore the overall picture of the inhomogeneity is not of close packed "hard cores" but of well separated scattering centres, occupying at the very most 0.5% of the actual sample volume.

This model is justifiable from the chemical kinetics of the system and the pre-existence of hydrogen-bonded aggregates in the prepolymer. The hydroxyl (-OH) groups react with the curing agent to give the crosslinks in the system (see Chapt. 4). Hydrogen bonded aggregates exist in the prepolymer [9-12]. These aggregates being rich in -OH groups act as preferential reaction sites for the curing agent. As there is a high concentration of -OH groups in the aggregates the resulting network formed at the position of the aggregations will be highly crosslinked. The chemical type of crosslink will be predominantly ester crosslinking due to the initial dominance of ester crosslinking in the reaction kinetics [19-20] this gives region 'c'.

H-bonding is less likely to occur at high temperatures. At the mixing and curing temperatures used the extent and definition of the aggregates will be reduced but in CT200 up to 150^o C the resin never adopts a full unassociated liquid behaviour [10].

As the reaction proceeds away from the initial aggregate there will be fewer -OH groups available for reaction and the matrix will become less densely crosslinked at these points. The reaction will also have proceeded to the point where ether crosslinking becomes more competitive therefore there will be a chemical difference between the initial crosslinks and the ones now being produced. This gives us region 'b'. This reaction will proceed to give a granular but chemically diffuse type of system which will be weakly interconnected by matrix 'a'. Here very few -OH groups will be available for crosslinking as there are likely to be a high number of $n=0$ oligomers present away from the initial hydrogen bonded aggregate. Therefore there exists the possibility of all types of defect occurring as outlined in Chapter 4.



Fig 70. Second possibility of network inhomogeneity.

There is a second possibility that two or more 'c' cores exist within one region 'b', Fig. 70 this will depend on the effective volume concentration of the initial aggregates, which is extremely small and therefore this is unlikely.

The three phase model can now be used to explain the trends found in Figs. 67 and 68. Although there are chemical differences between the regions 'a', 'b' and 'c' before stress the difference in density will be small ($< 0.5\%$) the lower limit being set by thermal density fluctuations. A greater contrast will exist between 'b' and 'c' due to the less diffuse chemical nature of the boundary between 'b' and 'c' than 'b' and 'a'.

Initially only a few 'c' cores will be apparent to light scattering, so the initial scattering profiles will be of a small number of small scatterers of the order of 0.01 % volume fraction. On application of stress to the system the weakest part of the matrix (region 'a') will deform the most. This gives rise to a greater contrast in density between region 'a' and 'b' than regions 'b' and 'c' for those locations where the 'a' regions are particularly weak and deform first. So the 'b' regions will become the dominant scatterers. Application of stress will exaggerate the density difference between the regions so more will become

apparent to light scattering increasing to 0.015% vol. fraction. Therefore the scatterer size and concentration will both initially increase on application of stress. Figs 67 and 68 show this up to the point σ_1 where now the scatterer size begins to decrease with stress. This can be explained if we consider what is happening in region 'a' at the point σ_1 more strain is transferred to region 'b'. This additional deformation with increasing stress giving rise to a decreasing contrast between 'a' and 'b' and a greater contrast between 'b' and 'c'. So the apparent scatterer size will decrease with stress and the concentration increases as more centres are revealed. The rise in concentration may not be as dramatic as shown in the figures due to the fact that the variation of differential refractive index was not taken into account as explained earlier.

At the point σ^* 'b' will have deformed as much as it can and the 'c' regions will again totally dominate the scattering so the scatterer size will return to its initial value. Up to this stress the behaviour is fully reversible.

Beyond σ^* yield occurs in region 'a' and the light scattering behaviour becomes irreversible. On yield voids are produced and grow with the application of stress, as shown by the increase in scatterer size after σ^* . Provided there are no other defects present

in the matrix it can be assumed that the voids will continue to grow with stress until eventual crack propagation and failure of the sample occurs.

Proof of yield occurring at σ^* comes from the stress strain curves of the epoxy resin Figs. 65 and 66. Before σ^* the macroscopic stress-strain curve is reversible, above this value this is not so. The fact that the sum of squares on the fit to the data increases beyond σ^* when the data is fitted (assuming inhomogeneities are present) indicates that scatterers other than inhomogeneities exist. The improvement on the sum of squares on the data when fitted assuming a distribution of voids show that voids are created beyond the point σ^* . This creation is irreversible as these voids continue to exist at zero stress.

The three phase system can be modelled using a spring and dash pot system Fig. 71 with different spring constants k_1 , k_2 and k_3 for the different areas of crosslink density in the matrix. The matrix will then deform as this model, k_3 representing 'a' will take most of the strain initially when this spring is fully extended then k_2 (as 'b') will extend and so on until k_3 spring breaks. However if any calculations were to be made using this model the limit of the extension of k_3 is required. As this is not known exact calculations of the extensions of regions 'a', 'b' and 'c' for

different stresses cannot be made.

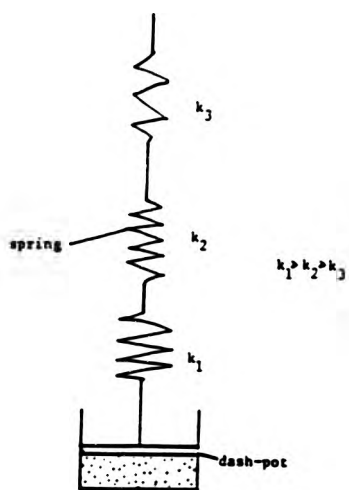


Fig 71. Spring and dash-pot model of matrix

5.3.2. PRE-EXISTING VOIDS IN THE NETWORK.

In contrast, the other type of initial defect present in the epoxy resin, i.e. is microvoids, show an increase in size immediately on applying the stress. However their behaviour depends on the initial concentration. At relatively low concentrations all voids will grow at a slow rate. At higher concentrations a smaller number will grow relatively quickly. Preferential growth at higher concentrations could be due to the growth of some voids restricting the growth of others Fig. 72. Typical concentrations of

-5

voids range from 0.8×10^{-5} to 0.0015 % vol. fraction. This is much smaller than the range of concentrations of inhomogeneities of 0.01-0.03 % vol. fraction.

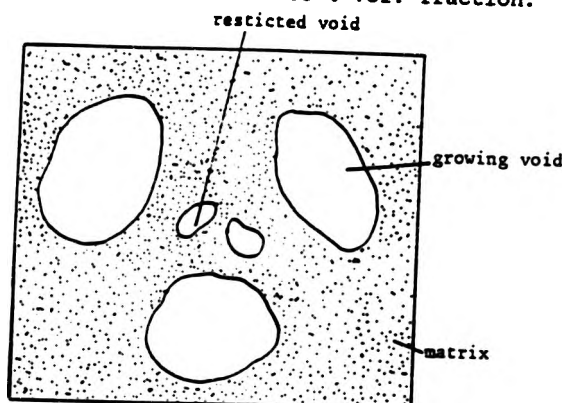


Fig 72. Preferential growth of voids.

Voids can be formed in a degassed system [10] from:-

- (i) residual gas that cannot be pumped out.
- (ii) low concentration or absence of cross-links in region 'a'.
- (iii) volatile impurities and low molecular weight material condensing during reaction.

It can be seen in the gas filled samples that the nitrogen did not 'dissolve' in the resin too well and large gas bubbles were produced. The carbon dioxide did modify the matrix to some extent and possibly acts as a low molecular weight plasticizer on it due to the lack

of void growth under stress.

A voided sample could lead to failure, should the void reach a critical size and lead to crack propagation.

The fact that voids grow immediately stress is applied is due to their acting as stress concentrators. If we consider a spherical cavity radius 'a' in a bar under a uniform tension S [96] Fig 73.

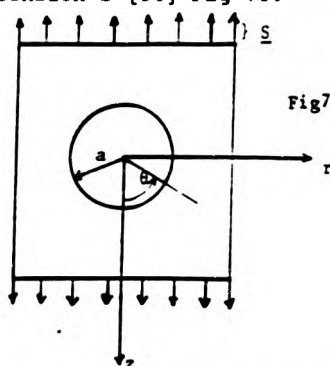


Fig73 . Schematic for void growth.

Then the stress in the direction of z

$$\sigma_z = S \left\{ 1 + \frac{4-5\nu}{2(7-5\nu)} \frac{a^3}{r^3} + \frac{9\nu}{2(7-5\nu)} \frac{a^5}{r^5} \right\} \quad (54)$$

ν = the Poisson's Ratio


at $r=a$ the max value is given by

$$(\sigma_z)_{\max} = \frac{27-15\nu}{2(7-5\nu)} S \quad (55)$$

the stress at an angle θ in the plane $z=0$ will be

$$\sigma_\theta = \frac{15-3\nu}{2(2-5\nu)} S \quad (56)$$

Therefore the stress is larger in the z direction than in r so the void will become elipsiodal with void



growth, with its major axis in the direction of the applied stress. Therefore the error on the fit to the data should increase as the scatterers become less spherical (Table 13).

Finally both voids and inhomogeneities exist together and will be deforming together, therefore crack initiation could occur at various different points in the sample. Fig. 74 is an optical micrograph of the fracture surface of one of the clean samples used. This shows that initiation has occurred at two points indicated by regions A and B and the arrest of A showing that this did not lead to failure. The region B is seen to have been initiated at b1 along the arrest point of region A. This suggests that the deformation leading to failure is inhomogeneous due to the presence of the two types of defect. This introduces a connection between local structure and potential failure and that there are voids which may be more disposed to failure as a result of their location and stress concentration, or a consequence of the local network structure surrounding the void.

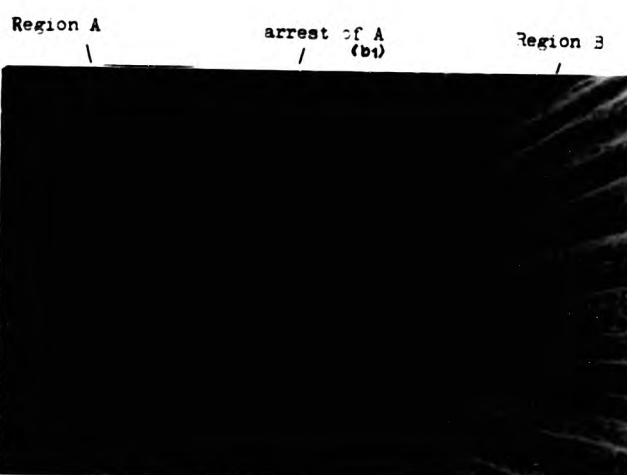
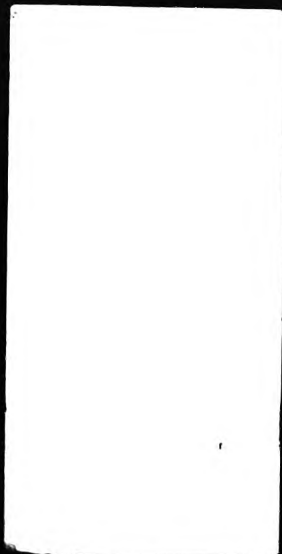


Fig 74. Fracture surface, showing crack arrest and two regions of crack growth.

5.4 CONCLUSIONS

The final conclusions to this chapter are:

- (i) The epoxy resin system investigated does not possess an ideal network and inherent defects exist, these are inhomogeneities and voids.
- (ii) The microstructure of the epoxy resin is complicated and consists of at least three different regions of crosslink density.
- (iii) There is also a difference in the chemistry of the crosslinks between the most and least densely crosslinked regions.
- (iv) Voids are formed and grow under mechanical stress, and premature failure of the sample occurs in the weakly crosslinked region of the matrix.
- (v) Voids in the sample also grow with applied stress leading to the failure of the sample. For large concentrations of voids few grow relatively quickly, for smaller concentrations relatively more voids grow at a slower rate.
- (vi) Addition of gas to the samples had two effects depending on the gas added. In nitrogen added samples the voids grow as for the clean samples at high concentrations although their initial size was larger. However carbon dioxide added to samples showed that it may have had a plasticizing effect on the

network.

(vii) The presence of network inhomogeneity and a non uniform void distribution leads to non uniform deformation behaviour and preferred locations for yield and fracture. This depends on the weakest regions of the network and their spatial distribution.

CHAPTER 6.

ELECTRICAL STRESSING OF EPOXY RESINS.

6.1 Introduction

Having established that results could be obtained on the behaviour of microstructure and microvoids during deformation under mechanical stress using light scattering, the same technique was applied to the samples under both d.c. and a.c. electrical stress. This was to attempt to discover the possible initiation processes of breakdown under electrical stress and the possible role of microstructure in this. Also to see if a link between the failure processes under mechanical and electrical stress could be established.

6.2. Preparation of pin tips

The very fine tungsten tips used for the samples were prepared from the same etching technique used by Shibuya [49]. A 20% by weight aqueous potassium hydroxide (KOH) solution was used for etching. This was floated on top of insulating carbontetrachloride (CCl_4) to a depth of 5-10 mm. Two tungsten electrodes 0.5 mm in diameter were placed in the liquids so that roughly 5 mm of the rods dipped in to CCl_4 . A potential of 6V was applied to the tungsten wires and the current flowing in the electrolyte eroded and cut the wire. The section of wire in the KOH became thinner and was drawn

out under the weight of the bottom portion of the wire. Eventually the lower section dropped off - this took about 20 minutes. The potential to the tip was immediately switched off so no further etching could take place as the tip was required to be as fine as possible.

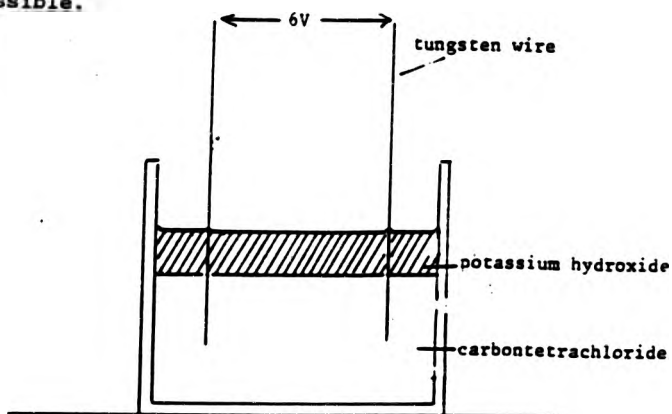


Fig 75 Experimental setup for etching pintips.

The tips produced were long, thin, very fine and possessed good profiles, $\sim 0.2-0.6 \mu\text{m}$ in diameter, Figs. 76 a,b,c show examples. These pin tips were observed under SEM to determine if they had good enough profiles for use, and to measure the tip diameter.

A pin-plane configuration was used for all the experiments. This produces a highly divergent field at the pin tip and, therefore, relatively low voltages would be sufficient to induce voids in the system.



(a) x150 mag.



(b) x1500 mag.



(c) x60,000 mag.

Fig 76. Scanning electron Micrographs of a typical pin tip.

The maximum electric field at the pin tip for a pin/plane configuration was calculated by Shibuya [49,96] and is given by

$$E_{\max} = \frac{2V}{[R \ln(4d/R)]} \quad (57)$$

Where V is the applied voltage value, d and R are defined in Fig. 77.

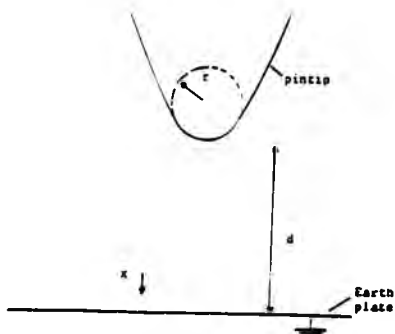


Fig 77. Schematic of pintip and gap.

Shibuya [49] also calculated the field at a distance ' x ' from the tip in the direction shown in fig 77. This decays quickly (Fig. 78). Hence, E will be smaller in the scattering volume as this was 0.5mm away from the pin tip. Also this does not account for corrections due to space charge tip blunting.

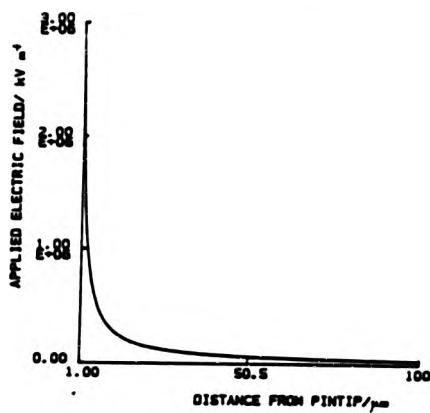


Fig 78. Distribution of electric field away from pintip.

From Shibuya's results [46,49] macroscopic voids should be formed in up to 1 hour above a stress value of $3.0 \times 10^8 \text{ Vm}^{-1}$. This value has been used as a guide line for the stress values required in this work.

The tips were embedded in the mixed anhydride and resin and these samples were cured in the same way as described in Chapter 4. The samples were faced in the lathe until the pin-plane separation was ~5 mm. This was eventually measured using a travelling microscope.

The modification of the system for electrical stressing has already been discussed in Chapter 3. The following section discusses how the samples were stressed and the results of that stressing.

Fig 79 and 80 gives the circuit diagrams for both the d.c. and a.c. circuits, these included a large value resistor to act as a current limiter and a smaller

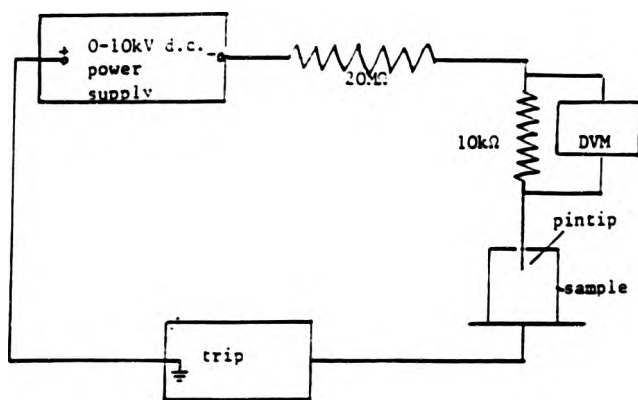


Fig 79. Circuit for d.c. stressing

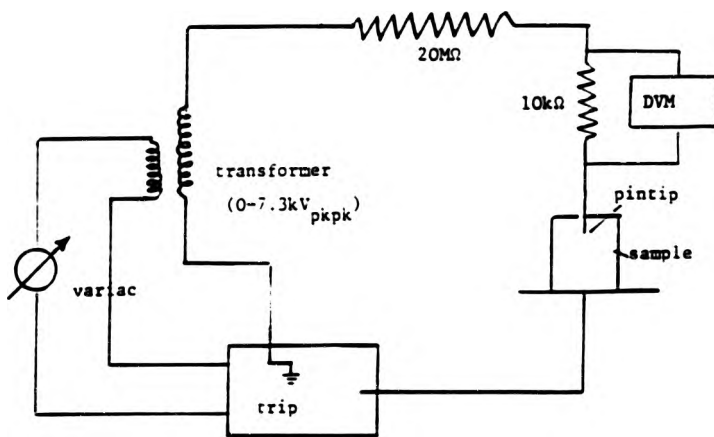


Fig 80. Circuit for a.c. stressing

resistor across which the voltage could be read using a digital voltmeter (DVM). This was to enable the current in the circuit to be calculated using Ohms law, in order to monitor the current passing through the sample. Any rapid increase in current would indicate that the sample was approaching failure. A trip was also included in the circuits on the low voltage size of the sample to act as a safety precaution against large currents flowing in the event of failure of the sample.

6.3 RESULTS OF STRESSING OF SAMPLES

6.3.1. D.C. Stressed Samples

It was considered that under d.c. more damage would be caused to the sample at a faster rate if electrons were injected into the sample rather than extracted; therefore a negative potential was applied to the pin tip.

The samples were stressed on average over a period of three days and the applied stress was released overnight. Shibuya's calculation for the stress field required to give voids in up to 1 hour, was used as a guide to determine the upper limit of applied stress. For all the pin tips used, 7 kV would give, in the absence of space charge, a peak stress value well above $3.0 \times 10^8 \text{ Vm}^{-1}$, the value above which Shibuya observed harmful void growth for an alternating applied

voltage. Therefore it was thought that some detrimental effect on the resin should occur at the d.c. stresses involved.

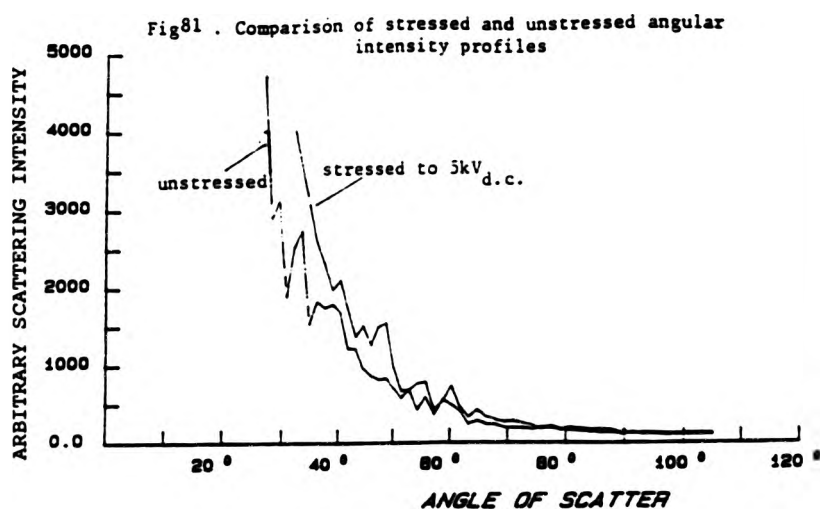
The scattering volume investigated for each sample was 0.5 mm below the pin tip. This was to ensure that no flare from the pin tip masked the scattering from defects in the network. For all the samples used no scattering volumes containing only inhomogeneities were found. Only scattering volumes containing a population of microvoids could be investigated. The initial size of microvoid found was similar to that found in the samples placed under mechanical stress. The exact concentration of these voids could not be obtained as flare from the pin tip could not be totally eliminated and would add a background to the scattered intensity. This background will vary from sample to sample. However it will remain constant for a given sample as it undergoes electrical stressing. Hence percentage volume concentrations could not be obtained for these samples, whilst the relative concentration changes with stress for each sample could be monitored.

The presence of microvoids around the pin tip could be produced,


- (i) in the preparation of the sample when the wire was inserted in the sample
- (ii) by local mechanical yield around the pin tip. The

tip is very small therefore the stress around it is large and it is possible for yield to have occurred in the vicinity of the tip and voids therefore produced.

Fig.81. shows the change in profile of scatterers with d.c. applied electrical stress. The changes for these samples with stress was not as pronounced as for the mechanically stressed samples. This is due to the fact that the type of the scatterers does not change with stress as microvoids are present in the scattering volume throughout the stress cycle. The stresses used were not large enough to cause the sample to tree.



From the scattering profiles obtained no completely reproducible behaviour was found. However



some common features were observed. Often there was an apparent increase and decrease in scatterer size with the application and release of applied stress showing a similar behaviour to the growth of voids with mechanical stress. The scatterer concentration change behaved in the opposite sense to the scatterer size. On release of stress, the change in size and concentration exhibited a step type of behaviour (Figs. 82-85). In some cases these step changes occurred during a stressing cycle and in a number of cases this first occurred at apparent stress values around $2.0 \times 10^9 \text{ V m}^{-1}$ (Figs. 86-88)

The overall behaviour of the scatterers with stress varied from sample to sample. This may have been due to the remoteness of the scattering volume from the pin tip which was the highest stress point, and the differing sizes of pin tip used giving different values of the field between samples for the same applied voltage. There will be some internal mechanical strain in the samples due to the presence of the pin tips in the system. The behaviour in the scattering volume will be effected by the value of this strain. This will vary from sample to sample due to the different size pin tips.

D.C. sample 4 showed that after an initial decrease in scatterer diameter (Fig 82) overall scatterer size

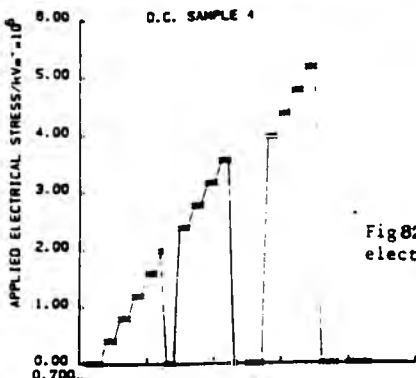


Fig 82 . Value of applied electric field for each data file.

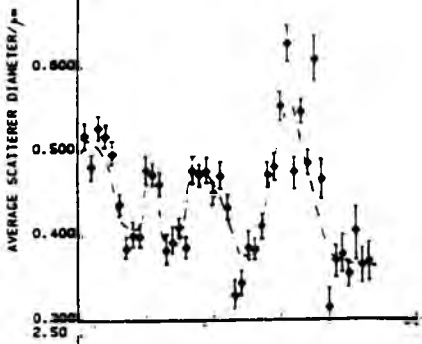


Fig 83. Variation of scatterer diameter with applied stress.

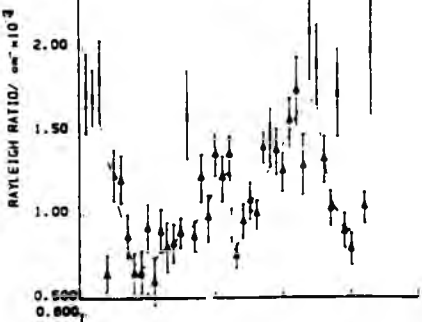


Fig 84. Variation of Rayleigh Ratio with applied stress.

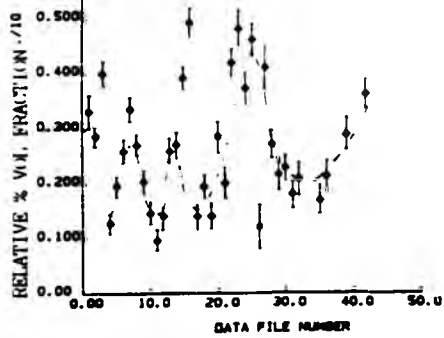


Fig 85. Variation of concentration with applied stress.

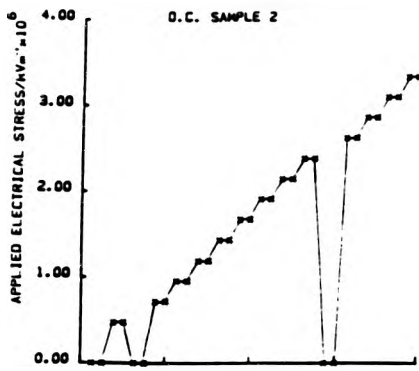


Fig 86. Value of applied electric field for each data file.

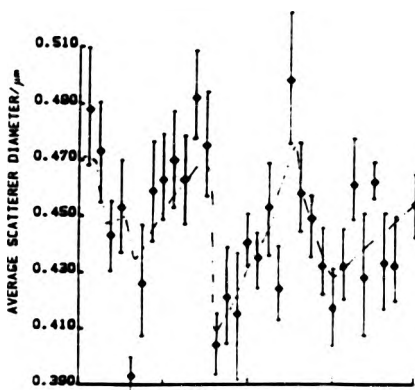


Fig 87. Variation of scatterer diameter with applied stress.

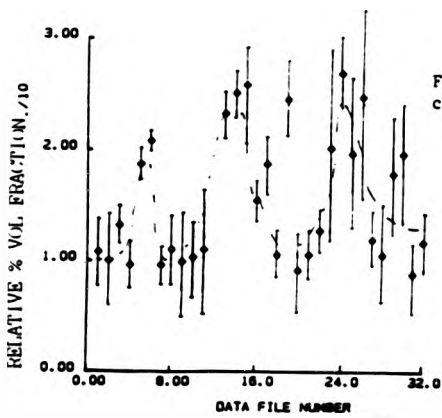


Fig 88. Variation of concentration with applied stress.

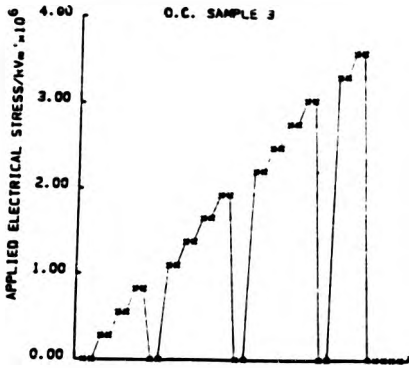


Fig 88. Value of applied electric field for each data file.

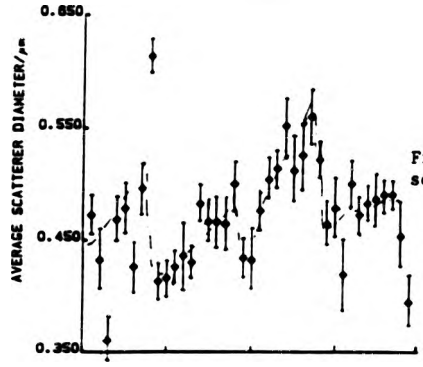


Fig 90. Variation of scatterer diameter with applied stress.

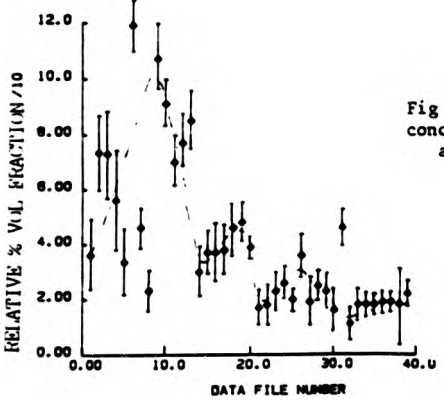


Fig 91. Variation of concentration with applied electrical stress.

increased with applied stress and then returned to a smaller value on the release of stress by a step type of change. Interestingly the value returned to was smaller for the higher stresses applied, and smaller than the initial unstressed value. This suggests that the sample is modified in some way with the application of stress, possibly by the introduction of a population of small microvoids or a change in the local strain condition. If the initial and final concentration values are ignored (Fig 85) then the behaviour of concentration with stress would bear out the idea of formation of small microvoids with stress, as the concentration values increase on each release of stress. However the initial and final values do not fall into this trend and lead to some ambiguity as to what is occurring. The scatterer size shows a decrease at a mid stress of $-1.0 \times 10^6 \text{ kV m}^{-1}$ and also during the last stress period before the stress is released. This decrease occurs at $4.0 \times 10^6 \text{ kV m}^{-1}$, and is not as sharp as the steps found on the release of stress. The value of Rayleigh Ratio varies directly with stress. It increases with applied stress and decreases on release of stress.

D.C. sample 2, Figs 86-88, shows a similar behaviour to D.C. sample 4 but it also exhibited a switching from large to small scatterer sizes and low to high

concentrations whilst under stress. This occurred at a value of applied electric field of $1.5 \times 10^6 \text{ kV m}^{-1}$.

D.C. sample 3 Fig 89-91 showed similar behaviour. In this case the scatterers increased in size with applied field and decreased on release of field. However the last step decrease in size at the highest field values, was to larger scatterers. The reverse of sample 4 e.g. after stressing to $0.9 \times 10^6 \text{ kV m}^{-1}$ the size of scatterer on release of stress was $0.39 \mu\text{m}$. After stressing to $1.95 \times 10^6 \text{ kV m}^{-1}$ the scatterer size was $0.43 \mu\text{m}$, the concentration of the latter being smaller Fig 91, although the same trend in increase in concentration on release of stress was still observed. These results indicate that in this case application of the electric field had caused irreversible void growth. Again there is a difference in behaviour in the initial and final values as for sample 4. Also two mid stress switching events were observed one at $2.8 \times 10^6 \text{ kV m}^{-1}$ and a final switching from large to small scatterers appears to have occurred before the release of the stress at a value of $3.5 \times 10^6 \text{ kV m}^{-1}$ as with sample 4.

A further long stress experiment was carried out to determine if the switching was purely due to release of stress. The sample was stressed throughout the whole range of voltages from 0-7.5 kV d.c. without release. Figs 92-94 give the results.

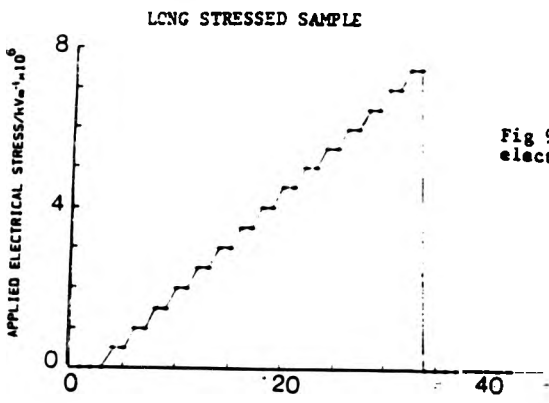


Fig 92 Value of applied electric field for each data file

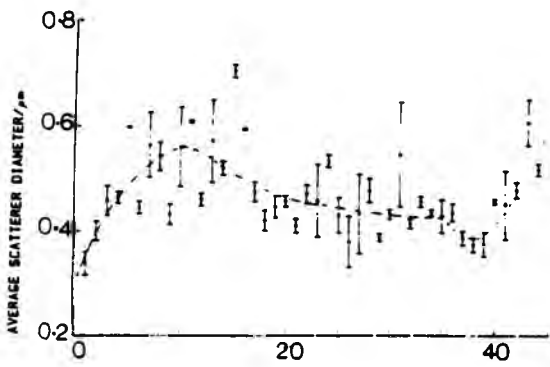


Fig 93 Variation of scatterer diameter with applied stress.

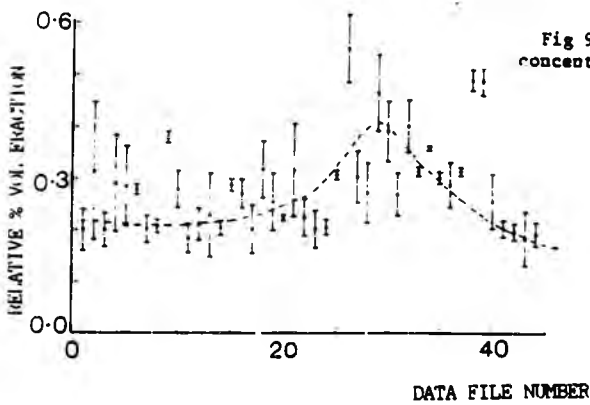


Fig 94 Variation of concentration with applied stress.

One step was observed throughout the whole stress period, at a maximum electric field of $2.0 \times 10^6 \text{ kV m}^{-1}$. Below this value the size of scatterers increases with stress and after this value the size of void decreases and the sample exhibited a steady slow decrease in size until stress was released.

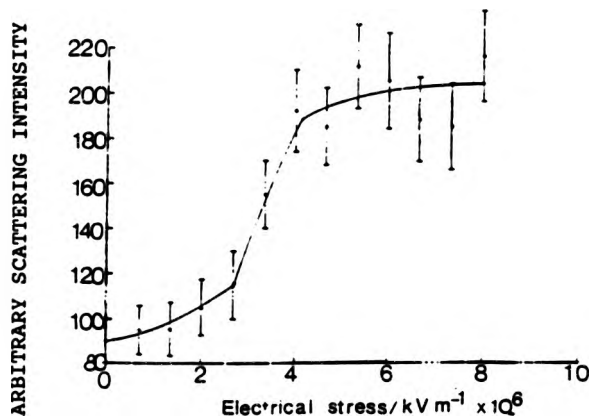


Fig 95. 90° Scattering intensity at pin tip with applied electrical stress.

If this behaviour is compared with the previously stressed samples then the trend in behaviour is the same between the samples if the switching is ignored as this obviously results from the release of stress. For example d.c. sample 3 shows a step at $2.8 \times 10^6 \text{ kV m}^{-1}$ and sample 2 shows a decrease in scatterer size at $1.5 \times 10^6 \text{ kV m}^{-1}$. Allowing for experimental error these are the same as the switch value for the long stressed sample and suggests this behaviour results from a relaxation process occurring within the sample.



Relaxation will occur as a result of yield occurring in another part of the sample. The weakest point within the sample must be the pin tip-matrix interface. A further experiment was carried out on the 90° scattering at the pin tip itself to see if there was a change in the scattering intensity around the applied maximum stress value of $2.0 \times 10^6 \text{ kV m}^{-1}$. Failure of this interface will lead to a larger differential refractive index and therefore a larger scattering intensity. Fig 95 illustrates the results, and shows a large change in intensity at around the expected stress value substantiating the idea that the steps observed during the mid-stress periods correspond to relaxation occurring in the scattering volume due to failure at the pin-matrix interface. It is important to note that the field value required for space charge tip blunting to occur [45] is -10^6 kV m^{-1} , the value above which the mid stress step changes are observed.

After the samples were stressed some were cut so as to obtain a very thin section including the pin tip. These were highly polished to enable observation of the tip under optical microscopy to see if there was any deterioration of the area around the pin tip. Figs 96-97 show optical micrographs of sample 3. There was an increase in the stress around the double cusped area of the pin tip, and a small extension is just visible at the end of the tip. It is possible that this is the

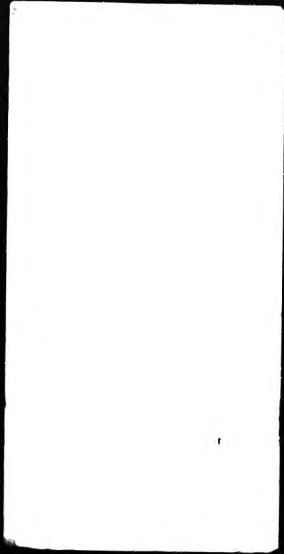


Fig 96. Photograph of d.c. sample pintip showing stress distribution around tip. (d.c. sample 3 x10mag.)

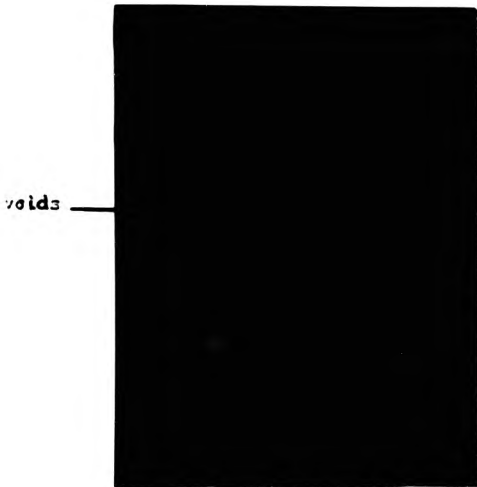



Fig 97. Same tip as fig 96 x20 mag. showing possible voids at tip.



initial stages of a tree. However no macroscopic treeing was observed.

6.3.2. A.C. Stressed Samples

The samples were stressed the same way under a.c. as for d.c. although the voltage peak to peak range was 0-7.3 kV . These were stressed in steps of 0.33 kV and the stress released over night. The same type of void behaviour with applied stress and release of stress was observed under a.c. as for d.c. (Figs. 98-100). The samples exhibited a switching on release of stress. However growth was more rapid under a.c.. Voids reached the same size at one third the stress under a.c. than d.c.. The sample also shows a decrease in scatterer size and concentration at the larger stress values. This compares with the d.c. samples including the long stressed sample, indicating a relaxation in the scattering volume.

Once more, none of the samples went to failure. Optical micrographs were again taken of some of the pin tips (Figs. 101-102). Some deterioration of the samples was found, although there was no evidence of macroscopic treeing.

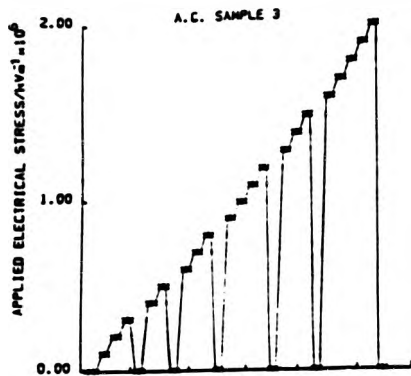


Fig 98. Value of applied electrical field for each data file.

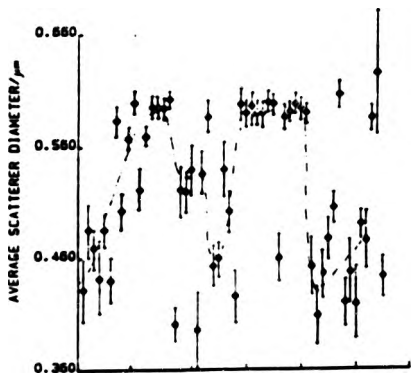


Fig 99 . Variation of scatterer diameter with applied electrical stress.

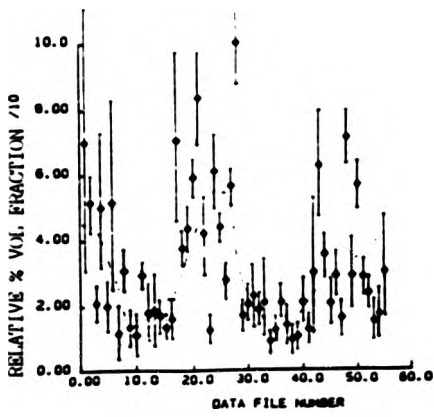


Fig:00 Variation of concentration with applied stress.

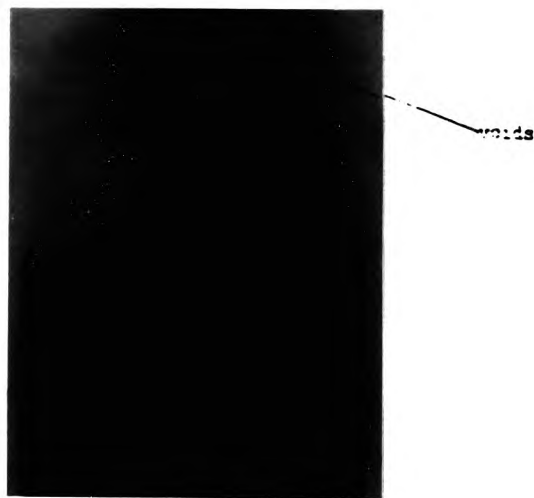
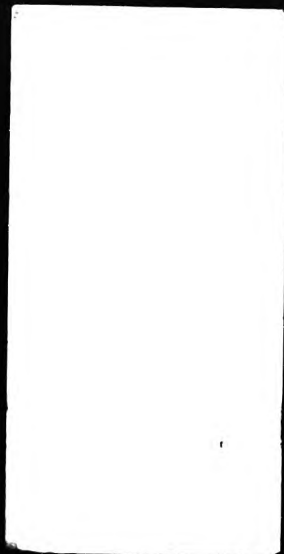


Fig 101. Photograph of pintip used in a.c. stressing, showing possible voids in sample. (x20mag.)

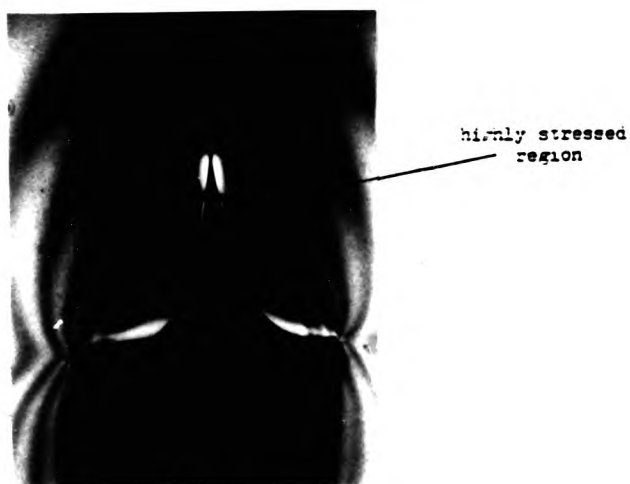


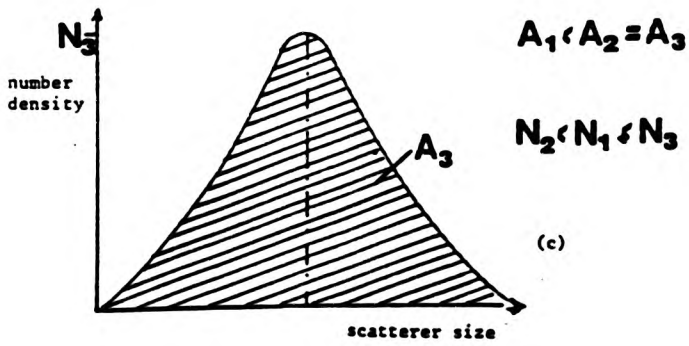
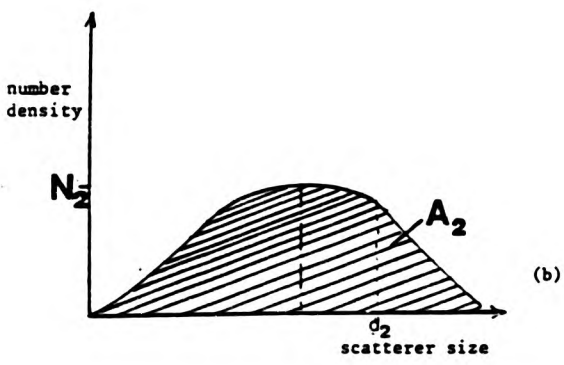
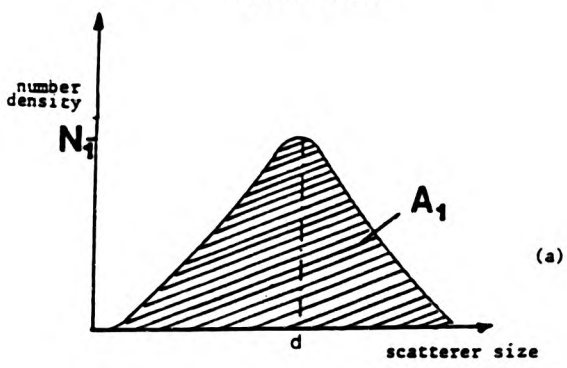
Fig102. Pintip showing highly stressed area and stress distribution.

6.4 DISCUSSION

Wholly reproducible behaviour was not observed from sample to sample of both the d.c. and a.c. stressed samples. However the same common features of step changes were observed for both types of field. This type of behaviour can be explained by considering the effect of stress on the population of microvoids Fig. 103a,b,c.

Fig. 103a represents the initial distribution of voids, the peak value is the size the scattering analysis programme will fit to. Application of stress will cause some voids to grow shifting and flattening the distribution Fig. 103b. As explained previously the fitting routine will fit to the most dominant scatterers which for the flattened distribution will be the largest value within the flattened peak (d).² Release of stress causes the voids that have grown to shrink back and the distribution will return to its original shape. In some cases the value of N will be larger than N ₁ showing that voids have been created in the stress cycle.³ In other cases the reverse was true indicating that the electrical stress had had some beneficial effect on the scattering volume reasons for this will now be discussed.

Fig 103 Change in scatterer distribution with applied stress



Zeller [45] has suggested that it is the mechanical force (F), produced by the applied electric field, that effect the deformation of the network under electrical stress (σ^M) (equation 58).

$$\sigma^M = \frac{\epsilon \epsilon_0 F^2}{2} \quad (58)$$

It is important to bear in mind that the field and consequently the electrostatic forces on the scattering volume will be much smaller than that at the pin tip. If a correction made for pin tip blunting due to space charge [45] then the space charge density for $r_0 < r < r_{sc}$ is

$$\rho(r) = \frac{2\epsilon \epsilon_0 E_c}{r} \quad (59)$$

where r_0 is the tip radius and r_{sc} is the effective radius due to space charge. E_c is the critical field required for the formation of a space charge region.

r_{sc} can be calculated from the applied voltage V and the pin-plane separation d

$$r_{sc} [1 + \log(4d/r_{sc})] = r_0 + (2V/E_c) \quad (60)$$

Therefore the field in the scattering volume (sv) is

$$E_{sv} = E_c / \sqrt{1 + 2r_{sv}/r_{sc}} \quad (61)$$

and the corresponding Maxwell compressive force is

$$\sigma_{sv}^M = \frac{\epsilon \epsilon_0 E_{sv}^2}{2} \quad (62)$$

at the pin tip interface r_0 . Then the stress at the interface due to space charge is

$$\sigma_{sc}^M = \int_{r_0}^{r_{sc}} \rho(r) E_c \cdot dr \quad (63)$$

this approximates to

$$\sigma_{sc}^M = \epsilon \epsilon_0 E_c^2 \left[\frac{r_{sc}}{r_0} - 1 \right] \quad (64)$$

Using parameters relevant to this work ($V = 10\text{kV}$, $d = 5\text{mm}$, $r = 0.15 \mu\text{m}$, $\epsilon = 3.6$ and $E = 10^9 \text{ Vm}^{-1}$) the space charge radius was found to be $4.3 \mu\text{m}$ and the force at the scattering volume was $6.8 \times 10^{-4} \text{ Nm}^{-2}$. From the results of the mechanically stressed data this force which is the maximum applied, will only weakly compress the existing microvoids. If the force at the actual pin tip is considered, then the value at the switch point, even if space charge pin tip blunting is considered, will be of the order of $8.8 \times 10^9 \text{ Vm}^{-1}$ close to the value required to produce failure. It can be assumed that failure of the pin/matrix interface does occur at this point and directly influences the matrix $500 \mu\text{m}$ away from the failure point. Evidence for failure of the pin/matrix interface comes from the 90° scattering intensity at the pin tip which shows a marked increase at the suggested value of pin tip/matrix failure. Application of the field initially causes voids to grow. Release of this stress then causes a relaxation and the voids decrease in size. This decrease also

occurs at the switching point in mid stress where it has been suggested that failure occurs at the pin/matrix interface causing a relaxation in the scattering volume.

Observation under optical microscopy of the cross-sectioned stressed samples showed that no treeing had occurred in the sample, although apparent E_{max} values of $2 \times 10^9 \text{ V m}^{-1}$ were used. The stressing on one of the samples outside of the photometer was undertaken for the same pin-plane separation. No treeing or electron discharge was observed even after stressing for 550 hours at 10 kV. This gives an $E_{\text{max}} \times t$ value of $10^{41} \text{ V m}^{-4} \text{ pk}$ and is far greater than the value calculated by Shibuya [45,52] of $10^{38} \text{ V m}^{-4} \text{ h}$ for breakdown. This value does not take into account space charge tip blunting, and suggests that space charge blunting does occur in the samples at the tip [45] reducing the size of the field.

Obviously the situation for the electrically stressed samples is more complicated than those placed under mechanical stress. Also the electrically stressed samples were not stressed to failure. However, both showed trends of void growth and relaxation with application and release of stress. The initiation processes therefore are considered similar through the influence of mechanical deformation processes resulting

from either electric or mechanical stress field.

6.5 CONCLUSIONS.

(i) Application of both a.c. and d.c. electric fields do have an effect on the pre-existing void distributions in the matrix.

(ii) In some cases this effect can be detrimental as voids have been shown to increase in size and number, due to the application of electrical stress. Release of stress causes the system to relax.

(iii) In some cases the reverse to conclusion (ii) has been observed. This may be due to failure occurring at the pin/matrix interface.

(iv) The samples investigated were ultra clean but it has proved impossible, in pin-plane specimens, to obtain a completely microvoid free scattering volume. It has been very difficult to initiate treeing and no trees have been observed in any of the samples.

(v) Although no treeing has been observed it is possible that the tip-matrix interface has failed.

It is suggested that this causes the step behaviour in the data observed during a stress period.

(vi) The long stressed sample showed a step in scatterer size and concentration in the range of

1.5-2.8 x10⁶ kV m⁻¹. Steps around this stress value were observed in other samples, and suggest this is a characteristic value relating to the failure of the pin/matrix interface.

(vii) The 90° scattering intensity from the pin tip increased at stresses around the value $\sim 3 \times 10^6$ kV m⁻¹. This strongly suggests that failure of the pin/matrix occurs at that point.

(viii) The overall behaviour of the long stressed d.c. sample compared with both d.c. and a.c. samples suggesting the same deformation processes occur with both types of stress.

(ix) Void growth with stress, and relaxation with release of stress, is common for both the electrically and mechanically stressed samples suggesting a link between the initiation of failure and deformation processes for both types of stress field.

CHAPTER 7

DISCUSSION

The aim of this work has been to determine if inhomogeneities exist within the bulk of the fully cured network of the epoxy resin system phthalic anhydride cured diglycidyl ether of bisphenol-A, and to determine their effects on the deformation and failure of the system under mechanical and electrical stress. Light scattering has been used throughout to determine this, as it is a non destructive technique which gives information on the bulk of the material throughout the whole of its stress cycle.

This work has shown that defects do exist within the bulk of the epoxy resin samples, even when they have undergone rigorous sample preparation that eliminates as far as is possible extrinsic impurities and defects. The defects present are both microvoids and network inhomogeneity. Although in this work few samples actually fractured in the photometer, the results indicate that both types of defect will lead to void growth and potentially to premature failure.

The results of the light scattering work have shown that the epoxy resin network is highly inhomogeneous with very different volumes of scatterers in different regions of the same sample. Typically the size of inhomogeneity was smaller than that of inherent voids. These were 80-200 nm in size, and the percentage volume fraction was 0.02%. The size of inhomogeneity was larger than that found in previous light scattering work on the epoxy resin prepolymer [9-12] although the percentage volume fractions were comparable. This indicates that the inhomogeneities in the fully cured system originate from the local aggregates in the prepolymer, and as such they are larger in the fully cured system. The size of inhomogeneity also spanned the range of the largest nodules observed under electron microscopy [4,5].

'Nodules' were observed under electron microscopy to have sizes ranging from 20 -100 nm. It is suggested that under light scattering the true extent of the inhomogeneity can be observed, especially when the sample undergoes tensile stress causing the contrast between the inhomogeneity and surrounding material to become greater.

A typical observed initial void size was 300 nm around twice the size of inherent inhomogeneities. The percentage volume fraction varied considerably from

10^{-6} to 10^{-3} % so there are relatively few inherent voids in the system. The size of void initiated under stress within the regions containing inhomogeneities was of the order of the size of the inhomogeneity. This suggests that the inhomogeneities act to nucleate voids under tensile stress.

Similar trends in scatterer behaviour were observed as the sample underwent stress. A network inhomogeneity containing three regions of crosslink density was deduced from the results. The network contains a highly crosslinked core surrounded by a less densely crosslinked matrix and these regions are interconnected by a weakly crosslinked network.

This type of inhomogeneity has been suggested before [9] and is substantiated by previous light scattering work [9,11,12] on the epoxy resin prepolymer, and the reaction kinetics of the system [19,20]. It is proposed that the inhomogeneities are a direct result of the existence of hydrogen bonded aggregates in the prepolymer. As these contain a high proportion of -OH groups they act as preferential reaction sites for the anhydride. Therefore the reaction will proceed from these initial aggregates and, as these areas have a large concentration of -OH groups, a densely crosslinked network will result. As

the reaction proceeds away from the initial aggregates the matrix becomes less densely crosslinked as there are fewer -OH groups for reaction. Also the chemistry of the crosslinks changes with time and the relative proportion of ether crosslinks increases with time. This is a direct consequence of the local increase in the concentration of carboxylic acid groups (an intermediate stage in esterification) which act to catalyze the etherification reactions. This accounts for the second area of crosslink density. Finally at the very end of the reaction process there will be less accessible -OH groups and free anhydride groups available for crosslinking, so the resulting network interconnecting the densely crosslinked regions will be relatively weakly crosslinked. This final region will have a greater ability to deform under stress, and will be the weakest part of the network where premature failure can occur.

The chemistry of the system can be changed to help produce a more homogeneous cured polymer. For instance if there were fewer -OH groups in the original prepolymer, then the hydrogen bonded aggregates would not be so large in the prepolymer and the amount of anhydride consumed in the initial reactions would be reduced. This can be achieved by adding more $n=0$ oligomers to the prepolymer (see chapter 4). A less

polydisperse system would lend itself to a more homogeneous system as that observed under neutron scattering [25]. A less reactive curing agent could be used which produces a less intense exothermic reaction, and therefore the local heating during reaction will be reduced so the the reaction will proceed at a similar rate throughout the sample. For instance tetrahydrophthalic anhydride could be used. Such a system involving a large n=0 DGEBA fraction resin and a phthalic anhydride/tetrahydrophthalic anhydride mixture (CY207-HT903) is currently available. For this system electron microscopy indicates that the nodule size range is smaller. Light scattering of the unreacted system also indicates that it is less structured with a smaller number of hydrogen bonded aggregates.

Analysis of void behaviour has shown that voids do grow as the sample undergoes uniform mechanical stress (some preferentially to others). This is true for pre-existing voids as well as those created under stress. If we consider what may be happening to the void and the surrounding material, the void will act as a stress concentrator as described in chapter 5. It will also act to concentrate strain in the matrix around the void. This will lead to local yield occurring in the surrounding network allowing the void to grow.

A step behaviour in the size of scatterer with stress

was also observed. At a certain stress value the size of scatterer decreased suggesting a yield occurring in one part of the matrix causing relaxation in another. In one case a plateau in void size was reached. This suggests that either (i) failure occurs by all voids growing to a certain size before coalescence, and crack propagation occurs, or that (ii) not all the voids in the system have the potential of causing failure. As the concentration of voids in the system is small (i.e. 10^{-5}) it is unlikely that coalescence occurs to give failure. Therefore it is probable that not all the defects in the system will lead to failure. We can assume that crack propagation and failure will occur from a single defect. This may occur via a process of 'microcrazing' where yield in the matrix will occur ahead of the crack tip due to the very high concentration of stress in that region, producing a microscopic equivalent of the bulk crazing observed in linear polymers. This will be dependent on the position of the defect in the epoxy. For microscopic crazing to occur a weakly crosslinked network could exist over the craze dimension as a single phase or as a distributed phase with more highly crosslinked material providing 'pinning' sites which limit the amount of extension. It is possible for a propagating crack to encounter a region of high crosslink density and stop

growing as the energy required to deform this region will be greater, such as the case where the void size reached a plateau. This could contribute to the slip-stick behaviour encountered by others [32] in their stress strain measurements, where crack propagation is halted and then recommences. The recommencing of crack propagation will occur when the strain energy exceeds that required to overcome deformation of the plastic region ahead of the crack. Crack propagation may also cease due to local strain being higher in another location due to void nucleation and growth elsewhere.

Consider the fracture mechanics of the system, with respect to Griffith fracture as quoted in Chapter 1. If we apply the values of σ_f and 'a' obtained experimentally in this work to the Griffith Equation for plane tensile stress, then the calculated fracture energy γ_p is 2 J m^{-2} , two orders of magnitude smaller than the macroscopic value quoted by other workers [33]. If we consider how this relates to the properties of the material then the smaller the value of γ_p the more elastic the sample is. 2 J m^{-2} is approaching the value for a totally brittle material. It may be assumed that totally elastic deformation is highly localised. This implies that locally around the defect the material behaves differently to the macroscopic sample. Deformation may be elastic or viscoelastic (ie

plastic). Therefore the Griffith theory for brittle fracture does not apply to these local regions, where the sample can undergo plastic deformation. If we consider the sample as a whole, some regions will have a greater ability to deform plastically than others as discussed in chapter 5 and later in this chapter. Therefore the macroscopic properties of the sample will be a result of all the processes occurring in the sample, and these will differ from the local microscopic properties as the material is inhomogeneous. Care has to be taken in comparing these results with those of others. Other workers consider macroscopic deformation and introduce relatively large sharp defects such as surface notches [33] for their studies. Whereas this work has investigated the local deformation of intrinsic defects in the sample.


Void growth and step behaviour was also observed under electrical stress. It is a known fact that an electrical field produces a mechanical force, and this force could cause mechanical deformation in electrically stressed materials. Calculation of this force shows that away from the pin tip the applied force is over three orders of magnitude smaller than the value for yield so negligible deformation should occur. However at the tip the force is comparable to and above that of the yield stress (see chapter 6). It is therefore likely that the strain condition and

deformation processes occurring at the pin tip will influence the deformation of the defects in the scattering volume remote from the pin tip more than the mechanical field present in the scattering volume, particularly if local failure occurs at the pin tip causing strain relaxation remote from the tip.

Under electrical stress, step behaviour in the scattering parameters was observed when the applied stress reached a value of $-2.0 \times 10^9 \text{ V m}^{-1}$. This suggests that this behaviour is a result of relaxation of the network and that some type of yield occurs around the value of $2.0 \times 10^9 \text{ V m}^{-1}$. The most likely point of yield will be the pin/matrix interface. This provides a link with the results of Shibuya [37] and his value above which harmful void growth occurred. Although his value of $3 \times 10^8 \text{ V m}^{-1}$ was smaller, it could be due to earlier yield within his resin system due to his less rigorous method of preparation. Alternatively, it may be due to the fact that space charge tip blunting has not been taken into account in this work and the actual applied field may be smaller than that calculated. However the field should not be significantly below 10^9 V m^{-1} , as this is the value quoted by Zeller [96] above which space charge injection will occur and space charge is required to drive the high interfacial mechanical stress. Also if

we consider the value of $E t^4$ for the times involved during the stress period before treeing occurs, Shibuya's value was $10^{38} V^4 h$ whereas in this study a lower bound value of $10^{41} V^4 h$ is observed. This may again be due to the more rigorous sample preparation used in this work and there being a lower probability of the sample containing a macroscopic void or defect at the pin tip.

This work has only begun to answer some of the many questions on network inhomogeneity and its link with failure mechanisms in epoxy resins, and the possibility of the primary failure processes being the same under electrical and mechanical stress. Further work is needed to establish the link by taking more samples through to failure in both the mechanically and electrically stressed situations. This work suggests that mechanical deformation processes control the formation of primary defects for both types of stress. The position of the defect in the network and its location in the sample is important if the defect is to contribute to failure. If, in the case of electrical stressing, the tree is initiated in a region of high crosslink density, then a higher stress is likely to be required to cause failure. In this work the size of pin tip was similar to the size of inhomogeneity, therefore the stresses involved around the tip are likely to be



similar to that around the inhomogeneity, and deformation via local yielding could again be the controlling factor for crack initiation and propagation. In this case this may be the primary initiation event leading to treeing, certainly in the high field region where space charge can be sustained. Further work is required to establish this.

Having established the existence of inhomogeneities and microvoids and how they deform under stress in one epoxy resin system, a logical extension to this work is to do the same for other epoxy resin systems, such as the Ciba Geigy CY207 HT903 system which has a predominance of $n=0$ oligomers and would produce smaller inhomogeneities and potentially a more chemically homogeneous network. As this work has shown that the true extent of inhomogeneity can be revealed under stress and is more complicated than originally expected, this may be true for polymers that are currently considered completely homogeneous. This work could then be extended to other types of polymers with differing network defects and inhomogeneity, to build a more complete picture of polymer network defects, defect formation and their influence on deformation and failure processes.

REFERENCES

1. Scott, J.M., Wells, G.M., and Phillips, D.C., *J Mat. Sci.*, 15 (1980) 1436.
2. Garnish, E.W., *Brit. Polym. J.*, 11 (1979) 72.
3. Nicase E., Gandini A., and Cneradame H., *Brit. Polym. J.* 18 (1986) 247, 251.
4. Mijovic, J.J., and Koutsky, J.A., *J. Applied Polym. Sci.*, 23 (1979) 1037.
5. Mijovic, J.J., and Koutsky, A.J., *Polym.* 20 (1979) 1095.
6. Morgan, R.J., and O'Neal, J.E., *Polym-Plast. Technol. Eng.* 10 (1978) 49.
7. Aspbury, J., and Wake, W.C., *Brit. Polym. J.*, 11 (1979) 17.
8. Yamini, S., and Young R.J., *J Mat. Sci.* 15 (1980) 1823.
9. Liddell, P., Ph.D Thesis, City of London Polytechnic (1979).
10. Stevens, G.C., in 'Structural Adhesives: Developments in Resins and Primers' Ed. Kinlock, A.J., Elsevier Applied Science Publishers, London and New York (1986).
11. Stevens, G. C., Champion, J.V., and Liddell, P., *J. Poly. Sci., Poly. Phys. Ed.*, 20 (1982) 327.

12. Stevens, G.C., Champion, J.V., Liddell, P. and Dandridge, A., Chem. Phys. Letts. 71, (1980), 104
13. Dusek, K., Plestil, J., Lednicky, F., and Lunak, Polymer, 19 (1978) 393.
14. Uhlmann, D.R., in ref. 2. p87.
15. Matyi, R., Uhlmann, D.R., and Kotsley, J.A., J. Polym. Sci. Polym. Phys. Ed., 18, (1980) 1053.
16. Barton, J.M., Brit. Polym. J., 11 (1979) 115.
17. Misra, S.C., Manson, J.A., and Sperling, L.H., Amer. Chem. Soc. Div. Org. Coat. Plast. Chem. Prep. 39 (1978) 152.
18. Stevens, G.C., and Richardson, M.J., Polymer, 24 (1983) 851.
19. Stevens, G.C., J. Appl. Polym. Sci., 26 (1981) 4279.
20. Stevens, G.C., J. Appl. Polym. Sci., 26 (1981) 4259.
21. Flory, P.J., Pure Appl. Chem., Macromol. Chem. 8 (1972), 1; J Macromol Sci. Phys, 12 (1976).
22. Charlesworth, J.M., J. Polym. Sci. Polym. Phys. Ed., 17 (1979) 1557,1571.
23. 'Organisation of Macromolecules in the Condensed Phase'. Farad. Disc., Chem., Soc., Roy. Soc. Chem., London, (1979)

24. Thomas, E.L., and Roche, E.J., *Polymer* 20 (1979) 1413.
25. Vander Sande, J., and Uhlmann, D.R., *J. Polym. Sci., Polym. Phys. Ed.*, 16 (1978) 2005.
26. Wignall, G.D., and Longman, G.W., *J. Mater Sci.* 8 (1973) 1439.
27. Bai, S.J., *Polymer*, 26, (1985), 1053.
28. Wu, Wen-Li and Bauer, B.J., *Polym. Comm.*, 26, (1985), 39
29. Wu, Wen-li and Bauer, B.J., *Polymer*, 27, (1986), 169.
30. Tuomin, L. and Harrison, I.R., *Polymer*, 29, (1988), 233
31. Griffith, A.A., *Phil., Trans. Roy. Soc., London (A)* 221 (1920) 163.
32. Young, R.J., in 'Developments in Polymer Fracture', Ed. Andrews, E.H., Applied Science Publishers, London 1979.
33. Kinlock, A.J., and Young, R.J., 'Fracture Behaviour of Polymers', Applied Science Publishers, London and New York (1983).
34. Morgan, R.J., Jones, E.J., and Steele, W.J., *Polym.*, 23 (1982) 295.
35. Morgan, R.J., O'Neal, J.E., and Miller, D.B., *J. Mat. Sci.*, 14, (1979) 109.

36. Morgan, R.J., and O'Neal, J.E., J. Mat. Sci., 12, (1977) 1966-88. Van Krevelen, D.W., 'Properties of Polymers', Elsevier, Amsterdam (1976).
37. Pritchard, G., Rose, R.G., and Taneja, N.J., J. Mat. Sci., 11 (1976) 718.
38. Owen, M.J., and Rose, R.G., J. Mat. Sci., 10 (1975) 1711.
39. Phillips, D.C., Scott, J.M., and Jones, M., J. Mat. Sci., 13 (1978) 1924.
40. Cherry, B.W., and Thomson, K.W., J. Mat. Sci. 16 (1981) 1924.
41. Kinloch, A.J., and Williams, J.W., J. Mat. Sci. 15 (1980) 987.
42. Kelly, F.N., Swetlin, B.J. and Trainor, D.R. in 'Macromolecules', Eds. H. Benoit and P. Rempp, Pergamon Press, Oxford. (1982).
43. Kelly, F.N. and Trainor, D.R., Polym. Bull. 7, (1982), 369
44. Arbab, M., and Auckland, D.W., IEE Proceedings, 133A (1986) 618.
45. Zeller, H.R. and Schneider, W.R., J. Appl. Phys., 56, (2), (1984), 455.
46. Shibuya, Y., Zoledowski, S., and Calderwood, J.H., Proc. IEE., 125 (1978) 352.
47. Zoledowski, S., Sakata, S., Shibuya, Y., and Calderwood, J.H., Third International Symposium on High Voltage Engineering (1979). 1

48. Shibuya, Y., Zoledowski, S., and Calderwood, J.H., IEEE Transactions on Polymer Apparatus and Systems. PAS-96 (1977) 198.
49. Shibuya, Y., Ph.D thesis, University of Salford, (1976).
50. Eichhorn, R.M., in 'Engineering Dielectrics', Vol IIIA Eds. R. Bartrukas and R.M. Eichhorn, ASTM, Philadelphia
51. Bahder, G., Gamty, T., Sosnovski, M., Eaton, R. and Katz, C., IEEE Pov. Appl. Syst., PAS-101. 1379
52. O'Dwyer, J.J., 'The Theory of Electrical Conduction and Breakdown in Solid Dielectrics', Clarendon Press, Oxford (1973).
53. Ieda, M. and Nawata, M., 'A consideration of Treeing in Polymers', CEIDP., 143-150, (1972). 95.
- Shilaya, Y., and Nitta, T., Electrical Engineering in Japan, 91 (1971) 177.
54. Robertson, R.E., J. Polym. Sci., Polym. Phys. Ed., 19 , (1981), 1277
55. Kerker, M., 'The Scattering of Light and other Electromagnetic Radiation Academic Press, New York, (1969)
56. Van de Hulst, H.C., 'Light Scattering by Small Particles', Dover Publications Inc. New York, (1957)
57. Fitzwater, S., HookIII, J.W., J Coatings Technology, 57, (1985) 39.

58. Maxwell, J.C., 'A Treatise on Electricity and Magnetism', 2 vols, Oxford, (1873).
59. Lord Rayleigh, Proc. Roy. Soc. (London), A90, (1914) 219
60. Koberstein, N., Russell, T., and Stein, R.S., J. Polym. Sci. 17 (1979) 1719.
61. Gans, R., Ann. Physik, 76 (1925) 29
62. Kerker, M., Farone, W.A., and Matijevic, E., J. Optical Soc. of America, 53 (1963) 758.
63. Pusey, N., in 'Colloidal Dispersions', Ed J.W. Goodwin, Roy. Soc. Chem., London, (1982).
64. Mie, G., Ann. Physik, 25 (1908) 377
65. Senior, M., Ph.D Thesis, City of London Polytechnic (1981).
66. Wickramasinghe, N.C., 'Light Scattering Functions for Small Particles', Adam Hilger Ltd, London (1973).
67. Bohren, C.F. and Huffman, D.R. , 'Absorption and scattering of light by small Particles', Wiley Interscience 1983.
68. Kuske, A. and Robertson, G., 'Photoelastic Stress Analysis', Wiley Interscience, London, (1974).
69. Ross, G., Optica Acta, 15 (1968) 451;16 (1969)95.
70. Debye, P., Ann. Phys., 46 (1915) 809
71. Debye, P., and Beuche, A.M., J. Appl. Phys., 20 (1949) 518.

72. Addleman, R., Ph.D Thesis, University of London, (1974).
73. Coumou, D.J., Humans, J., and Mackor, E.L., Trans. Far. Soc., 60 (1968) 2299.
74. Coumou, D.J., Mackor, E.L., and Humans, J., Trans. Far. Soc., 60 (1964) 1539.
75. Schmidt, R.L., J Colloid int. Sci. 27 (1968) 516.
76. Clough, S., Van Aartsen, J.J., and Stein, R.S., J. Applied Phys., 36 (10) (1968) 3072.
77. Stein, R.S., and Rhodes, M.B., J. Applied Physics, 31 (1960) 1873.
78. Batzer, H., and Zahir, S.A., J. Appl. Polym. Sci., 19 (1975) 601.
79. Flippan-Anderson, J.L., and Gilardi, R., Acta Cryst., B37 (1981) 1433.
80. Bantle, S., Hasslin, H.W., Meer, H.U., Schmidt, M., and Burchard, W., Polymer, 23 (1982) 1889.
81. Batzer, H., and Zahir, S.A., J. Appl. Polym. Sci., 21 (1977) 1843.
82. Lee, H., and Neville, K., 'Handbook of Epoxy Resins', McGraw-Hill, New York, (1967).
83. May, C.A., and Tanaka, Y., (Eds), 'Epoxy Resins: Chemistry and Technology', Marcel Dekker, New York, (1973).
84. Fisch, W., and Hoffmann, W., J. Polym. Sci. XII (1954) 497.

85. Fisch, W., Hoffman, W., and Koskikallio, K., J. Appl. Chemistry, 6 (1956) 429.
86. Fisch, W., Hoffmann, W., and Schmid, R., J. Applied Science 13 9 (1969) 295.
87. Tanaka, Y., and Kakiuchi, H., J. Appl. Polym. Sci., 7 (1963) 1063 & 1951.
88. Tanaka, Y., and Kakiuchi, H., J. Polym. Sci., Part A, 2 (1964) 3405.
89. Flory, P.J., 'Principles of Polymer Chemistry', Cornell University Press, London 1953.
90. De-Boar, J.H., Trans Farad Soc., 32 (1936), 10.
91. Dusek, K., and Prins, W., Adv. Polym. Sci., 6 (1969) 1.
92. Nyas, N.G., Shashikant, S., Caturkdi, P.N., and Patel, C.K., Polymer Communications, 27 (1986) 301.
93. Ghaemy, M., Bilingham, N.C., and Calvert, P.D., J. Polym. Sci., Polym. Letts. Ed., 20 (1982) 439.
94. Bell, J.P., J. Appl. Polym. Sci., 27 (1982) 3503.
95. Ciba Geigy Product Information Sheet No. C1.c.
96. Timoshenko, S.P. and Goodier, J.N., 'Theory of Elasticity', 3rd Edition, McGraw Hill.
97. Shilaya, Y., and Nitta, T., Electrical Engineering in Japan, 91 (1971) 1
98. Bevington, P.R., 'Data Reduction and Analysis for the Physical Sciences', McGraw-Hill Book Company, New York, (1969).

APPENDIX

A.1 Calculation of standard error and mean on the counts from the PMT.

A number (NCOUNTS) of reference beam counts c_{ref} and scattered counts c_{sca} were taken at each angle on average 15 counts

The mean of these counts for each angle 'i' was then calculated

$$I_{scai} = \frac{1}{NCOUNTS} \sum_{n=1}^{NCOUNTS} c_{sca} \quad (A.1)$$

The standard error (ie the uncertainty in the mean) was then calculated from s_{scai} where

$$s_{scai}^2 = \frac{1}{NCOUNTS-1} \sum_{n=1}^{NCOUNTS} (c_{sca} - I_{scai})^2 \quad (A.2)$$

giving

$$\sigma_{scai} = s_{scai} / (NCOUNTS-1) \quad (A.3)$$

A.2 Calculation of errors on fitting parameter 'a'

The errors in the fitting of the data to the theoretical curves were calculated in two ways ,

- (i) The worst fit on the data
- (ii) From the value of χ^2 and the last increment Δa_j used in the fitting routine to determine the

value of size 'a' of the scatterer.

The worst fit on the data was determined by fitting:-

- (a) The actual data to a theoretical profile. Then
- (b) adding σ_{scai} to the first half of the data values I_{scai} and subtracting σ_{scai} from the last half of the data values, and then fitting these values to theory to determine the largest scatterer present. Then
- (c) subtracting σ_{scai} from the first half of the I_{scai} to determine the smallest scatterer possible causing the scattering by again fitting to theory (fig A.1).

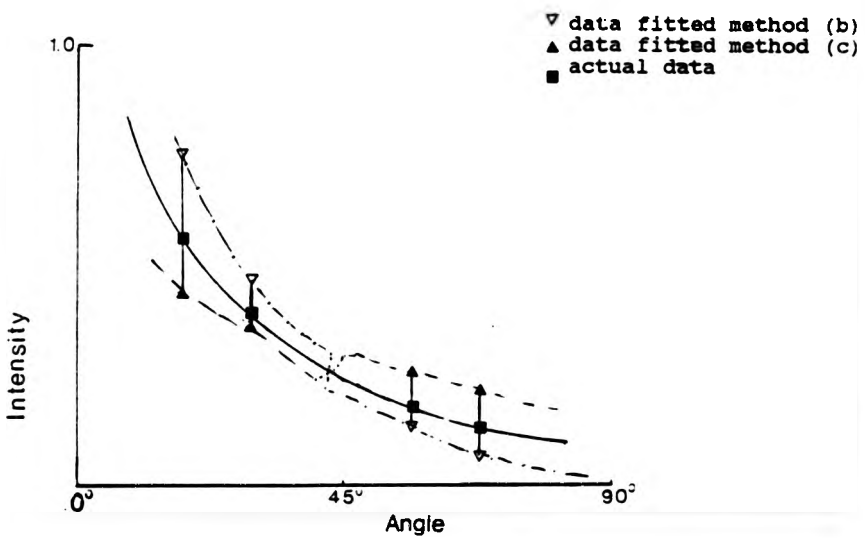


Fig.A1 Figure showing worst error on data
A.2

(ii) The second method of error determination uses the fact that at the optimum fit the function χ^2 will be at a minimum, where χ^2 is the sum of squares of the differences between the data value and the calculated theoretical value. Therefore the second derivative of χ^2 with respect to the fitting parameter 'a' will be zero. The following [54 p245] is then true for independent fitting parameters,

$$\sigma_{a_j}^2 = - \frac{2}{\partial^2 \chi^2 / \partial a_j^2} \quad (\text{A.4})$$

where a_j is the fitted parameter and σ_{a_j} is the error on that parameter. $\partial^2 \chi^2 / \partial a_j^2$ can be calculated from the last increment in the fitting parameter used Δa_j

$$\frac{\partial^2 \chi^2}{\partial a_j^2} \approx \frac{\chi^2(a_j + \Delta a_j) - 2\chi^2(a_j) + \chi^2(a_j - \Delta a_j)}{\Delta a_j^2} \quad (\text{A.5})$$

This was then used to give the value of the error σ_{a_j}



THE BRITISH LIBRARY DOCUMENT SUPPLY CENTRE

TITLE AN INVESTIGATION OF DEFECT FORMATION AND GROWTH IN EPOXY RESIN USING LIGHT SCATTERING METHODS

Elaine Ann Perkins

AUTHOR

INSTITUTION and DATE

City of London Polytechnic, 1989 (C.N.A.A)

Attention is drawn to the fact that the copyright of this thesis rests with its author.

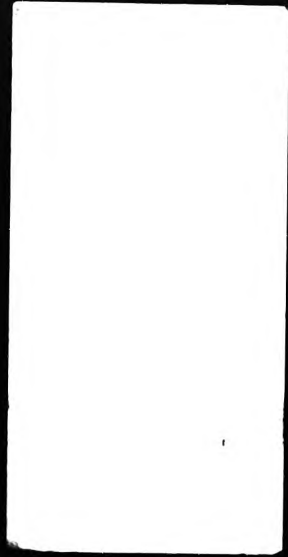
This copy of the thesis has been supplied on condition that anyone who consults it is understood to recognise that its copyright rests with its author and that no information derived from it may be published without the author's prior written consent.

THE BRITISH LIBRARY DOCUMENT SUPPLY CENTRE Boston Spa, Wetherby West Yorkshire Unked Kingdom

Table with 8 columns and 1 row, labeled 'cms'.

CAM. 9

REDUCTION X 21



DX



87724

